GEOCHEMICAL AND MINERALOGICAL EVALUATION OF CO_2-BRINE-ROCK EXPERIMENTS: CHARACTERIZING POROSITY AND PERMEABILITY VARIATIONS IN THE CAMBRIAN MT. SIMON SANDSTONE

by

Alexander Brian Gonzalez

A thesis submitted to the faculty of
The University of Utah
in partial fulfillment of the requirements for the degree of

Master of Science

in

Geology

Department of Geology and Geophysics

The University of Utah

December 2013

The University of Utah Graduate School

STATEMENT OF THESIS APPROVAL

The thesis of **Alexander Brian Gonzalez**

has been approved by the following supervisory committee members:

Brenda B. Bowen	, Chair	**10/11/13** Date Approved
Thure E. Cerling	, Member	**10/11/13** Date Approved
Lauren P. Birgenheier	, Member	**10/11/13** Date Approved

and by **John M. Bartley** , Chair of

the Department of **Geology and Geophysics**

and by David B. Kieda, Dean of The Graduate School.

ABSTRACT

The Cambrian Mount Simon Sandstone has been targeted as a major reservoir for CO_2 storage in the Illinois Basin. The Mount Simon Sandstone's geologic setting, mature quartz to arkosic composition, reservoir thickness, and generally low permeability of the overlying Eau Claire Formation seal make it an attractive candidate for long-term storage potential of carbon dioxide. Injection of CO_2 has been shown to cause a range of chemical alterations that may causes dissolution of existing minerals and precipitation of secondary phases that can alter the porosity and permeability of the reservoir. This study focuses on conducting detailed microscopic analysis of compositionally and texturally dissimilar Mount Simon Sandstone samples from the Illinois Basin that were experimentally exposed to CO_2-rich brines for 6 months at the National Energy and Technology Laboratory in collaboration with the Indiana Geological Survey. Our objective is to examine the experimental samples to determine how porosity texture and mineral abundance influence the types of reactions that occur with CO_2 injection at various scales. Petrographic and geochemical analysis coupled with Geochemist Workbench's REACT module demonstrates how porosity and permeability amounts strongly influence rates of mineral precipitation and dissolution that occur over the observed 6-month and projected 1000-year period. These results, which represent the compositional and textural heterogeneities in the formation, provide a set of criterion for evaluating CO_2 injection sites and long-term storage potential in the formation.

TABLE OF CONTENTS

LIST OF FIGURES

LIST OF TABLES

ACKNOWLEDGEMENTS

The following work reflects the wonderful personalities of the people who have helped me along the way. You know who you are. I'm greatly indebted to you all. Please expect Christmas cards for years to come.

INTRODUCTION

Between the onset of the Industrial Revolution in 1751 to the present, CO_2 emissions have risen from 280 ppm to over 400 ppm (Boden et al., 2012). Elevated consumption of fossil fuels and subsequent release of CO_2, especially over the past 30 years, is largely responsible for this dramatic rate increase. Growing concern over the rise of this greenhouse gas has led to extensive research focused on safely capturing and storing large-scale CO_2 emissions. A variety of storage mechanisms have been proposed for mitigating CO_2 emissions, including deep-ocean storage, mineral carbonization, and long-term sequestration in deep, saline reservoirs. Sequestration in deep saline reservoirs is considered one of the most promising methods because the basins are widespread, increasingly their likelihood of being near a point source of CO_2; have a large storage potential; and have been extensively studied because of their oil and gas reserves (Bachu, 2003).

The Department of Energy has established seven partnerships to determine the feasibility of geologic carbon sequestration in different regions of the United States (DOE, 2012). The Midwest Geologic Sequestration Consortium (MGSC) was formed in 2003 with the initial goal of characterizing the Illinois Basin as a long-term storage reservoir (Finley et al., 2011). Through the collaborative efforts between private companies, state geologic surveys, and associated universities, the project aims to inject 1 million tons of CO_2 into the Cambrian Mount Simon Sandstone. Injection began in late 2011 (Finley et al., 2011). The Cambrian Mount Simon Sandstone is appealing as a long-

term CO_2 storage reservoir because of the formation's depth, thickness, overlying impermeable seal, and lack of structural discontinuities (Barnes et al., 2009; Leetaru and McBride, 2009; Bowen et al., 2011).

Characterization of the geochemical and mineralogical composition of the reservoir along with the reactions that may occur with the injection of CO_2 is fundamental to predicting how storage potential varies throughout the formation. Previous studies have shown the injection of CO_2 into deep, saline formations has the potential to cause a range of chemical alterations, including dissolution of existing minerals and precipitation of secondary phases that can alter the porosity and permeability of the reservoir (Bachu, 2003; Kaszuba et al., 2003; 2005; Peters, 2009; Lu et al., 2010; Yu et al., 2012). Thus, evaluations of fluid-mineral interactions are critical in the assessment of the long- and short-term storage potential of CO_2 in a deep, saline reservoir.

Objective

The purpose of this study is to characterize and interpret how heterogeneous textures and compositions in the Mount Simon Sandstone influence the alteration that occurs in the presence of a CO_2 -saturated brine.

Geologic Sequestration

Geologic sequestration involves the capture of CO_2, its conversion into a supercritical fluid, and injection for storage into deep, saline reservoirs, coal beds, or depleted oil fields (Bachu and Adams, 1999). A part of this process (injection of CO_2 into

subsurface reservoirs) has historically been utilized as an enhanced oil recovery technique as a means to increase the recovery of liquid hydrocarbons in mature oil fields. The most promising reservoirs for long-term CO_2 storage are deep saline reservoirs that have suitable porosity and permeability to allow for large volumes to be injected and stored without over-pressurizing the system and an extensive, impermeable seal (Benson and Cole, 2008). Carbon dioxide is trapped by four different mechanisms: structural, capillary, solubility, and mineral trapping (Benson and Cole, 2008).

Structural trapping occurs first when the CO_2 is still in its supercritical form and is contained by the overlying seal. Capillary trapping follows when CO_2 fills in brine-rich pores and become immobilized. The next phase is solubility trapping when the immobile CO_2 dissolves into the formation fluid persists for thousands of years. Finally mineral trapping occurs through the precipitation of carbonate minerals such as calcite, anhydrite, alunite, and dawsonite, but due to the slow rate of silicate dissolution, the benefits of this process are not realized until several thousand years have elapsed (Benson and Cole, 2008; Balashov et al., 2013). Obtaining a detailed analysis of a reservoir's mineralogical composition is critical in determining the long- and short-term efficacy of trapping the injected CO_2 and overall reservoir integrity through the ability to predict the alteration of existing mineral formation secondary minerals.

Illinois Basin Geologic Setting

The Cambrian Mount Simon Sandstone is the basal sedimentary formation within the Illinois Basin in the Midwest United States. This cratonic basin spans approximately 650 km northwest-southeast and 300 km southwest-northeast covering an area of

approximately 155 km^2 (Figure 1A) (Macke, 1995). The basin is situated atop the 1.4-1.5 Ga Eastern Granite Rhyolite complex that underwent significant rifting in the early Cambrian producing the Reelfoot rift and Rough Creek half-graben complex (Braile et al., 1982; Kolata, 1991). The irregular Precambrian basement topography is believed to have influenced the depositional history of the Cambrian Mount Simon Sandstone (Leetaru and Mcbride, 2009). Further, basement topography impacts the distribution and accumulation of sediments, which has important implications for characterizing sequestration potential (Leetaru and Mcbride, 2009).

The rifting that occurred early in the basin's formation produced arches that represent the western, northern, and eastern edges during deposition, but the basin did not fully close until the end of the Paleozoic (Swann, 1968). Extensive crustal stretching, subsidence, and faulting resulted in an influx of ~10,000 m of arkosic sediment shed off the complex forming the base of the Sauk sequence, which encompasses both the Mount Simon Sandstone and overlying Eau Claire Formation (Figure 1B) (Kolata and Nelson, 1991).

Mount Simon Sandstone Depositional Setting

An understanding of the depositional setting is critical in the interpretation of reservoir characteristics because the environment, along with tectonic setting and existing topographic variability, influences composition and distribution of sedimentary materials and hence petrophysical porosity and permeability parameters. The thickness of the formation varies from 2,600 ft. (~800m) at the center of the Illinois Basin to less than 200 ft. (~60m) thick in the north part of the basin and is absent in the southern reaches of the

basin (Leetaru and Mcbride, 2009). The Precambrian basement's irregular topography is believed to have influenced the formation of distinct sub-basins (McBride, 1989; Leetaru and McBride, 2009). Lithologically, the formation is an arkosic to quartz arenite sandstone with fine to coarse-grained siliclastics and thin, interbedded mudstone and shale layers (Templeton, 1951). The lower part of the formation is commonly more arkosic than the upper part, which is a quartz arenite (Hoholick et al., 1984). K-feldspar is found as both detrital grains and authigenic overgrowths (Heald and Larese, 1973; Odom 1975). Clay minerals such as illite, kaolinite, and chlorite identified in the formation are interpreted as the product of feldspar dissolution and/or precipitation from pore fluids (Bowen et al., 2011). Trace fossils of *medusae* and *skolithos* in the Upper Cambrian Mount Simon Sandstone provide age constraints for the upper-section of the formation (Hagadorn et al., 2002). Depositional models of the Mount Simon Sandstone based on evidence from detrial zircon U-Pb geochronology and petrographic data suggest a mixed provenance during initial transport of fluvial sediments and later a singular provenance with deltaic and marine sediment transported (Lovell and Bowen, 2013). The Eau Claire Formation consists of siltstone, shale, and sandstone and is the overlying seal for the Mount Simon Sandstone (Swann, 1968; Bowen et al., 2011).

Mount Simon Sandstone Composition and Pore System

Porosity in the Mount Simon Sandstone fluctuates because of variable distribution of mineralogy and subsequent mechanical and chemical alteration. Petrographic, well log, and core analysis from previous studies suggest porosity is defined by the formation's composition and texture in addition to compaction with burial (Hoholick et

al., 1984; Bowen et al., 2011). The Mount Simon Sandstone's depositional setting and subsequent diagenetic alteration resulting from precipitation of authigenic minerals such as illite, kaolininte, chlorite, and iron oxides as cements, pore linings, grain coatings, and within existing grain fractures (Hoholick et al., 1984; Bowen et al., 2011). The existence of clays and other authigenic minerals and the impact this has on their composition and texture is significant because coatings around grains has shown to preserve porosity by preventing the growth of quartz cements and other overgrowths (Pittman et al., 1992). The introduction of a CO_2-rich brine has shown to dissolve clays in existing pore throats, which can expand existing fluid pathways (Bowen et al., 2011; Yu et al., 2012).

Quartz overgrowths, a primary porosity-destroying feature, are widely found throughout the formation and often occur as multiple generations. The formation of these overgrowths is interpreted as the result of the precipitation high temperature (100-130C), saline-rich fluids that migrate regionally (Fishman, 1997; Chen, 2001; Pollington et al., 2011). Feldspar amounts have been found to reach as high as 40% and potentially may have formed early in the burial history concurrently during the formation of quartz overgrowths (Bowen et al., 2011). The dissolution of feldspar, especially in the lower arkosic section of the formation, is one of the primary factors that leads to the development of porosity.

Predictive Modeling of CO_2 Sequestration Systems

The purpose of experimental reactivity studies is to observe and determine alteration that could occur within reservoirs and seals, under the appropriate reservoir pressure and temperature conditions, with injection of CO_2. The materials used and

experimental conditions they are subjected to are important components in experimental studies. Some previous studies use synthetic mineral assemblages that represent typical reservoirs to react under sequestration conditions (Kaszuba et al., 2005; 2003; Newell et al., 2008). Geochemical modeling studies conducted on the Mount Simon Sandstone have used mineral composition amounts from previous data (Liu et al., 2011; Bashaov et al. 2013), which as with synthetic sedimentary samples, may not necessarily be representative of the variability and heterogenetiy observed in nature.

The modes of analysis and construction of reactions used in this work were influenced by previous studies. The use of SEM/EDX microscopy and Gazzi-Dickinson point counting to characterize textures and compositions of experimental samples and Inductively Coupled Plasma spectroscopy to measure brine chemistry has been implemented in previous studies (Kaszuba et al., 2005; 2003, Rosenbauer et al., 2005, Yu et al., 2012). Results from the laboratory CO_2-brine-rock experiments were then used to construct the compositional framework for geochemical modeling software, which project the long- and short-term influence of CO_2 in the system (Rosenbauer et al., 2005, Liu et al., 2011; 2013). Establishing a high-resolution composition of initial and post-experimental brine, pores, and mineralogy under reservoir conditions allows for dissolution and reprecipitation amounts to be estimated throughout the sequestration process.

Figure 1. Scale of study. (A) Outline of the Illinois Basin with approximate location of Experiment B plugs. (B) Cross-section of the Illinois Basin with approximate locations of the two experimental samples in the Mount Simon Sandstone shown by squares. The cross-section is modified from Kolata and Nelson (1991). (C) The experimental core plugs, measuring 3''x 1'', were taken from #1 Duke Energy Indiana IGCC core in Knox County, In. and WD-1 Newport Chemical Plant core in Vermillion County, IN. The location of thin sections used in petrographic analysis are shown on the plugs. (D) Photograph of thin section cutting across core sample used in experiment. The squares on the thin section indicate regions analyzed with SEM/EDX study. Three zones of analyses were considered: inner (0-4 mm from center of sample), middle (4-8 mm from center of sample), and outer (8-12 mm from center of sample).

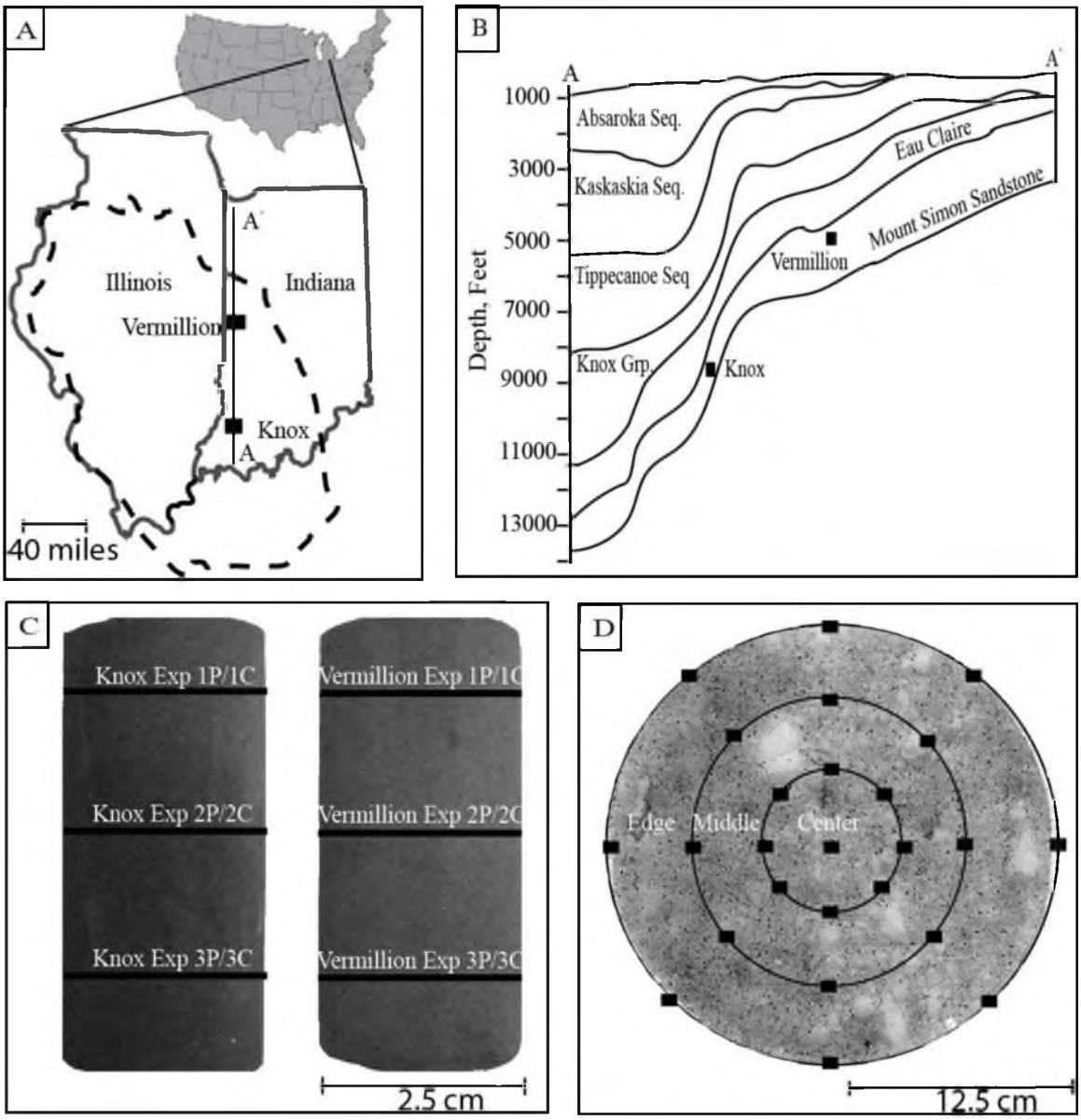
A
A'
Illinois
Indiana
Vermillion
Knox
40 miles
B
A
A'
1000
3000
5000
7000
9000
11000
13000
Depth, Feet
Absaroka Seq.
Kaskaskia Seq.
Tippecanoe Seq
Knox Grp.
Eau Claire
Mount Simon Sandstone
Vermillion
Knox
C
Knox Exp 1P/1C
Knox Exp 2P/2C
Knox Exp 3P/3C
Vermillion Exp 1P/1C
Vermillion Exp 2P/2C
Vermillion Exp 3P/3C
2.5 cm
D
Edge
Middle
Center
12.5 cm

METHODS

Mount Simon Sandstone samples were subjected to a CO_2-saturated brine at elevated pressures and temperatures at the National Energy Laboratory (NETL) in Pittsburgh, PA in an effort to stimulate any mineral reactions that might take place within the unit if it were used as a storage reservoir. Before and after the experiment permeability, porosity, and weight measurements were taken of each plug. Post-experiment, thin sections were analyzed using a combination of mineralogical, geochemical, and petrographic techniques to determine if any compositional and textural alteration occurred after exposure to the CO_2 and brine (Table 1). Empirical observations were then incorporated into Geochemist Workbench's REACT module to investigate the changes that would be expected to occur when reacting the bulk Mount Simon Sandstone composition and pore-scale composition with CO_2 charged brine over the course of the experiment and extrapolated out to 1000 years.

Experimental Design

Six Mount Simon Sandstone plugs, each measuring 3.2 cm x 5.7 cm x 0.6 cm, were used in Experiments A and B. In Experiment A, three sandstone plugs were taken from the WD-1 Newport Chemical Plant core in Vermillion County, IN and one from the Midwest Steel WD #1 core in Porter Co., IN. The two sandstone plugs in Experiment B are taken from the WD-1 Newport Chemical Plant core in Vermillion County, IN and #1 Duke Energy Indiana IGCC core in Knox County, In. (Figure 1A). The Knox Co.,IN

8642.5-B sample was selected because this site was originally proposed as an injection site for the "Next Generation" CO_2-EOR project (Figure 1C). The Vermillion Co., IN 5806-B plug was used because of the cores' proximity to the ADM site where CO_2 is presently being injected (Figure 1C). The plugs were held in separate Teflon containers and placed in gold-coated, 1L pressure vessels filled with a 75,500 ppm NaCl solution that was crafted to mimic the geochemistry of brine found within the pores of the Mount Simon Sandstone (Table 2). The pressure vessel was then purged with CO_2 three times to remove residual O_2 and N_2. Finally, approximately 4.08 MPa (600 psig) of CO_2 was charged into the vessel and then the reactor was slowly heated to final temperature of 85 °C and pressure of 23.8 MPa over the course of 4 hours. Once the experimental conditions were met in the vessels, they were held for 6 months (~4383 hours). The elevated pressure and temperatures were chosen to expedite mineral reactions during the nonflow through experiment.

Upon completion of each experiment, the temperature of the reactor was cooled down to room temperature and then the CO_2 was slowly vented and the sample was removed from the reactor. After being removed from the vessel, each of the wetted core samples was quickly preserved in a moistened Kimwipe presoaked with the 75,000 ppm of NaCl solution. The sandstone plugs and aliquots of the brine used in the experiment (before and after) were then sent to Purdue University for petrographic examination and chemical analysis.

Brine Chemistry

Ion Chromatography, Inductively Coupled Plasma, and Inductively Coupled Plasma Optical Emission Spectrometry were used to analyze the major ion and trace element composition of the experimental brine both before the experiments were conducted and after the experiment.

Petrological Analysis

Petrographical analysis was used to establish an initial composition of each sample to both compare to other previously measured Mount Simon Sandstone samples and to evaluate any compositional and textural alteration that occurred after exposure to the CO_2 and brine.

Four sets of thin sections were made from each of the sandstone core plugs that were used in Experiment B (Table 3). The thin sections were cut as cross-sectional transects near the top, middle, and base of the core plugs and include both covered and polished thin sections that were vacuum impregnated with a blue epoxy to help identify pores (Figure 1D). The covered thin sections were stained with Potassium cobaltinitrite ($K_3[Co(NO_2)_6]$) to distinguish K-feldspars. The polished thin sections were examined with traditional petrographic microscopy techniques, including transmitted, reflect, plane, and polarized light at 20x-400x magnifications. The duplicate polished thin sections were utilized for SEM/EDX analysis (Table 3) (Appendix A). In addition, additional thin sections were made of unreacted billet samples from the same cores from which the experimental cores were derived (Table 3).

The Gazzi-Dickinson point counting method was used to characterize the compositional and textural features of both reactive and nonreactive samples from both the Knox County and Vermillion County cores (Appendix B) (Ingersol,1984). Five hundred grain and two hundred-grain size measurements were recorded at 400- and 100x magnification under transmitted light microscopy for each covered thin section. Quartz, K-feldspars, lithics, and porosity were the primary minerals and textures identified using this method. The first 200 measurements recorded the long and short axis, composition, and roundness of each grain or pore. The remaining 300 recorded composition and roundness. Emphasis was placed on characterizing porosity in the samples, specifically recording proximity to grains, shape, and distribution. One thin section from each reactive sample was analyzed for a total of 1,000 grains and 400 grain size measurements (Table 3). Additionally, 2,000 grains and 800 grain size measurements were recorded from three Knox County samples at depths of 8642.5, 8542, and 8642.2 ft. (~2630m) and one Vermillion County at 5805 ft (~1769m) (Table 3).

Backscattered electron (BSE) images were taken of 12 thin sections from Vermillion samples, including those used in Experiment A to determine detrital and secondary mineral composition, abundance, porosity, and textures. Each image was approximately 1.45 x 1.45 millimeters in size to identify any mineralogical and textural variability. A combination of both coarse- and finer-scale BSE imaging and subsequent quantitative analysis with the electron microprobe was implemented to identify the minerals. Once the minerals were identified, further analysis was conducted to quantify mineralogical or textural features.

Pore-Scale Characterization

A FEI Quanta 3D FEG Dual-beam Scanning Electron Microscope/Energy Dispersive X-Ray Spectroscopy (herein SEM/EDX) was used to obtain high resolution images of mineral and pore-scale textures and make quantitative measurements of elemental concentrations. These analyses allow us to obtain high-resolution images of mineral and pore-scale textures and make quantitative measurements of elemental concentrations. The SEM is an effective and versatile tool that uses a highly focused beam of electrons to scan a sample and produce a raster image based on how the electrons and x-rays are either ejected or absorbed from the sample (Goldstein et al., 2003). The EDX similarly measured incident electron beam and sample interactions to obtain a chemical analysis of a surface (Goldstein et al., 2003). All measurements were taken from a working distance of 10mm, spot size of 6 nm, incident beam strength of 20Kv, and in Low Vacuum Secondary Electron Detector (LVSED) mode. 300x EDX measurements were run for 30 seconds and all pore measurements were run for 60 seconds.

Zone Analysis

Preliminary work comparing samples that were exposed to the experimental conditions and those that were not demonstrated the difficulty in conclusively identifying whether observed differences were due to the experiment, or were simply the result of natural heterogeneity within the Mount Simon Sandstone. Thus, we designed the analyses to investigate spatial changes between the outer edges of the core plugs that were in direct contact with the experimental brine, and the interiors of the samples that would

have only experienced exposure to the brine if the fluids diffused through the open pores over the 6 months of the experiment. We hypothesize that the influence of CO_2 and brine was primarily confined at the outermost edges (1-2mm) of the plugs, and if the experiments resulted in alteration, we would observe differences in the composition and texture along the cross-section of the samples. To evaluate this hypothesis 174 300x magnification and 144 individual pore measurements of both Knox and Vermillion experimental samples were made. To measure the extent of alteration, 72 pores from each experimental sample (n=144) at different intervals were analyzed to determine if zones of alteration exist (Figure 1D). Three zones spanning 4mm in radius were created and 24 pore measurements were made in each zone for a total of 72 per sample.

Porosity Estimation

Estimates of the experimental sample's porosity were derived from whole thin section scans and the combined 318 SEM images. Measurements were taken using ImageJ64, a program for image processing and analysis. The Threshold and Region of Interest functions were used to isolate and calculate the pore space present in the images for both experimental samples. The purpose of these measurements is to understand how the estimates compare at the various magnification levels and the NETL laboratory values.

Pore Characterization

Total surface area, microporosity, morphology, and mineralogy measurements were used to distinguish textural and compositional variations for present in the pores of

the two experimental samples. ImageJ64 was used to calculate the total surface area for all 144 pores that were imaged by the SEM/EDX. All surface area measurements made were based on the area where EDX measurements were made on individual pores. Morphology characterization was established by separating each pore into three groups: round, etched, and irregular. Round pores are generally spherical in shape and contain few asymmetric edges. Etched pores have coarse to acute edges but still are round in shape whereas irregular pores are typically not round and lack any defined structure (Figure 2A). The purpose of this measurement is to determine if the CO_2-rich brine potentially influenced the shape of the pores and if differences can be observed across the core plug cross-sections. Mineralogy characterization is based on separating different types of minerals contained in the pore into four groups: quartz, quartz/nonquartz grains, quartz/nonquartz grains/clay, and clay (Figure 2B). Minerals and clays were distinguished based on brightness, which is representative of elemental composition, morphology, and relative abundance in pores. Mineralogy determination was conducted by using SEM images to examine grain morphology and brightness rather than measurements from the EDX analysis. Quartz grains and overgrowths were found in nearly all pores. Fe- and Al-rich grains varied in size and morphology but are visibly much brighter than quartz grains. This is a result of Fe- and Al- rich grains having higher atomic weights gives them a "brighter" appearance. The atomic weights influence the behavior of the secondary electrons that are emitted as quartz grains tend to be darker because the secondary electrons it attracts can escape more easily than Fe- and Al- grains and clays, which retain more of the secondary electrons giving them their bright appearance (SEM Short Course 2012). Clays were identified by their brightness and

fibrous textures. Similar to morphology, examination of the distribution of minerals within pores between zones can indicate the amount of precipitation and/or dissolution that took place to form new minerals and alter existing mineralogy. Microporosity is a gauge of the amount of open space within the pore from high to low (Figure 2C). Pore-filling and linings were examined to determine the relative proportion of minerals and clays to open space present in each pore. A pore with low microporosity is filled nearly completely with the previously described minerals or clays. Conversely a pore with high microporosity is unoccupied by minerals and lacks textural features. The purpose of this measurement is to survey the pores within each zone and determine if any variability exists between the center, middle, and edge that may indicate how deeply the CO_2-rich brine penetrated the samples. This measurement was difficult because the presence of epoxy in the pores may have altered the textural makeup of the pores.

Reaction Modeling

Empirical observations were incorporated into geochemical models to investigate the changes that would be expected to occur when reacting the Mount Simon Sandstone bulk sample composition and pore-scale composition with CO_2 charged brine over the course of the experiment and extrapolated out to 1000 years. Geochemist Workbench was used to construct reaction path models using compositional inputs from both samples in the Batch B experiment. The software has been applied in previous modeling studies because the activity, temperature, and pressure ranges in the thermodynamic settings span the relevant conditions present in geologic sequestration processes (Parry et al., 2007; Berger et al., 2009; Nondorf et al., 2011). The module REACT was used primarily to

trace the different reaction paths between the two samples focusing on modeling mineral saturation and dissolution along with fluxes in pH and porosity. ACT and TACT modules were used to project mineral stability diagrams that span the various temperature and pressure conditions and mineral concentrations that may occur during the sequestration process.

Model Parameters

The input parameters for Geochemist Workbench's module REACT were based on the experimental conditions at which the samples were held and measurements of mineralogical and pore compositions. The temperature and pressure were fixed at 85 C and 8 moles of CO_2. Brine values, including pH, were adapted from ICP-MS and ICP-OES analysis. The bulk composition model considered 1 L of brine while the pore model incorporated the same prereactive brine scaled to fill the average volume of a pore in both the Knox and Vermillion samples (Table 2).

Mineralogical abundances with specific molarities and surface areas were calculated from point count composition results for the bulk composition (Table 3). Mineralogical concentrations were determined from point counting results of reactive samples. Mineral surface areas were calculated using the specific surface area equation (e.g., Knauss et al., 2005). All minerals in the bulk composition model were assumed to have a .25 mm grain diameter based on the formation's fine to medium-grains (Udden-Wentworth scale, Heald, 1973). The volume of minerals in the bulk composition model, expressed in moles, present in the samples is calculated by dividing the percentage of minerals present in the sample by the total sample mass minus the samples respective

porosity amount calculated at the NETL. Mineral ratios remained constant, but porosity values were adjusted to understand how variations in porosity influenced mineral saturation and/or dissolution amounts. Kinetic rates, applied uniformly to both the bulk composition and pore models, selected from previous publications, contain empirically derived and compiled references of existing rates at appropriate temperature and pH conditions (Table 3 and 4) (Kharaka, 2004; Nondorf et al., 2011).

Reactive pore surface areas for the pore-scale model were calculated from measuring the differences in total surface area and pore surface area in the SEM image using ImageJ64 surface area measurements of SEM images. Each SEM pore image was assumed to be a cube with the pore volume representing the difference between the total volume of the image and nonpore volume (Figure 3). Elemental EDX weight-percent values were converted to normalized oxide amounts, which were further used to construct minerals. Ratios of minerals present in the reactive surface area of the pores were established by assuming the most common cation end members found in the EDX analysis Si, K, Fe, Mg, Al, Ca, and Na represent quartz, K-feldspar, hematite, illite, Al-oxide, calcite, and albite, respectively (Table 4). In an attempt to understand how the heterogeneity of minerals present in the pore impact rates of dissolution and precipitation in the samples, a pore with average composition was compared with individual pores with the highest reported elemental weight percent of the cations (Table 4).

Variations in porosity and mass for the Experiment B samples were modeled to quantify the relationship between the measurements and extrapolate to different scales. The postexperiment porosity and mass amounts for the Vermillion Co. IN 5806-B sample show a 1.6% decrease in porosity resulted in a .6 gram decrease in sample mass.

This decrease in mass per increase in porosity relationship was applied to both Experiment B samples to determine how mineral saturation was altered at higher porosities. A 1 gram decrease per 1.6% porosity increase was also implemented to further test how a larger mass decrease alters mineral saturation rates during short- and long-term periods.

Figure 2. Summary of pore characterization methodology. (A) Pore morphology characterization defined by examination of SEM pore images. All pores were divided into 3 groups: round, etched, and irregular. (A1) Sphere-shaped pores with smooth to slightly-deformed edges. (A2) Generally round in shape but contain more coarse edges. (A3) Pores lack any defined shape and have very irregular edges. (B) Mineralogy characterization defined by examination of grains and clays present in pores. All pores were divided into 4 groups: quartz, quartz/nonquartz, quartz/nonquartz/clays, clays. (B1) Pores are primarily filled with quartz grains. (B2) Pores contain both quartz and various nonquartz grains. (B3) Pores are filled with quartz, nonquartz, and clays. (B4) Pores are primarily filled with clays. (C) Microporosity characterization defined by examination of amount of open space in pores. All pores were divided into 3 groups: low, medium, and high. (C1) Pores are filled entirely with minerals and clays. (C2) Pores contain some minerals but have open pore space. (C3) Few to no minerals present in pore but may be in pore linings.

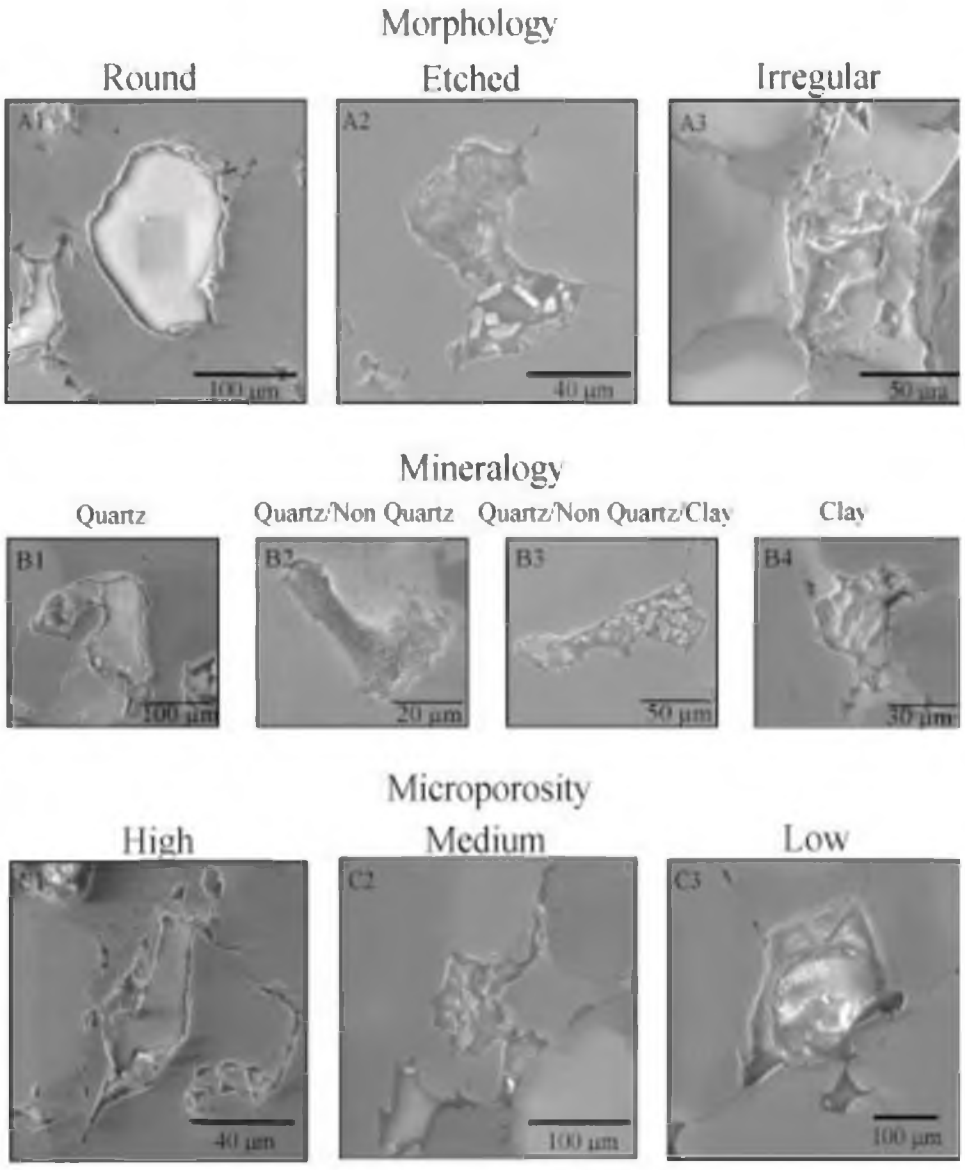
Morphology
Round
Etched
Irregular
A1
A2
A3
100 µm
40 µm
50 µm
Mineralogy
Quartz
Quartz/Non Quartz
Quartz/Non Quartz/Clay
Clay
B1
B2
B3
B4
100 µm
20 µm
50 µm
30 µm
Microporosity
High
Medium
Low
C1
C2
C3
40 µm
100 µm
100 µm

Figure 3. Conceptual pore model. (A) Vermillion sample and (B) Knox sample. Cube surface area measurements were used from ImageJ64 analysis. Volume was assumed to be identical to height and width.

A

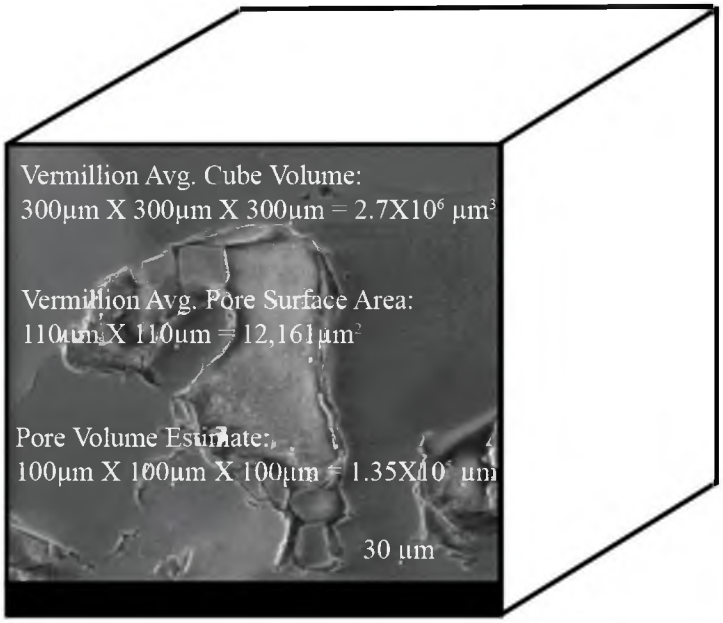

$$\left(\frac{1g}{dm^3}\right)*\left(\frac{1dm^3}{1x10^3\ cm^3}\right)*\left(\frac{1cm^3}{1x10^3\ mm}\right)*\left(\frac{1mm^3}{1x10^9\ \mu m^9}\right)*\left(\frac{1.35x10^5\ \mu m^3}{1\ pore}\right)=1e^{15}$$

B

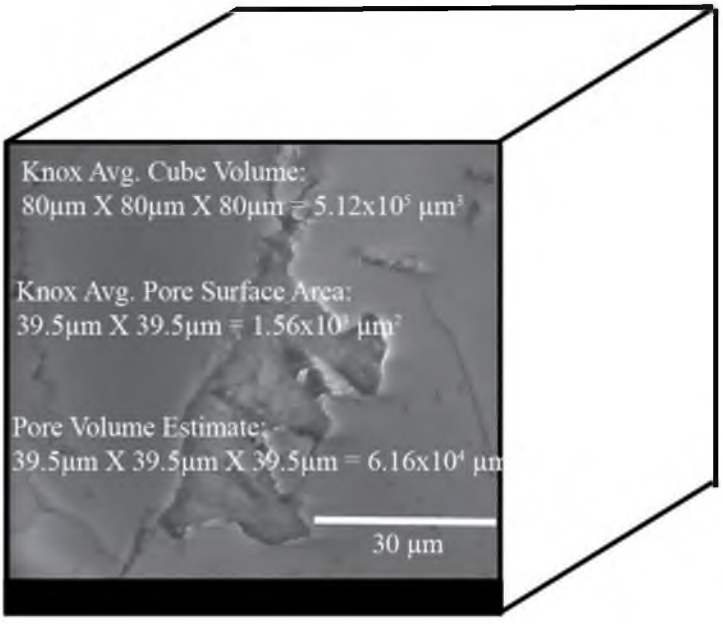

$$\left(\frac{1g}{dm^3}\right)*\left(\frac{1dm^3}{1x10^3\ cm^3}\right)*\left(\frac{1cm^3}{1x10^3\ mm}\right)*\left(\frac{1mm^3}{1x10^9\ \mu m^9}\right)*\left(\frac{6.16x10^4\ \mu m^3}{1\ pore}\right)=1e^{15}$$

Table 1. List of Mount Simon Sandstone plugs from Experiment A and B

Experimental Plug Identification
Vermillion Co., IN 5806-A1
Vermillion Co., IN 5806-A2
Vermillion Co., IN 5465-A
Vermillion Co., IN 5740-A
Porter Co.,IN 3451-A
Vermillion Co. IN 5806-B

*Naming convention is the well the plug was taken from, depth of plug, and experiment the plug was used.

Table 2. Summary of ion and trace element concentration of pre-experimental brine

Brine Component	Bulk Brine Sample	Knox Pore Brine	Vermillion Pore Brine
H_20	1 L	6.00E-11	1.35E-09
Na	4.74E+04	2.90E-09	6.40E-08
Ca	1.79E+04	1.10E-09	2.42E-08
Cl	1.35E+04	8.00E-09	1.75E-07
Ba	1.07E+04	6.60E-13	1.44E-11
Mg	2.27E+03	1.40E-10	3.06E-09
K	1.28E+03	7.90E-11	1.73E-09
SO_4	5.89E+03	3.60E-11	7.95E-10
Fe	7.58E+01	4.70E-12	1.02E-10
NO_3	2.39E+01	1.50E-14	3.20E-11
Ni	8.15E-01	5.00E-14	1.10E-12
Co	2.93E-02	1.80E-15	3.95E-14
Pb	2.00E-02	9.50E-16	2.08E-14
HCO_3	1.00E-02	1.80E-15	1.80E-15
Cs	1.36E-03	8.80E-16	1.80E-15
Al^{3+}	1.00E-03	5.00E-12	5.00E-12
Mn	2.00E-05	6.20E-16	1.35E-14
H^+	3.3	3.3	3.3

For the pore-scale model, the brine was scaled down to fit the pore while keeping the element ratio consistent.

Table 3. List of thin sections created from Experiment B plugs

Well	Well ID	Depth ft.	Thin Section	Use
Vermillion	125110	5806	Verm EXP 5806 1P	SEM
Vermillion	125110	5806	Verm EXP 5806 1C	Pet
Vermillion	125110	5806	Verm EXP 5806 2P	SEM
Vermillion	125110	5806	Verm EXP 5806 2C	Pet
Vermillion	125110	5806	Verm EXP 5806 3P	SEM
Vermillion	125110	5806	Verm EXP 5806 3C	Pet
Knox	N/A	8642.5	Knox EXP 8642.5 1P	SEM
Knox	N/A	8642.5	Knox EXP 8642.5 1C	Pet
Knox	N/A	8642.5	Knox EXP 8642.5 2P	SEM
Knox	N/A	8642.5	Knox EXP 8642.5 2C	Pet
Knox	N/A	8642.5	Knox EXP 8642.5 3P	SEM
Knox	N/A	8642.5	Knox EXP 8642.5 3C	Pet
Vermillion	125110	5806	Verm EXP 5806 4C-S	PC
Knox	N/A	8642.5	Knox EXP 8642.5 4C-S	PC
Vermillion	125110	5805	Verm 5805 P	Pet
Vermillion	125110	5805	Verm 5805 C	PC
Knox	N/A	8542	Knox 8542 Billet C	PC
Knox	N/A	8642.2	Knox 8542.2 Billet C	PC
Knox	N/A	8642.5	Knox 8542.5 Billet C	PC
Knox	N/A	8642.5	Knox 8542.5 Billet P	PC

Thin sections from experimental samples were cut near the top, middle, and bottom of the plugs. The polished thin sections were used in SEM/EDX analysis and covered thin sections were stained and used for petrographic analysis.

Table 4. Summary of porosity measurements

Measurement Method	Knox Co. IN 8642.5-B	Vermillion Co. IN 5806-B
300x Magnification	2.1%	6%
Whole Thin Section	1.3%	5%
NETL Laboratory	1.1%	6.3%

The 300x porosity measurements was taken from using ImageJ64 to measure 172 SEM images across the three zones for both Experiment B samples. Whole thin section porosity was determined from using ImageJ64 to calculate the amount of blue epoxy-stained pores. The NETL porosity values are derived from helium injection measurements.

RESULTS

Clay and Feldspar Dissolution

Back Scattered Electron (BSE) images of typical pore spaces in both pre- and postexperiment A samples show variable dissolution amounts. The Porter Co., IN 3451-A experiment was conducted in the presence of both a CO_2-rich atmosphere and acidic Na-rich brine. The Vermillion Co., IN 5740-A experiment was conducted in the presence of a CO_2-rich atmosphere but no brine. The pore spaces of both preexperiment samples are partially or nearly filled with very fined grained secondary clay minerals. Similar clay minerals are almost completely absent from the postexperiment Porter Co., IN 3451-A sample but are still visible in the postexperiment Vermillion Co., IN 5740-A experiment.

An important aspect of the Mt. Simon sandstone is the presence of secondary overgrowths on all detrital feldspar (and quartz) grains. Figure 4 shows examples of detrital feldspar grains and overgrowths from samples Vermillion Co., IN 5806-A1&2. Microprobe analysis of the detrital feldspar grains in all Experiment A samples studied display a range in composition from Or_{92} to Or_{98} with a mean value of around Or_{96}. In contrast, the feldspar overgrowths are invariably close to pure orthoclase ($Or_{99\text{-}100}$). The Vermillion Co., IN 5806-A1&2 experiments clearly demonstrate a partial dissolution of the feldspar overgrowths whereas the Vermillion Co., IN 5740-A experiments do not. A comparison of the 6-month and 12-month Vermillion Co., IN 5806-A1&2 experiments does not show more advanced feldspar dissolution in the longer duration experiment suggesting that all dissolution occurred within a 6-month time frame.

Knox Co. IN 8642.5-B

The Knox Co. IN 8642.5-B had an initial porosity of 1.5%, permeability of 19 nD, and weight of 61.6g. Postexperiment measurements show the sample underwent a 27% decrease in porosity to 1.1%, a 21% permeability increase to 23.9nD, and slight reduction in mass to 61.1g (Figure 5) (Table 5).

SEM/EDX data and petrographic analysis indicate the experimental sample's low porosity and high quartz cement composition confined the CO_2 and brine influence to the outer edges. The sample strategy devised to investigate if zones of dissolution occurred in the plugs identified several key differences between samples. Petrographic observations of thin sections highlight differences in pore types found in the interior and exterior of the sample (Figure 6). The largest pores, located at the edge of the sample, contain feldspars with various dissolution textures and an abundance of clay materials infilling (Figure 6E). One pore also displayed possible accumulations of halite crystals, which indicate precipitation of secondary minerals. The interior pores appear more homogenous in composition with a majority of the pores showing little buildup of material and minor dissolution of feldspars. Other observations included highly cemented grains, grain fractures, and high abundance of K-feldspar grains displaying variable morphologies (Figure 5A). Point counting results of experimental and nonexperimental thin sections characterize the composition as containing quartz amounts of approximately 70%, K-feldspar amounts between 17% and 30%, porosity values of less than 5%, and lithics composing 5% (Figure 7A). The Knox Co. IN 8642.5-B sample had the largest quartz grains of all measured experimental and nonexperimental samples (Figure 7C). A

porosity of 1.3% and feldspar amount of 26.8% was found by measuring the blue and yellow staining in the thin section using ImageJ64, which is in line with the point counting results (Table 6). As a result of the short reaction time, complete mineral dissolution and/or precipitation was not expected to occur; thus, the use of SEM/EDX microscopy was useful in identifying textural and compositional variations.

The use of EDX measurements quantifies the compositional and surface area differences present in pores within the three zones. Ratios of Al to K amounts taken from EDX weight percent were used to estimate the relative amount of K-feldspar and clays present in pores. A high Al/K EDX ratio indicates a higher amount of clay minerals present; conversely a low Al/K ratio suggests higher K-feldspar amount (Figure 8B). The ratio of 1.39 for all three zones in the Knox pores contrasts with the ratio of 4.9 for all Vermillion pores, indicating higher amount of K-feldspar corroborates with volume amounts derived from point counting. The ratios did not vary by more than .1 between all three zones in the Knox sample. Pore characterization of the zones indicates the pore morphologies and microporosity vary widely in the Knox Co. IN 8642.5-B sample and contain abundant quartz, feldspars, and clays (Figure 9). The size of these pores are roughly ten times smaller than in the Vermillion Co. IN 5806-B sample with the largest pores located at the edge of the sample (Figure 8D). Estimates recorded from ImageJ64 measurement of 300x magnification SEM images show porosity varies slightly between the inner and outer portion of the sample. The Knox County sample has an overall porosity of 2.06% with the inner (0-6.5 mm) measuring 2.07% and outer (6.5-12.5mm) measuring 2.05%.

EDX pore composition data show Na^+ and Ca+ are concentrated primarily at the outer edge of the sample and nearly absent in the two inner zones. All of the eight pores that contained Na^+ in the pores were located at the outer, 12mm edge. Halite is the primary Na^+-bearing mineral that precipitates from the pore fluid. The distribution of Ca in the sample provides further evidence that the most alteration occurred during at the edge of the sample. Ca, a primary component of the brine with a concentration of 17900 mg/l, was found in more pores and at higher amounts at the outer 12mm zone than in the interior zones.

Vermillion Co. IN 5806-B

The Vermillion Co. IN 5806-B had initial porosity of 7.9%, permeability of 1.6 mD, and weight of 66.78g. Postexperiment measurements for Vermillion Co. IN 5806-B revealed a 69% permeability decrease to .5mD, a 20% porosity decrease to 6.3%, and slight mass reduction to 66.3 grams (Figure 5, Table 5).

Petrographical observations show the experimental and nonexperimental samples as having variable mineralogical compositions and porosity values compared to the Knox Co., 8642.5-B sample. Point counting results of the Vermillion Co.,IN 5806-B show K-feldspar constitutes 4% of the reacted sample compared to 15% found in the unreacted sample located 5805 ft (Figure 7A). These amounts fall within the 1-15% feldspar range found in the 12 separate Vermillion County samples analyzed using the electron microprobe. A porosity of 5% and feldspar amount of 1.94% was found by measuring the blue and yellow staining in the thin section using ImageJ64, which is in line with the

point counting results (Table 6). A majority of the porosity observed under plain-light microscopy shows is the product of feldspar dissolution (Figure 6E-H).

Pore surface area measurements show Vermillion County sample has the largest and most uniformly distributed pores (Figure 7D). The morphology of the Vermillion pores show a shift from irregular pores at the center zone to etched at the middle and edge (Figure 9C). Microporosity in the Vermillion sample shows a progression of porosity that increases from the center to the edge, which is absent in the Knox sample (Figure 9B). The mineralogy of the Vermillion sample shows the quartz/nonquartz/clays are found in the highest abundance at the edge zone (Figure 9A). Estimates recorded from ImageJ64 measurement of 300x magnification SEM images show porosity varies slightly between the inner and outer portion of the sample. The Knox County sample has an overall porosity of 2.06% with the inner (0-6.5 mm) measuring 2.07% and outer (6.5-12.5mm) measuring 2.05%. EDX data show Fe, Mg, Ti, Al, and K were similarly found in all of the Vermillion pores but in lower weight percent compared to the Knox sample (Figure 8). Unlike Knox, Ca and Na were identified across all parts of the sample.

Brine Chemistry of Experiment B Experimental Samples

All major ions and trace elements increase in concentration after the experiment. Particularly, the amount of Na, Fe, K, Al, Ni, Ba, Mn, and Pb all increased considerably (Figure 10). Given that elemental concentrations increased, no evidence of mineral precipitation was observed based on the fluid chemistry.

Geochemical Modeling of Mineral Saturation

Mineral saturations for bulk and pore-scale models suggest mineral dissolution was variable between samples, which has significant implications for predicting the development of secondary porosity and identifying areas with optimal CO_2 storage potential. Kaolinite in the Knox and small amounts of quartz in both samples were the only minerals that precipitated in the brine after 6 months and 1000 years (Figure 11A and D). All other minerals underwent rapid dissolution when in contact with the brine and CO_2 but slowed as the system reached equilibrium. Porosity variations in the two samples revealed differing mineral saturation paths at both 20% and 40% (Figure 12). In the pore-scale models, high concentrations of ions such as K and Fe identified from EDX analysis did not influence mineral saturation states when compared to the average concentration.

Figure 4. BSE images of K-feldspar from Experiment A. Vermillion Co., IN 5806-A1 and A2 show preferential dissolution of the ~Or_{99-100} overgrowth. (A) displays the lowest and (B) displays the highest Or content of detrital grains measured. The original grain is interpreted as orthoclase and the overgrowth as microcline based on composition results.

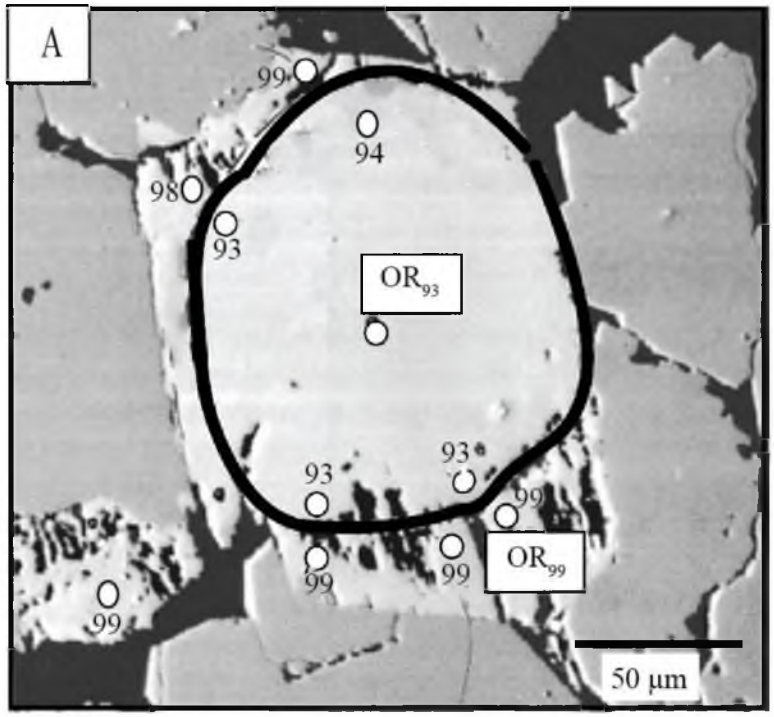
A
99
94
98
93
OR93
93
93
99
99
99
99
OR99
50 µm

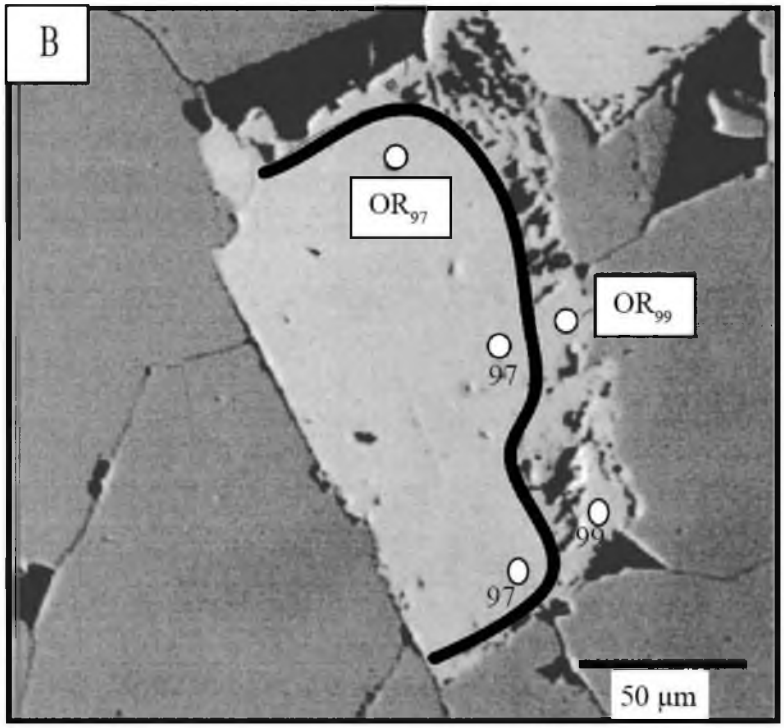
B
OR97
OR99
97
99
97
50 µm

Figure 5. Porosity and permeability results. Comparison of Pre- and Post-Experiment B samples compared to previously measured Mount Simon Sandstone samples from Frailey et al. (2011).

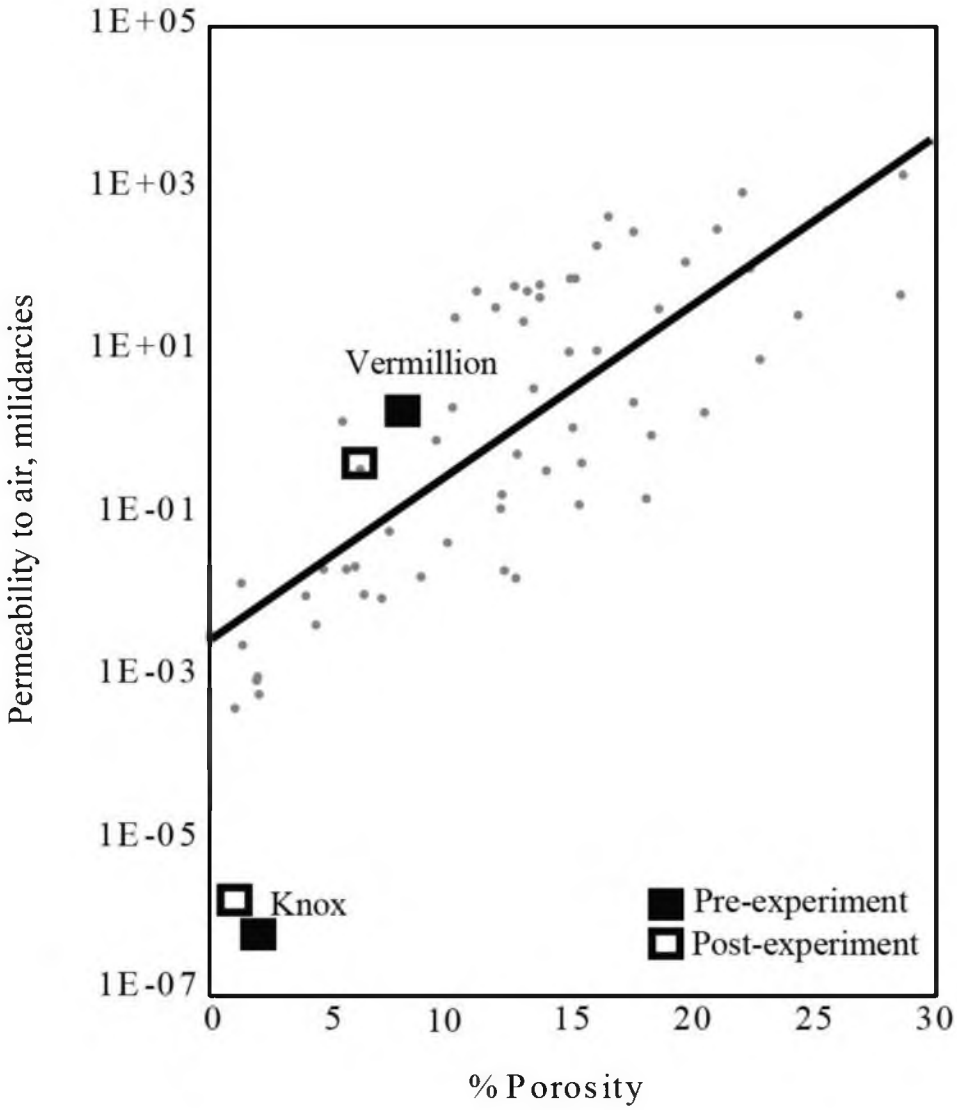
1E+05
1E+03
1E+01
1E-01
1E-03
1E-05
1E-07
Permeability to air, millidarcies
Vermillion
Knox
Pre-experiment
Post-experiment
0
5
10
15
20
25
30
% Porosity

Figure 6. Petrographic micrographs of Experimental B thin sections. Annotations on micrographs: (A) authigenic minerals, (Q) Quartz grains, (F) K-feldspar stained yellow, (P) Pore space filled with blue epoxy, and (Qo) Quartz overgrowth. Micrographs (A)-(D) are taken from the Knox sample and (E)-(H) are from the Vermillion sample. (A) Example of Knox textures and composition revealing an abundance of K-feldspar and low porosity. (B) Macroscale pore containing detrital and authigenic feldspars and clays. (C) Extensive fracturing spanning a variety of minerals. (D) Detrital muscovite emplaced on top of feldspar and quartz grains. Low porosity in the sample is a result of extensive quartz overgrowths. (E) Example of Vermillion textures compositions in transmitted plane-light at 2.5 X magnification revealing a lower amount of K-feldspar and higher porosity. (F) Partial dissolution of feldspar grain creating secondary porosity. (G) Iron oxide rim and quartz overgrowth surrounding round quartz grain. (H) Secondary porosity occurring around quartz grain with clay coatings.

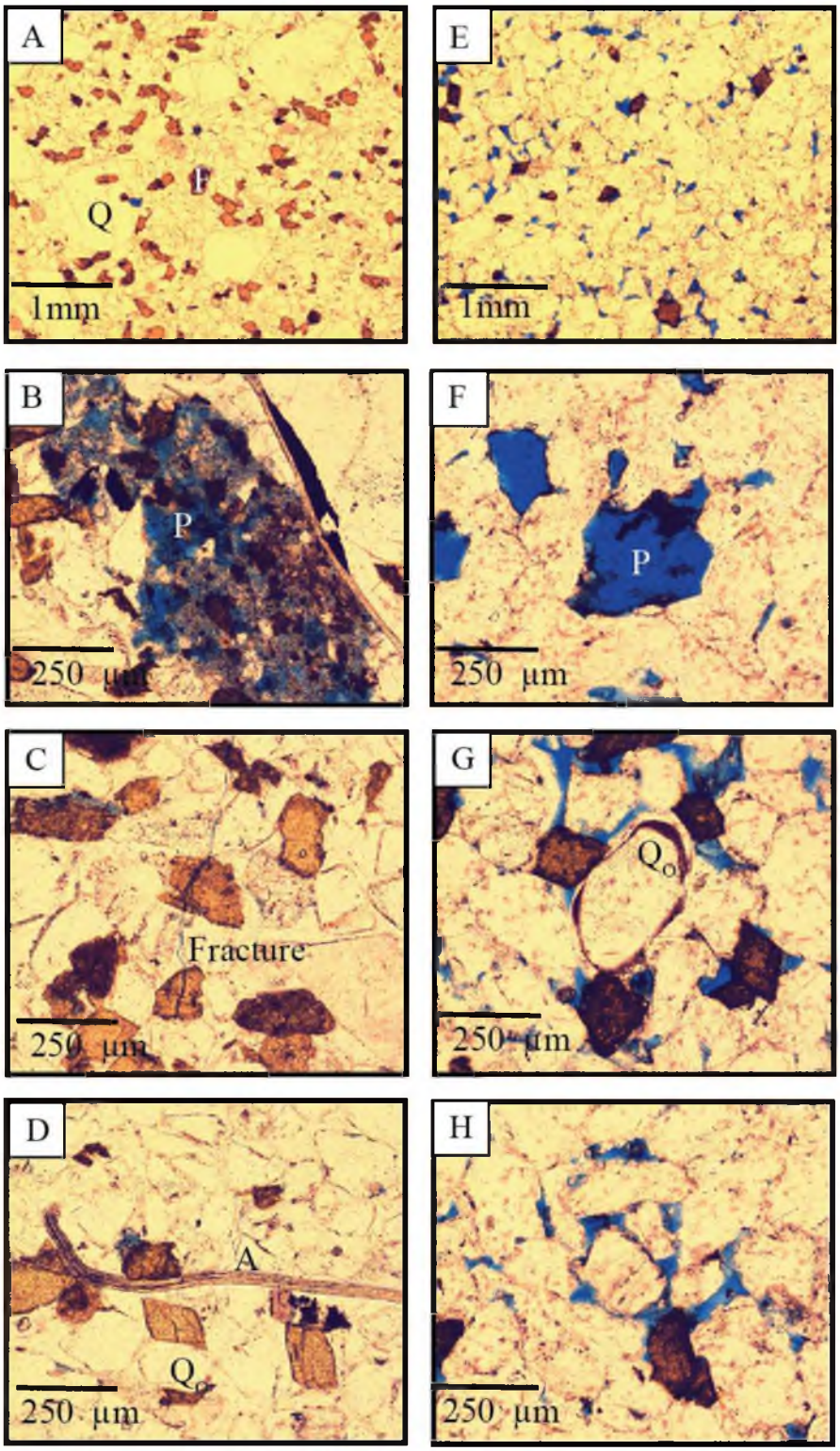
A
Q
F
1mm
E
1mm
B
P
250 µm
F
P
250 µm
C
Fracture
250 µm
G
Qo
250 µm
D
A
Qo
250 µm
H
250 µm

Figure 7. Summary of Experiment B and nonexperimental point count results. (7A) The left panel shows the point count comparison of quartz and feldspar minerals in experimental and nonexperimental samples to previously measured Mount Simon Sandstone samples. The right panel shows the point count comparison of porosity to authigenic minerals in experimental and nonexperimental samples compared to previously measured Mount Simon Sandstone samples. (B) Summary of 600 grain size measurements of nonexperimental Knox grains taken from proximal locations. Larger symbols are the average grain size of the mineral. (C) Summary of 200 grain measurements of experimental Knox grains. (D) Summary of 200 grain measurements of nonexperimental Vermillion grains. (E) Summary of 200 grain measurements of experimental Vermillion grains.

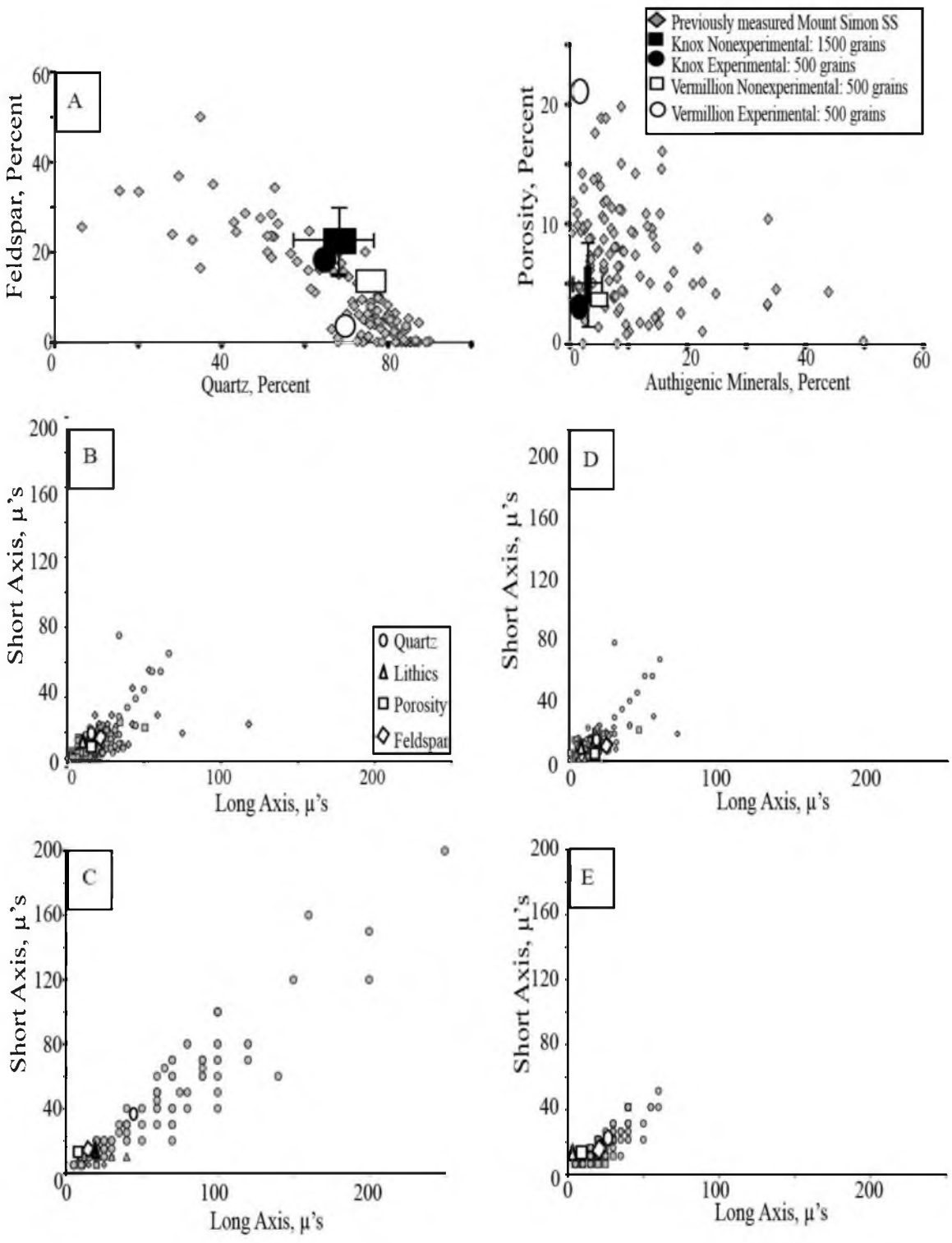
A
Feldspar, Percent
Quartz, Percent
Previously measured Mount Simon SS
Knox Nonexperimental: 1500 grains
Knox Experimental: 500 grains
Vermillion Nonexperimental: 500 grains
Vermillion Experimental: 500 grains
Porosity, Percent
Authigenic Minerals, Percent
B
Short Axis, µ's
Long Axis, µ's
Quartz
Lithics
Porosity
Feldspar
D
Short Axis, µ's
Long Axis, µ's
C
Short Axis, µ's
Long Axis, µ's
E
Short Axis, µ's
Long Axis, µ's

Figure 8. Summary of EDX pore analysis results. (A) Fe-Ti ratio comparison for both samples at each zone. (B) Al to K- ratio comparison for both samples at each zone. (C) Mg-Ca ratio comparison for both samples at each zone. (D) Surface area measurements show the largest pores in the Knox sample are located at the edge whereas the Vermillion sample has more uniformly distributed pores across the three zones.

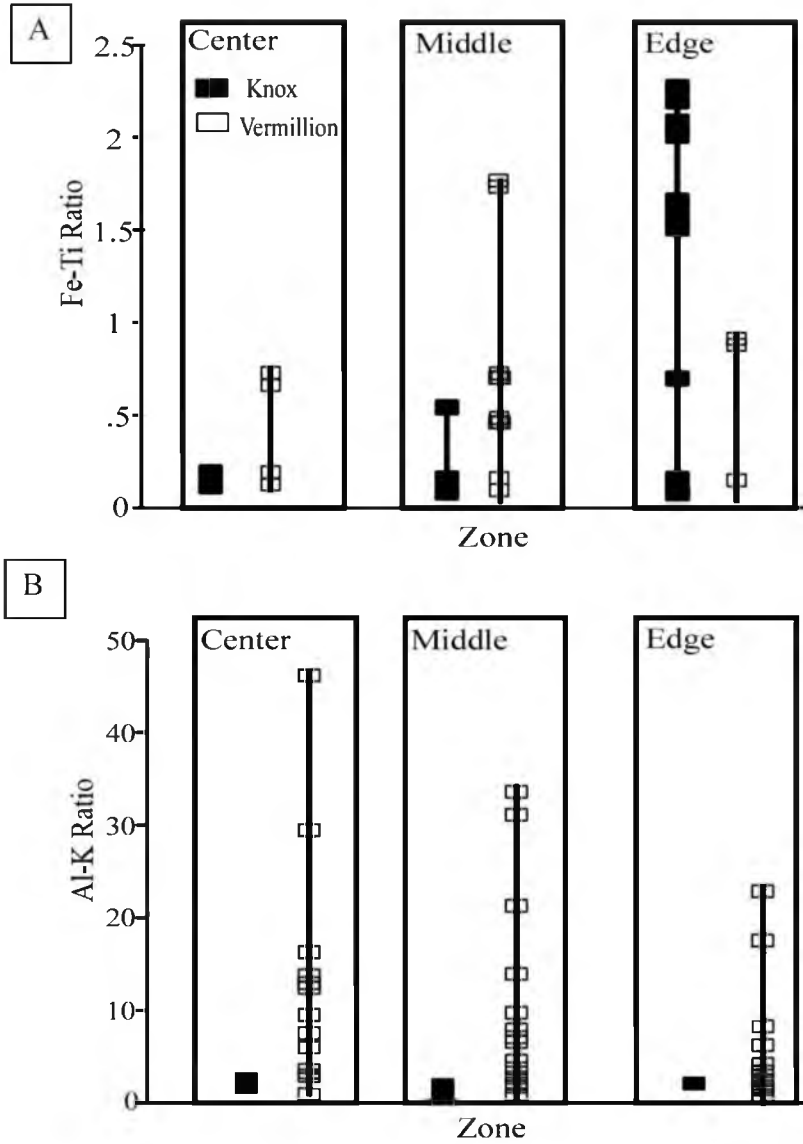
A
Center
Middle
Edge
Knox
Vermillion
Fe-Ti Ratio
2.5
2
1.5
1
.5
0
Zone
B
Center
Middle
Edge
Al-K Ratio
50
40
30
20
10
0
Zone

C
Center
Middle
Edge
10
8
6
4
2
0
Mg-Ca Rato
Zone
D
50000
45000
40000
35000
30000
25000
20000
15000
10000
5000
0
Pore Surface Area, μ²
Center
Middle
Edge
Zone

Figure 9. Pore characterization summary from Experiment B samples. The Vermillion results are shown as the white filled bars and the Knox as the black filled bars. (A) Histogram of pore morphology results. Figure axis labels: R=Round, E=Etched, I=Irregular. Vermillion pores in the center and middle zones contain a relatively similar mineral distribution but becomes more quartz/nonquartz/clay dominated at the edges. No pores in the Vermillion sample contained just clays, which differs from the Knox sample. Knox pores indicate all types of minerals are found in pores across all zones of examination. (B) Histogram of microporosity characterization results. Figure axis labels: 1=All Quartz, 2=Quartz and Nonquartz, 3=Quartz, Nonquartz, and Clays, 4=All Clays. Knox pores are typically low in microporosity across all zones while Vermillion pores have less pore-filling material. (C) Histogram of pore morphology characterization results. Figure axis labels: L=Low, M=Medium, H=High. Knox pores show a wide distribution of pore shapes while the Vermillion sample are etched at the center and middle zones and irregular at the edges.

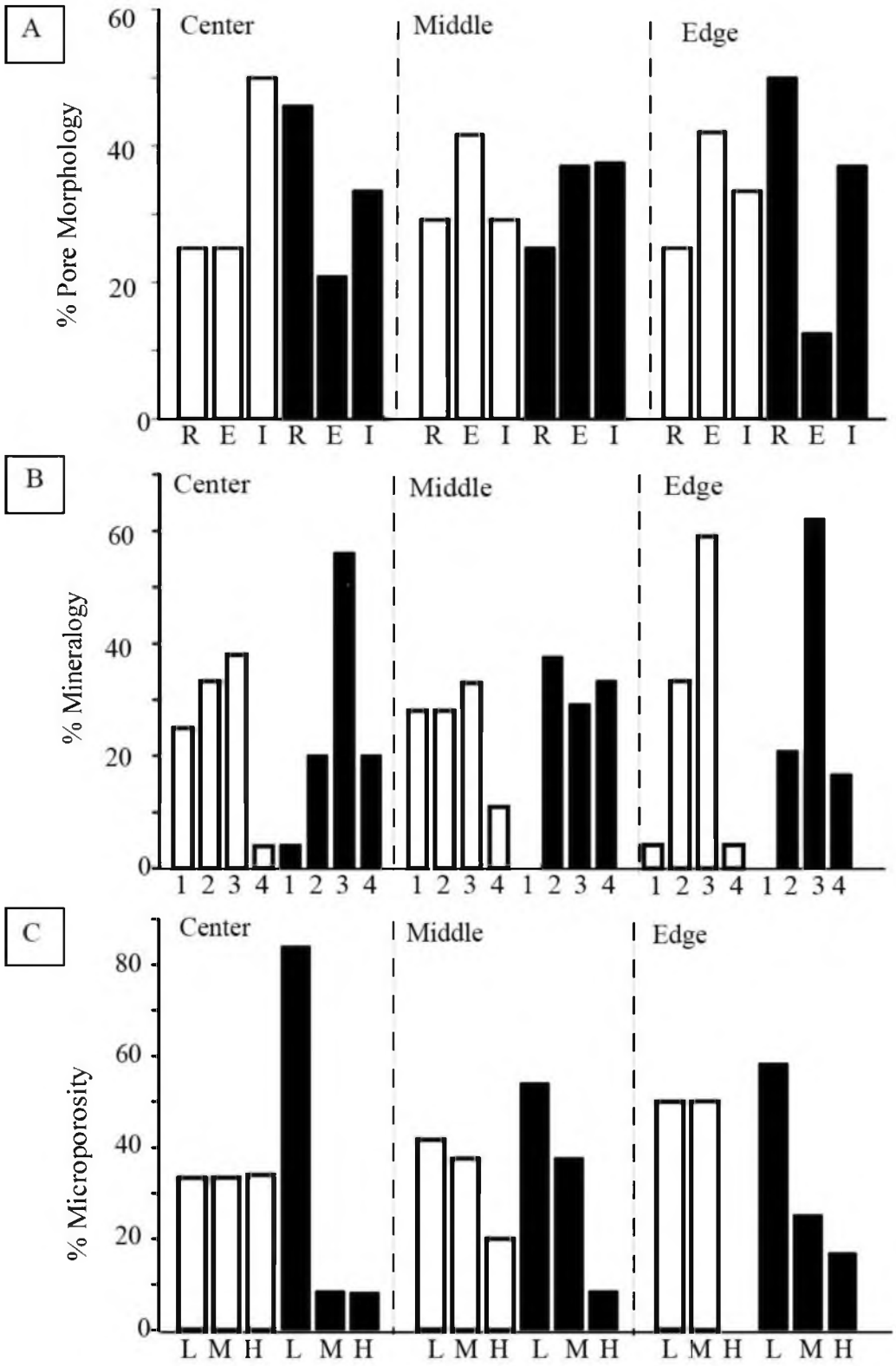
A
Center
Middle
Edge
% Pore Morphology
60
40
20
0
R E I R E I R E I R E I R E I R E I
B
Center
Middle
Edge
% Mineralogy
60
40
20
0
1 2 3 4 1 2 3 4 1 2 3 4 1 2 3 4 1 2 3 4 1 2 3 4
C
Center
Middle
Edge
% Microporosity
80
60
40
20
0
L M H L M H L M H L M H L M H L M H

Figure 10. Selected brine chemistry results for Knox and Vermillion. All elemental concentrations increased after the experiment, suggesting no precipitation of phases.

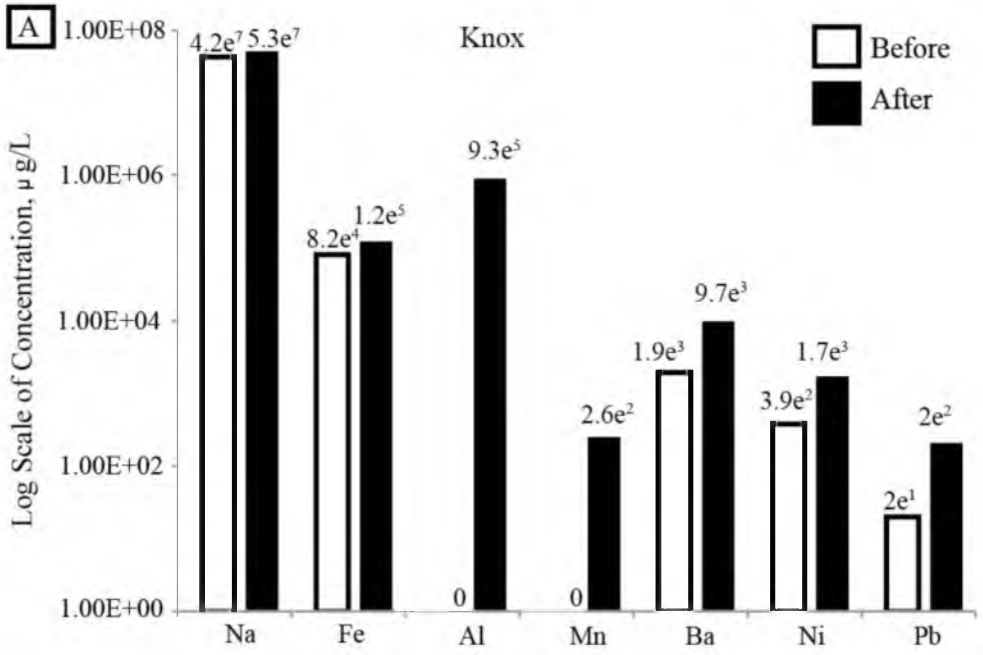
A
Knox
Before
After
Log Scale of Concentration, µ g/L
1.00E+08
1.00E+06
1.00E+04
1.00E+02
1.00E+00
4.2e7
5.3e7
8.2e4
1.2e5
0
9.3e5
0
2.6e2
1.9e3
9.7e3
3.9e2
1.7e3
2e1
2e2
Na
Fe
Al
Mn
Ba
Ni
Pb

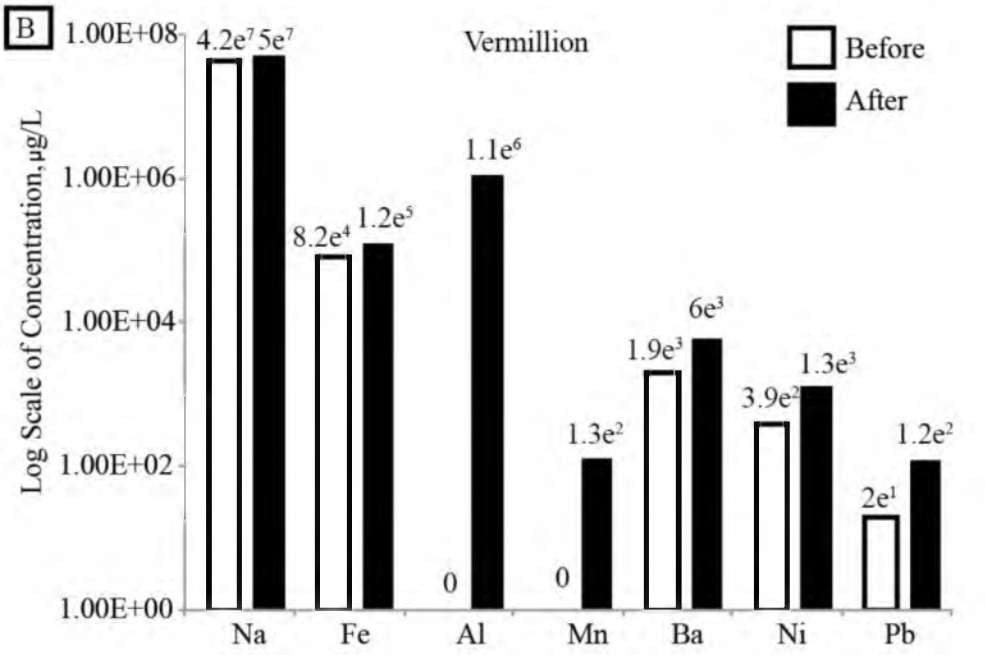
B
Vermillion
Before
After
Log Scale of Concentration, µg/L
1.00E+08
1.00E+06
1.00E+04
1.00E+02
1.00E+00
4.2e7
5e7
8.2e4
1.2e5
0
1.1e6
0
1.3e2
1.9e3
6e3
3.9e2
1.3e3
2e1
1.2e2
Na
Fe
Al
Mn
Ba
Ni
Pb

Figure 11. Comparison of mineral saturation and pH variations. (A) Bulk comparison of the two samples showing variations in mineral saturation. (B) Pore comparison showing very low saturation rates for both samples. (C) 6-month comparison of pH for the bulk and pore samples reveal very different reaction paths. (D) 1000-year comparison of pH for the bulk and pore samples reveal very different reaction paths.

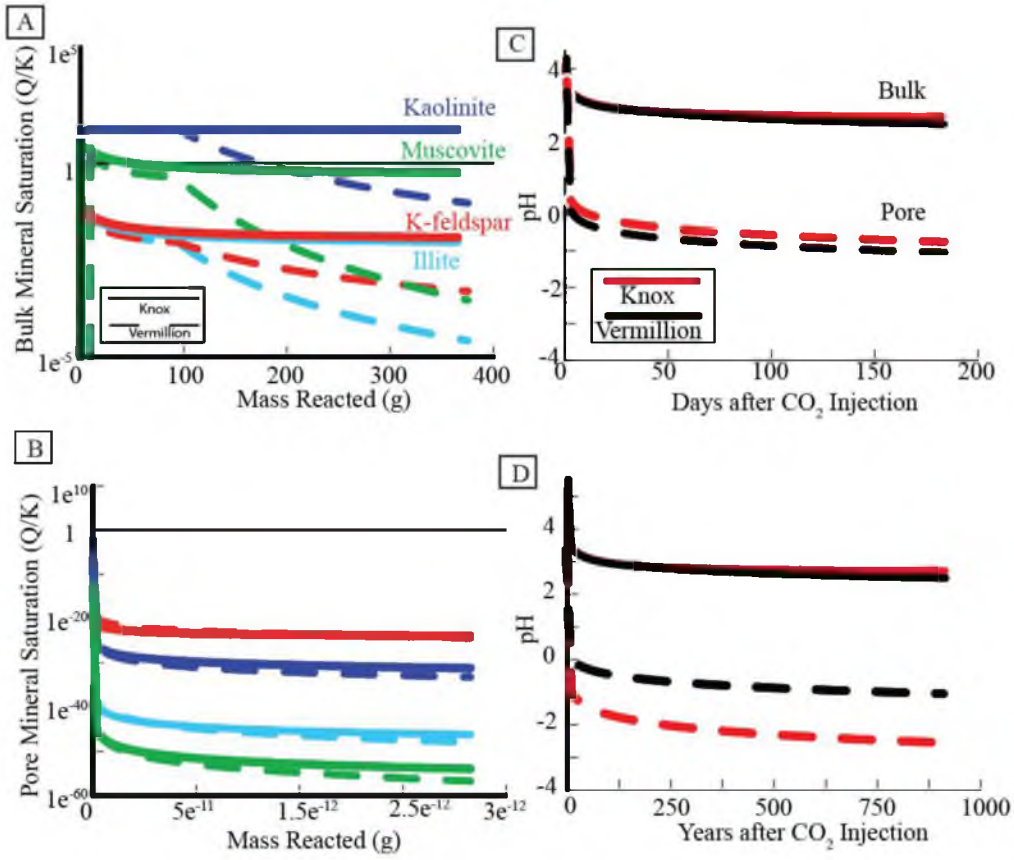
A
Bulk Mineral Saturation (Q/K)
1e5
1
1e-5
Kaolinite
Muscovite
K-feldspar
Illite
Knox
Vermillion
0
100
200
300
400
Mass Reacted (g)
C
pH
4
2
0
-2
-4
Bulk
Pore
Knox
Vermillion
0
50
100
150
200
Days after CO2 Injection
B
Pore Mineral Saturation (Q/K)
1e10
1
1e-20
1e-40
1e-60
0
5e-11
1.5e-12
2.5e-12
3e-12
Mass Reacted (g)
D
pH
4
2
0
-2
-4
0
250
500
750
1000
Years after CO2 Injection

Figure 12. Summary of mineral saturation amounts with variable porosity. A moderately-high porosity of 10% and high porosity of 20% were measured with gram per porosity amounts of 1 and .6 grams. (A) Comparison of mineral saturation in Knox samples with 10% porosity varying the mass dissolution amounts. (B) Comparison of mineral saturation in Knox samples with 20% porosity varying the mass dissolution amounts. (C) Comparison of mineral saturation in Vermillion samples with 10% porosity varying the mass dissolution amounts. (D) Comparison of mineral saturation in Knox samples with 20% porosity varying the mass dissolution amounts.

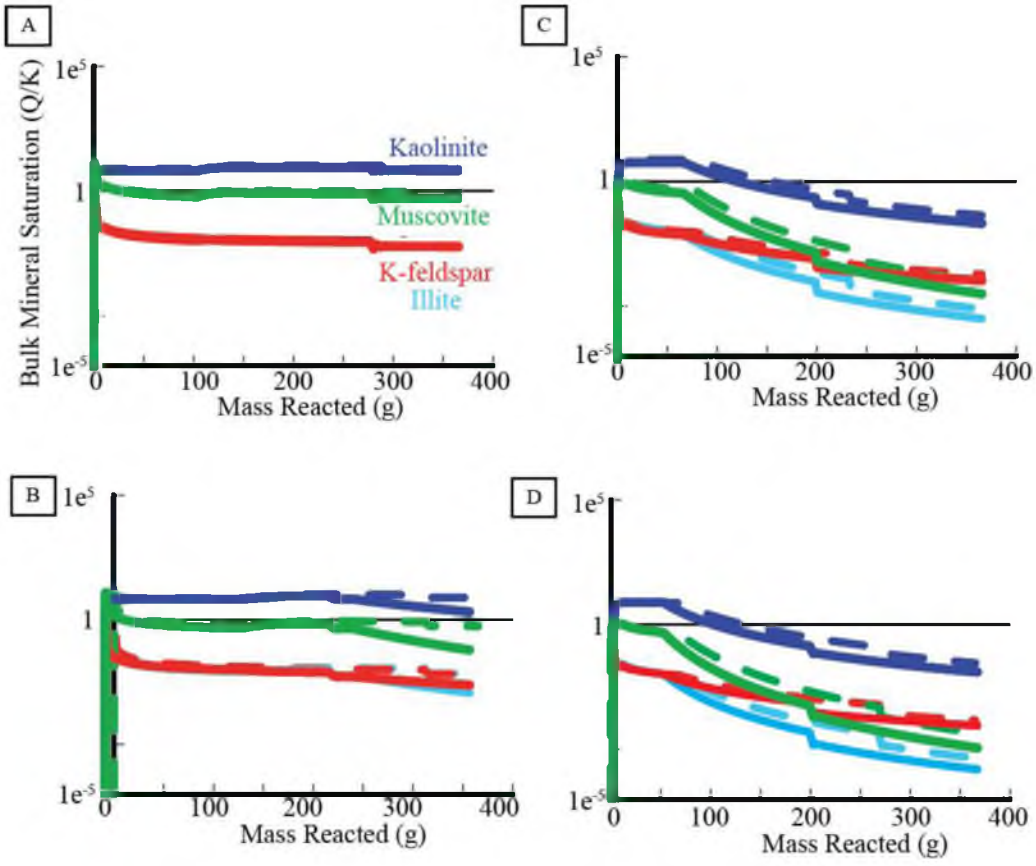
A
B
C
D
Bulk Mineral Saturation (Q/K)
1e5
1
1e-5
Kaolinite
Muscovite
K-feldspar
Illite
0
100
200
300
400
Mass Reacted (g)

Table 5. Summary of mineral inputs for bulk model in Geochemist Workbench

Knox Minerals	Mineral Amount, Moles	Mineral Amount, Percentage	Kinetic Rate (mol/cm^2 s^{-1})	Surface Area (cm^2/g)
Quartz	6.90E-01	76%	1.00E-16	5886.5
K Feldspar	4.60E-02	21%	1.00E-10	370.51
Kaolinite	4.73E-03	2.00%	1.00E-16	17.88
Illite	7.83E-04	0.50%	4.00E-16	11.21
Muscovite	1.15E-03	0.75%	1.00E-16	10.67
Vermillion Minerals	**Mineral Amount, Moles**	**Mineral Amount, Percentage**	**Kinetic Rate (mol/cm^2 s^{-1})**	**Surface Area (cm^2/g)**
Quartz	1.02E+00	93%	1.00E-16	5886.5
K Feldspar	1.19E-02	5%	1.00E-10	74.1
Calcite	1.92E-03	0.75%	1.00E-08	44.28
Kaolinite	1.27E-03	0.75%	1.00E-16	17.88
Illite	8.28E-04	0.50%	4.00E-16	5.6

Mineral concentration and surface area measurement were taken from point counting results. Kinetic rates were adapted from Kharaka (2004) and Nondorf (2010).

Table 6. Summary of mineral inputs for pore-scale model in Geochemist Workbench

K Feldspar	Quartz	Illite	Calcite	Albite	Knox
1.81E-10	1.35E-08	8.32E-11	6.50E-11	3.42E-11	Average
1%	97%	1%	0%	0%	Percent
2.31E-10	1.05E-08	8.06E-11	1.27E-09	3.38E-11	High Ca
2%	87%	1%	10%	0%	Percent
1.12E-10	1.35E-08	9.27E-11	5.76E-10	0	High Mg
1%	95%	1%	4%	0%	Percent
7.78E-10	1.2E-8	5.44E-11	0	4.90E-11	High K
6%	93%	0%	0%	0%	Percent

K Feldspar	Quartz	Illite	Calcite	Albite	Vermillon
6.44E-10	3.22E-07	2.37E-10	1.97E-09	1.39E-09	Normal
0%	99%	0%	1%	0%	Percent
1.46E-09	3.71E-07	1.61E-09	8.88E-09	1.08E-08	High Ca
0%	94%	0%	2%	3%	Percent
9.88E-10	2.46E-07	1.92E-09	8.78E-09	1.34E-08	High Mg
0%	91%	1%	3%	5%	Percent
7.70E-08	3.64E-07	1.29E-09	3.14E-09	3.43E-08	High K/Na
16%	76%	0%	1%	7%	Percent

Minerals were constructed from EDX data of the 144 pores examined

DISCUSSION

Petrographic and geochemical analyses and modeling of the Mount Simon Sandstone reveal how porosity and mineral abundance influence the types of reactions that occur with CO_2 injection and also provide unique insights into the complex diagenetic history of the reservoir and how spatial variations impact the way that the reservoir reacts with CO_2. The results from the Batch A experiment provide insights on the abundance and stability of the detrital and authigenic feldspars when exposed to sequestration conditions, which has implications for the development of secondary porosity and potential flow paths postinjection as well as the availability of cations for subsequent mineral sequestration. The results of the Batch B experiment show how inherent compositional and textural differences impact the amount of dissolution and precipitation that occurs over both a short and long term (Table 7).

Quartz

Quartz, the most abundant mineral in the formation, displays heterogenous textures and grain sizes that are the result of a range of tectonic and diagenetic conditions and influence the distribution and type of porosity. Quartz amounts derived from point counting of reacted and unreacted samples range between 58% to 78% and textures vary widely between very round to highly fractured (Figure 7). Quartz overgrowths, the most common cements, occur as multiple generations and constitute at least 2% of total composition based on modeling results in the basin at depths between 5,000-8500 ft

under a wide variety of temperature, pressure, and mineral textures in the Illinois Basin (Makowitz et al., 2006). Many of the quartz grains show multiple generations of cementation, which is the major porosity-reducing process in in deep, quartzose sandstones (Figure 6C) (Walderhaug, 1996). Petrographic and modeling results indicate the compaction exerted on the deeper Knox sample created extensive fractures in quartz grains, which were filled with silica-rich fluids that mineralized to form multiple generations of quartz overgrowths. Conversely, the Vermillion sample that has roughly the same quartz amount but smaller and rounder grain size has a higher potential for future development of secondary growths and clay rims because of the higher amount of potential reactive surface area and contact with pore fluids.

The distribution of quartz grain morphologies is influenced by the initial sediment distribution and subsequent diagenetic and structural alterations that occur. Well-rounded quartz grains observed in the Mount Simon Sandstone are often found coated with overgrowth-inhibiting clays that are precipitated from fluids found in pore spaces (Stoessel and Pittman, 1990). Highly fractured quartz grains, formed from compaction events or structural deformation, create fresh, reactive surfaces where nucleation of quartz cements can potentially occur which reduces porosity (Makowitz et al., 2006). Petrographic observations of reacted and unreacted samples found the fractures are typically angular, thin and often span multiple quartz and feldspar grains (Figure 6C). Results of mineral angularity from point counting indicate variability in the morphology of Knox and Vermillion quartz grains. Thirty-six percent of the quartz grains measured from unreacted Vermillion sample were identified as subangular to very angular compared to 45% of quartz grains in the Knox sample. Measurements of quartz grains

from reacted samples show the average quartz grain and overgrowth in the Knox, 46µm x33.8µm, is nearly twice the size of Vermillion grains (Figure 6). SEM images at 300x magnification further illustrate the widespread distribution of quartz overgrowths, sutured grain contacts, and fractured grains present in the Knox sample (Appendix A). Vermilion quartz grains under SEM examination are rounder, surrounded by intergranular porosity, and have grain coatings.

Quartz, along with all minerals in the bulk composition model, were assumed to be spherical grains that have the lowest surface area to volume ratio, which may potentially underestimate the actual surface area because of the amount of fractured grains found in the samples. To balance this assumption, porosity amounts of 2% in the Knox Co., IN 8642.5-B sample and 8% in Vermillion Co., IN 5806-B were included to reflect the difference in grain spacing between the two samples. The purpose of this model was to determine if quartz saturation rates vary between two samples with similar quartz amounts but different porosities and surface areas. Reaction path modeling shows quartz very rapidly reaches chemical equilibrium for both samples during both 6-month and 1,000-year scenarios, which was also found in a previous experimental study using Mount Simon Sandstone compositions (Figure 11A and D) (Basahov et al., 2013). This result is not typical in nature as silicate minerals are seldom found in equilibrium with brines (Bethke, 2008). It has been proposed this discrepancy in equilibrium exists because of existing clay coatings on reactive surfaces in aquifers inhibiting overgrowths or the presence of other minerals that produce and consume silica (Bethke, 2008). Accurate estimation of mineral surface area and consideration of the impurities that naturally occur in silicate minerals must be balanced with the feasibility of accounting for

the entire system's reaction process. Quartz grains found under petrographic analysis are often rimmed with clay and/or hematite grains, display an unsystematic array of edges and round surfaces, and are surrounded by feldspars and open pore spaces (Figure 6E-H). Under laboratory conditions, quartz grains are typically removed of any coatings and can have sharp, more reactive edges where nucleations can occur (Bethke, 2008). More accurate prediction of future alterations can be reconstructed by integrating empirically derived data with experimental results (Walderhaug, 1996; Makowitz et al., 2006; Bethke, 2008).

Previous studies have shown that silica-rich fluids can precipitate at temperatures ranging from 60°C to 90-100°C depending on the salinity of the pore fluid with which the quartz is reacted (Mcbride, 1989). Kinetic modeling of the source of quartz cementation has shown to be complex because of the factors that contribute to the release of silica and identification of source. Initially, it was believed pressure was the primary control on the release of silica that accumulates on grains, resulting in secondary cements (Stephenson et al., 1992). It has also been proposed that silica is sourced from stylolites and diffusion that occurs at quartz-clay grain contacts (Walderhaug, 1996). The algorithm in this study found that grain size, clay coatings, and temperature have a significant impact on cementation while compositionally, a quartzarenite and arkosic sandstone varied by less than 4% (Walderhaug, 1996). In this scenario, the smaller quartz grains and higher porosity amount found in the reacted Vermillion sample compared to the Knox sample indicate a higher potential for both future development of clay coatings and cementation depending on what ions are mobilized in the pores with the introduction of CO_2.

Feldspar

The examination of feldspar dissolution has been shown to aid in predicting the amount of CO_2 trapping that occurs in saline reservoirs (Rosenbauer et al., 2005; Wigand et al., 2008; Liu et al., 2011; 2013; Balashov et al., 2013). The abundance of authigenic and detrital feldspars, primarily K-feldspar, plays a significant role in the creation of existing and future porosity as it constitutes nearly 50% of some samples observed in the Mount Simon Sandstone (Figure 7A) (Surdam et al., 1984; Stoessel and Pittman, 1990). Dissolution of feldspars can lead to the formation of porosity but can also lead to formation of diagentic clays in pores and release of silica, which can be a source of quartz cementation (Heald, 1973; Bowen et al., 2011). The presence of CO_2 in the system accelerates the dissolution rate of aluminosilicates and mobilizes K, Al, and Si (Stoessel and Pittman, 1990). A prior study that modeled the reaction of minerals in the Mount Simon Sandstone under sequestration conditions found the entire volume of K-feldspar, 21%, had reduced to nearly zero while alunite and anhydrite, products of mineral precipitation in the brine, formed at the end of the 10,000-year simulation (Liu et al., 2011).

Identification of K-feldspar amount and composition in the samples revealed an abundance of both detrital and authigenic forms. The difference in feldspar composition between the grains and overgrowths suggests the presence of several feldspar polymorphs. Detrital K-feldspars are potentially orthoclase sourced from high-temperature metamorphic gneiss. At high temperatures, the structural arrangement of atoms on the crystal structure decreases, resulting in a more disordered mineral form, which may explain the less pure, monoclinic orthoclase form (Dyar and Gunter, 2007).

Conversely, as temperatures decreases and cooling slows due to the presence of formation brines in the system, the existing crystal structure will favor a more stable arrangement, creating the authigenic, microcline overgrowths with a triclinic habit (Dyar and Gunter, 2007). Similar compositional differences were identified in the arkosic Triassic Buntsandstein sandstone using SEM/EDX and cathodoluminescence (CL) analysis (Morad et al., 1989). The authors argue the formation of K-feldspar pseduomorphs occurs through the process of incomplete dissolution-precipitation occurring in the intercrystalline porosity located in detrital K-feldspar grains. The process begins with the instantaneous exchange of H^+ for alkali ions K^+ and Na^+ followed by the formation of Al-Si structures, which acts as the basis for which K^+ attaches and eventually forms authigenic K-feldspar (Morad et al., 1989). Differentiating overgrowths from detrital grains not only provides insights into the thermal history of the Mount Simon Sandstone but also towards a better understanding of the preferential dissolution that occurred during the experimental process.

The variability of authigenic and detrital feldspar morphology at different depths of the Mount Simon Sandstone indicates authigenic K-feldsapr grains were derived from several sources. Petrographic results suggest porosity amount influences the precipitation and dissolution of authigenic K-feldspar as being derived from transport of pore fluids or nucleation at reactive surfaces. In areas of moderate porosity such as in Vermillion Co.IN 5806-B, grain boundaries in detrital feldspars are significant because they are constant contact with pore fluids and CO_2, which create areas of weakness where authigenic minerals can precipitate. Authigenic, rhombic K-feldspar minerals were found extensively in pore spaces and extensive quartz grain coatings in these samples indicate

solution transport could be responsible the formation of authigenic minerals (Figure 5D) (Duffin, 1989). Conversely, the Knox 8642.5-B sample with low porosity is more likely to develop porosity localized in areas of existing grain weakness such as microfractures where potential nucleation of overgrowths is favorable. Cleavage surfaces such as orthoclase twinning and tartan twinning in microcline are also areas where mineral precipitation can occur (Morad et al., 1989). Feldspar overgrowths often lack twinning because they are composed of many discrete crystals rather than one elongate crystal (Morad et al., 1989).

The variations in feldspar composition and morphology identified in the experimental samples likely result in precipitation and dissolution rates that differ from the standard feldspar inputs in Geochemist Workbench. The feldspar minerals were created to evaluate how variations in porosity and abundance and in the presence of other minerals impact the mineral's saturation rate. Saturation of simple minerals in GWB are calculated from the dimensionless ξ variable, which is based purely on the amount of mineral that is reacted. The inclusion of kinetic rates and surface area measurements based on petrographic results and sequestration conditions allows for more accurate dissolution and precipitation rates (Bethke, 2008). According to transition state theory, from which surface area reactions were derived in previous literature, dissolution rates are controlled by the rate at which activated complexes, intermediate chemical structures that form from the interaction of the product and reactant, decay rather than the mineral's saturation state (Lasaga, 1981; Bethke, 2008). Precipitation rates are influenced by saturation states and are positive when Q, the reaction quotient, exceeds K, the equilibrium constant (Bethke, 2008). Mineral saturation results of feldspar grains

modeled from kinetic rates calculated at 100 C, pH of 4, mass based on point counting results, and helium-injection porosity measurements found neither sample's brine precipitated K-feldspar during both the 6-month and 1000-year periods in the bulk models (Kharaka, 2004). Significant undersaturation of K-feldspar occurs in the pore scale for both samples, which is the result of the high concentration of CO_2 present in the system that drops the pH rapidly (Figure 11). The pore scale model allowed for the creation of mineral surface areas unique to the size of pore, but this did not significantly change the saturation state of the two samples, likely due to the scale of reactions that occurred. Similarly, the comparison between maximum and mean K amounts, which was a proxy for K-feldspar amount, resulted in indiscernible differences in saturation amounts in pores.

Results from the Vermillion 5806 sample in the Batch A experiment found feldspar overgrowths underwent more pronounced dissolution than the less pure, detrital grains. The implications of this are significant because overgrowths in the Mount Simon Sandstone can constitute as much as 20-30% of the total feldspar volume in a sample (Brophy, unpublished data). Total feldspar amount in some samples can be as high as 50%, meaning dissolution of overgrowths can increase porosity by up to 15% if no re-precipitation occurs. Further, electron microprobe analysis conducted on samples from the Vermillion core identified feldspars as primarily being orthoclase with compositions ranging from Or_{92-99} but also contains albite, the sodium end member, with ranges between Ab_{1-8}. Anorthite, the calcium feldspar endmember, was absent. The detrital grains should undergo less dissolution because they are already saturated in sodium; thus, less exchange with H^+ would occur when in contact with the formation brine and CO_2.

Clay Minerals

The experimental samples contain both detrital and authigenic clays such as illite, kaolinite, and chlorite, which form from the dissolution of feldspar grains and through precipitation-saturated formation brines (Bowen et al., 2011). The experimental samples contain both detrital clays and authigenic clays mechanisms that form from the dissolution of feldspar grains and through precipitation of ion-saturated formation brines. Clay coatings of quartz grains are significant in determining porosity and permeability because they deter quartz overgrowths, especially with chlorite (Pittman et al., 1992). The authors attribute the preservation of porosity in deeply buried sandstone reservoirs to clays that develop on potential nucleation sites.

Pore characterization results show the mineralogical composition of both Experiment B pores mostly contain a variety of quartz, feldspars, and clays, although pores with one mineral type were also found. The mineralogy present in the pores helps to predict the types of secondary growths on surrounding quartz grains that may develop during long-term CO_2 storage and further provides insights on how porosity controls the types of minerals are preserved in pores. Knox 8642.5-B pores, on average ten-times smaller than Vermillion 5806-B pores, contain diverse mineral assemblages and were more likely to have just clays present across the three zones (Figure 9A). These pores are also on average rounder and contain lower microporosity amounts than the larger pores (Figures 9B and 9C). The low porosity in Knox 8642.5-B helps to preserve pores that are highly filled with clays and contain diverse mineral assemblages after exposure to CO_2 sequestration conditions. Conversely, the larger pores and higher porosity amount in Vermillion 5806-B increased the mineral's exposure to pore fluids and CO_2, resulting in

pores with moderate microporosity and containing minerals that are more resistant to dissolution than clays.

The development of clay coatings on quartz grains in the Vermillion sample may have helped to preserve the round to subangular texture and less pronounced overgrowths. Knox clay formation is likely confined to areas of weakness such as grain fractures and cleavage planes due to the low permeability, which reduces the transport of fluids. The introduction of CO_2 may potentially be disruptive to the formation of clay coats since this process typically occurs in stages where a substrate layer must first form and then sequential layers build up, provided there is a constant source of clay-building material (Pittman et al., 1992). As observed in the pore-scale model, a dramatic change in pH would dissolve and mobilize phyllosilicates in pores and similarly disrupt the formation of immature clay grain coatings.

Carbonates

The rapid rise in pH that occurs immediately after the beginning of the reaction in the bulk Vermillion sample could be attributed to the presence of calcite, an important mineral buffer (Rosenbauer et al., 2005; Newell et al., 2008). The Vermillion sample has a smaller mass of reactive minerals than the Knox sample but reaches a higher pH of 4.4, initially because of a small, .005 m, concentration of $CaCO_3$. The result is the calcite, which has the fastest kinetic rate of all minerals in the system, is consumed rapidly, providing an ephemeral buffer lasting .013 days, roughly 30 minutes, with the brine and CO_2 before it is incorporated into solution and forms excess CO_2. The first reaction is likely to create excess HCO_3, the more dominate carbonate species at the initial pH,

driving the system to become more alkaline according to the activity log series of carbonates outlined in (Drever, 1997).

$$H_2O + CaCO_3 \rightarrow Ca^{2+} + HCO_3 + OH^-$$

As $CaCO_3$ becomes consumed and the buffer is depleted, CO_2 in the form of carbonic acid becomes the primary carbonate species that is formed (Drever, 1997).

$$H_2O + CaCO_3 \rightarrow Ca^{2+} + CO_2 + H_2O$$

The calcite that acted as a buffer in the initial reaction step is eventually consumed by the brine and converted to excess CO_2 to drop the pH of the brine below the initial value, thus accelerating the amount of dissolution that takes place. The Knox sample is absent of calcite, and shows a less pronounced buffer peak but also stabilizes sooner at a slightly higher pH compared to the Vermillion at 6 months (Figure 11C&F). This result is likely to occur because there was no addition of excess CO_2 into the system from calcite, which prolongs the system from reaching equilibrium. Further, all of the mineral saturation states except quartz for both 6-month and 1000-year scales are more undersaturated in the brine, indicating more extensive dissolution occurred in the Vermillion sample compared to Knox due to higher porosity amount (Figure 11). The proposed secondary minerals that form from the dissolution of K-feldspar seen in Liu's (2011) analysis were not seen in either sample, but higher saturation states of these minerals were seen in the Knox sample. Calcite was found in both Experimental B

samples pore model samples but did not react as a buffer in this "closed system" as it did in the bulk model sample.

Porosity and Permeability

Examination of the development of secondary porosity provides insights on the variability of the diagenetic process and assessment of CO_2 storage potential. Secondary porosity is characterized as the porosity that forms from dissolution of minerals while primary porosity is the space that exists between minerals during initial deposition. In natural systems, the creation of secondary porosity in sandstone reservoirs has been debated to be the result of dissolution that occurs from interaction with organic acids to carbonic acids (Surdam et al., 1984; Stoessel and Pittman, 1990). One of the first studies to examine how partial dissolution of feldspars created excess porosity in the Mount Simon Sandstone argued that secondary porosity can be significant even if primary porosity is depleted (Heald and Larese, 1973). Mineral saturation results indicating higher rates of K-feldspar dissolution in the Vermillion sample likely are the product of lower amount of the mineral and higher initial porosity. Petrographic and Al/K ratios in EDX data support this hypothesis as nearly all available porosity in Vermillion is the product of partial to near complete dissolution of feldspar grains (Figure 5D). Knox may have larger feldspar content but dissolution would occur at lower rates due to the highly compacted nature of grains, making it difficult for fluids and CO_2 to penetrate grain surfaces. The amount of porosity in the system is a primary influence in the amount of dissolution and/or precipitation that occurs on all scales of examination in this study.

The results of pore characterization suggest that low porosity amounts in the Knox 8642.5-B sample aid in the preservation of minerals present both as pore fillings and pore linings. Even under sequestration conditions, the minerals and fluids present in pores are so tightly confined that CO_2 storage will be low. An interesting result from the pore-scale model is that K-feldspar precipitation is slightly lower in the Knox sample while the pH of the pore is lower than Vermillion. A possible explanation of this is that the surface area of the Knox pore is smaller than Vermillion, which creates a higher concentration of CO_2 in the system, dropping the pH, but a higher concentration of K-feldspar, which slows the dissolution rate.

The bulk model shows how estimates of porosity based on the mass of the sample influence mineral saturation rates over a 6-month and 1000-year scale (Figure 10). Porosity results of Knox 8642.5-B shows a constant mineral precipitation rate at low and moderate porosity values but decreases sharply in a high, 40%, porosity system during both time scales (Table 8) (Figure 10B and10F). The high porosity accelerates the dissolution process, creating a more favorable scenario for a sample with a high K-feldspar concentration. This result demonstrates the influence of porosity on precipitation and dissolution rates for a sample that composition-wise is an attractive prospect for long-term CO_2 storage. Vermillion 5806-B results display an interesting relationship between the two time frames with similar saturation rates at both high and moderate porosities during the experimental time frame but deviate during the 1000-year simulation (Table 9) (Figure 10). The composition of this sample has much less K-feldspar than Knox 8642.5-B, which may explain why it is quickly consumed at all porosity amounts in the short term. The distinct kink in the 1000-year model for mineral

saturation states in Vermillion 5806-B could be a result of the depletion of calcite in the system, which increases the CO_2 concentration, creating a slightly more acidic system as seen in the pH at approximately 400 years (Figure 9D).

The results of modeling porosity variations across long- and short-term time frames for the two samples show how both composition and porosity influence alterations that occur from CO_2 injection. Areas in the formation with this composition have a greater potential of storing CO_2 despite having a lower feldspar content due to the moderate porosity and permeability and developed porosity framework of authigenic and detrital feldspars. Modeling results indicate high (>20%) porosity coupled with a high K-feldspar concentration is the most favorable scenario for long-term storage. Petrographic analysis coupled with geochemical modeling demonstrates the influence of porosity on precipitation and dissolution rates for a sample that composition-wise is an attractive prospect for long-term CO_2 storage.

Reservoir Heterogeneity

The samples from both experiments display compositional and textural features that underscore the inherent variability that exists in the Mount Simon Sandstone. Previous studies have extensively characterized and discussed the origin of the heterogeneities from a variety of perspectives (Mcbride, 1989; Heald, Leetaru, and Mcbride, 2009; Liu, 2010; Bowen et al., 2011). Interpreting results from this study in context with previously published point count data, porosity and permeability measurements, and reaction modeling results of the Mount Simon Sandstone aids in contextualizing the heterogeneities that were found. This study explores how porosity

along with composition act as primarily controls for predicting how the formation will respond during the initial phase of injection of CO_2 and long-term storage.

Another aim of this study is to describe the paragenetic sequence of the Experiment B samples and predict the long-term response to CO_2 injection. The feldspar-rich Knox 8642.5-B sample may have been initially deposited along the flanks of topographic Precambrian basement highs where arkosic-rich sediments accumulated (Leetaru and Mcbride, 2009). Pore fluids migrate through the formation, causing quartz cements and authigenic feldspars to form, which decreases porosity and permeability. As the Illinois Basin continues to form, extensive faulting is occurring, causing structural deformation throughout the formation as evidenced by the fractures that cross cut minerals. These fractures are soon filled once again with pore fluids that further decrease porosity. Results from Experiment A show any CO_2 injected would preferentially dissolve the authigenic feldspar overgrowths. Due to the low porosity of the sample though, very little CO_2 could actually be trapped despite the abundance of reactive minerals present.

The Vermillion 5806-B experimental and nonexperimental samples display a large range of feldspar amount, suggesting it may have formed in a similar environment to the Knox. Quartz overgrowths and authigenic feldspars precipitated from transport of ion-rich pore fluids, but porosity still remained moderate. The sample's depth, lack of fractures, and current porosity indicate it underwent less compaction but has consistently been exposed to pore fluids, which leads to the precipitation/dissolution of minerals. This experimental has a greater potential of storing CO2 despite having a lower feldspar

content due to the moderate porosity and permeability and developed porosity framework of authigenic and detrital feldspars.

The next step in evaluating the Mount Simon as a CO_2 reservoir involves scaling up the modeling to a formation level. This study evaluated samples from the top and bottom of the formation, encompassing very low to moderate porosity and permeability measurements, and low to high feldspar amounts. A possible strategy could involve creating unique areas of stratification within the formation that encompass these compositional properties and creating compositions from previous studies measurements.

Challenges with Modeling

The use of geochemical modeling provides valuable insights into predicting the outcome of long-term CO_2 storage yet is rife with uncertainties that stem from constructing the model's framework. The inclusion of secondary minerals, porosity amount, choice of thermodynamic and kinetic data, and calculation of CO_2 pressure have been shown to impact storage potential estimates (Dethlefsen et al., 2011). In this study, one of the challenges was establishing a reaction path model representative of the location of the experimental plugs and concurrently comparing the results to previous experimental studies. The brine chemistry used to react with the mineral and gases contains a larger variety and higher concentration of cation and trace elements compared to previous studies using formation brine from the Mount Simon Sandstone, which influence the type and amount of minerals that precipitate and dissolve (Liu, 2010; Basahov, 2013). For the bulk-scale model, a grain diameter of .25mm was chosen to isolate the influence kinetic rates have in the system. Grain size measurements for the

secondary minerals and clays were difficult to obtain from point counting results; thus, a uniform grain size helps reduce the variability that exists between samples while still representing the surface area amount for minerals and allowing for a more straightforward approach to vary the scale of the model.

Bulk- and pore-scale modeling revealed issues with modeling mineral saturation states. The ratio of saturation to undersaturation rate for kaolinite is nearly equal for both simulations. In reality, this would not be the case as mineral saturation would be influenced the reaction time. The results suggest reaction rate amounts based on surface area and mineral kinetics rather than time are being plotted. This explains the equal ratios and not observing minerals fluxing between saturation states at given time intervals.

Additionally, several minerals found under petrographic observation could not be included in the reaction models. Hematite is difficult to model because of the alteration that occurs to the system's pH. The inclusion of O_2 is needed in the brine to react with hematite but also increases the eH of the brine. This increased consumption of electrons in the brine results in an initial concentration of H^+ that is higher than what was measured using ICP-MS analysis. When using the REACT module, a fixed cation amount of the mineral must also be included in the initial brine tab. For example, reacting a NaCl brine with K-feldspar cannot occur without the inclusion of K and Al^{3+} in the brine. Additionally, no Ti-bearing minerals or chromite, which have been identified in the formation, are included in the module.

Table 7. Summary of results

Method	Knox	Vermillion
Pre-Experimental Porosity	1.5%	7.9%
Post-Experiment Porosity	1.1% (-27%)	6.3% (-20%)
Pre-Experimental Permeability	19nD	1.6 mD
Post-Experiment Permeability	23 nD (+21%)	.5mD (-69%)
Mineral Composition	Quartz: 71% Feldspar: 20% Authigenic: 1% Porosity: 8%	Quartz: 71% Feldspar: 4% Authigenic: 3% Porosity: 22%
Brine Composition	All major ions and trace elements increased	All major ions and trace elements increased
Pore Surface Area	Center: 1288 μ2 Middle: 628 μ2 Edge: 2747 μ2	Center: 10969 μ2 Middle: 12566 μ2 Edge:12947 μ2
Pore Al/K Ratio	1.39	4.92

Table 8. Summary of mineral inputs for high porosity model.

Knox Minerals	Mineral Amount, Percentage	Mineral Amount 2% Porosity, Moles	Mineral Amount 20% Porosity, Moles	Mineral Amount 40% Porosity, Moles
Quartz	76%	6.90E-01	5.57E-01	4.18E-01
K Feldspar	21%	4.60E-02	3.68E-02	2.76E-02
Kaolinite	2.00%	4.73E-03	3.78E-03	2.84E-03
Illite	0.50%	7.83E-04	6.27E-04	4.70E-04
Muscovite	0.75%	1.15E-03	9.18E-04	6.88E-04
Total	Sample Mass	61 g	48.8 g	36.6 g
Vermillion Minerals	Mineral Amount, Percentage	Mineral Amount 8% Porosity, Moles	Mineral Amount 20% Porosity, Moles	Mineral Amount 40% Porosity, Moles
Quartz	93%	1.02E+00	6.82E-01	5.12E-01
K Feldspar	5%	1.19E-02	9.49E-03	7.11E-03
Calcite	0.75%	1.92E-03	1.53E-03	1.15E-03
Kaolinite	0.75%	1.27E-03	1.02E-03	7.63E-04
Illite	0.50%	8.28E-04	6.62E-04	4.97E-04
Total	Sample Mass	66g	52.8	39.6

Table 9. Summary of mineral inputs for moderate porosity model

Knox Minerals	Mineral Amount, Percentage	Mineral Amount 2% Porosity, Moles	Mineral Amount 20% Porosity, Moles	Mineral Amount 40% Porosity, Moles
Quartz	76%	6.90E-01	5.57E-01	4.18E-01
K Feldspar	21%	4.60E-02	4.09E-02	3.53E-02
Kaolinite	2.00%	4.73E-03	4.20E-03	3.62E-03
Illite	0.50%	7.83E-04	6.97E-04	6.00E-04
Muscovite	0.75%	1.15E-03	1.02E-03	8.79E-04
Total	Sample Mass	61 g	54.25	46.75
Vermillion Minerals	Mineral Amount, Percentage	Mineral Amount 8% Porosity, Moles	Mineral Amount 20% Porosity, Moles	Mineral Amount 40% Porosity, Moles
Quartz	93%	1.02E+00	6.82E-01	5.12E-01
K Feldspar	5%	1.19E-02	1.11E-02	9.70E-03
Calcite	0.75%	1.92E-03	1.80E-03	1.57E-03
Kaolinite	0.75%	1.27E-03	1.19E-03	1.04E-03
Illite	0.50%	8.28E-04	7.75E-04	6.77E-04
Total	Sample Mass	66g	61.8	54

CONCLUSIONS

When dealing with such a complex problem such as CO_2 storage, there is a compromise between capturing the heterogeneous nature of the samples and creating a model that can be replicated not only within the Mount Simon Sandstone but other potential reservoirs. Arriving at this intersection requires both familiarity with the formation being studied and methods to experimentally model these observations to identify the parameters that are key in influencing the model. This study argues that porosity and permeability amounts are fundamental in determining the abundance and distribution of authigenic K-feldspar, the most important mineral for determining CO_2 storage potential.

APPENDIX A

SEM AND EDX ANALYSIS

Table 10. EDX Pore Analysis

Sample	Section	Image #	Distance	Surface Area	C	O
Knox	1P	17160	4	762.351	28.28	44.93
Knox	1P	17161	4	2188.901	23.99	47.55
Knox	1P	17162	4	1419.962	17.45	50.03
Knox	1P	17163	4	503.282	20.27	47.76
Knox	1P	17164	4	909.747	17.9	49.56
Knox	1P	17165	4	353.69	18.57	49.89
Knox	1P	17166	4	421.192	16.43	49.65
Knox	1P	17167	4	515.12	12.33	50.87
Knox	1P	17168	4	996.582	14.4	50.74
Knox	1P	17169	8	288.312	12.63	51.23
Knox	1P	17170	8	204.26	21.42	48.05
Knox	1P	17171	8	330.042	20.22	48.17
Knox	1P	17172	8	918.35	18.91	49.11
Knox	1P	17173	8	592.263	12.06	52.49
Knox	1P	17174	8	626.108	24.81	47.56
Knox	1P	17175	8	771.288	30.32	42.47
Knox	1P	17176	12	1124.642	32.03	42.83
Knox	1P	17179	12	2677.581	39.94	41.41
Knox	1P	17182	12	2725.553	19.3	48.89
Knox	1P	17185	12	868.572	22.26	47.36
Knox	1P	17188	12	661.772	30.84	43.42
Knox	1P	17191	12	663.546	29.16	45.3
Knox	1P	17194	12	795.055	28.06	46.09
Knox	1P	17197	12	1880.499	31.42	44.21

Mg	Al	Si	K	Ti	Fe	Cl	P	Ca	Na
0.36	2.8	21.08	2.04	0	0.5	0	0	0	0
0.19	2.16	23.6	1.88	0.13	0.49	0	0	0	0
0.35	3.35	25.07	2.87	0.12	0.76	0	0	0	0
0.14	1.26	28.91	1.03	0	0.62	0	0	0	0
0.5	4.11	23.85	2.65	0.19	1.25	0	0	0	0
0.25	1.82	27.61	1.23	0.22	0.41	0	0	0	0
0.36	2.97	28	1.9	0	0.7	0	0	0	0
0.54	4.98	26.82	3.15	0	1.31	0	0	0	0
0.41	4.06	26.37	2.74	0	0.59	0	0	0	0
0.38	3.55	29.13	2.13	0.13	0.82	0	0	0	0
0.36	2	0.45	0	0	0.19	0	0	0	0
0.27	3.18	21.46	3.1	3.17	0.43	0	0	0	0
0.29	2.75	26.19	1.97	0	0.78	0	0	0	0
0.37	2.93	29.47	1.92	0.13	0.64	0	0	0	0
0.29	2.5	22.38	1.77	0.13	0.55	0	0	0	0
0.2	3.41	19.11	3.84	0	0.65	0	0	0	0
0.31	3.03	19.35	1.74	0	0.7	0	0	0	0
0.18	1.44	14.68	1.21	0	0.48	0.1	0	0.23	0.24
0.27	2.76	26.03	2.18	0	0.58	0	0	0	0
0.47	3.32	22.91	2.18	0	1.5	0	0	0	0
0.23	1.4	22.74	0.87	0	0.5	0	0	0	0
0.21	2.2	20.85	1.4	0.12	0.61	0.15	0	0	0
0.42	3.64	18.48	2.26	0.1	0.95	0	0	0	0
0.27	2.51	19.33	1.61	0.23	0.42	0	0	0	0

Table 10. Continued

Sample	Section	Image #	Distance	Surface Area	C	O
Knox	2P	16830	4	683.242	46.2	34.71
Knox	2P	16831	4	626.201	46.69	35.13
Knox	2P	16832	4	778.982	36.3	41.67
Knox	2P	16833	4	316.41	11.46	52.05
Knox	2P	16834	4	311.678	9.27	52.23
Knox	2P	16835	4	667.125	29.95	44.1
Knox	2P	16836	4	836.813	33.7	42.39
Knox	2P	16837	4	2022.569	42.35	38.74
Knox	2P	16838	8	1131.254	39.46	39.85
Knox	2P	16839	8	1086.6	33.33	42.58
Knox	2P	16840	8	449.671	25.98	46.68
Knox	2P	16841	8	372.327	14.22	50.34
Knox	2P	16842	8	315.042	28.09	45.39
Knox	2P	16843	8	1432.737	35.95	41.67
Knox	2P	16844	8	585.318	8.29	52.45
Knox	2P	16845	8	1171.795	41.43	37.01
Knox	2P	14142	12	1703.44	48.69	36.12
Knox	2P	14145	12	1310.244	42.59	39.61
Knox	2P	14148	12	1170.924	17.95	49.78
Knox	2P	14151	12	435.302	19.06	48.28
Knox	2P	14154	12	764.766	25.01	45.9
Knox	2P	14158	12	12422.016	47.82	38.39
Knox	2P	14162	12	13286.194	16.21	49.06

Mg	Al	Si	K	Ti	Fe	Cl	P	Ca	Na
0	.9	13.64	0.97	0.22	0.23	0	1.08	2.05	0
.12	.3	16.69	0.23	0	0.74	0.1	0	0	0
.26	2.28	16.76	1.52	0.65	0.57	0	0	0	0
.38	3.59	29.19	2.31	0.27	0.75	0	0	0	0
.58	4.73	28.33	3.11	0.35	1.4	0	0	0	0
.27	2.49	20.75	1.74	0	0.69	0	0	0	0
.26	1.81	19.8	1.5	0.17	0.38	0	0	0	0
.12	2.02	14.76	1.39	0.29	0.33	0	0	0	0
.22	1.76	16.74	1.22	0.21	0.54	0	0	0	0
.18	1.41	21.06	1.14	0	0.3	0	0	0	0
.18	1.83	23.23	1.35	0.19	0.57	0	0	0	0
.43	3.14	29.23	2.11	0	0.52	0	0	0	0
.18	2.01	21.51	1.74	0.18	0.41	0	0	0.46	0
.18	1.4	19.1	0.95	0.17	0.58	0	0	0	0
.57	4.74	28.85	3.18	1.92	0	0	0	0	0
0	1.93	10.65	1.69	0.27	0.47	0	0	0	0
.19	.35	16.17	0.31	0.21	0.27	0	0	0.35	0
0.13	3.07	25.16	2.3	0.3	0.81	0	0	0.23	0
0.39	3.44	24.28	3.25	0.32	0.39	0	0.4	0.29	0
0.3	5.01	18.73	3.61	0.27	0.89	0	0	0.16	0
0.42	0.94	11.39	0.54	0	0.38	0	0	0.21	.12
0.19	5.45	22.31	3.51	0	2.43	0	0.12	0	0
0.92	0.72	12.47	0.67	0	0.25	0	0	0.5	0

Table 10. Continued

Sample	Section	Image #	Distance	Surface Area	C	O
Knox	3P	17028	4	4351.618	34.78	41.72
Knox	3P	17029	4	2137	23.82	47.1
Knox	3P	17030	4	307.008	13.6	50.67
Knox	3P	17031	4	712.403	15.49	50.69
Knox	3P	17032	4	1647.84	14.97	50.61
Knox	3P	17033	4	5463.175	30.14	44.59
Knox	3P	17034	4	1764.987	14.45	50.87
Knox	3P	17035	4	1432.457	43.92	37.74
Knox	3P	17036	4	1376.697	19.59	48.92
Knox	3P	17037	8	152.44	9.58	52.05
Knox	3P	17038	8	155.839	11.25	51.92
Knox	3P	17039	8	1183.323	21.59	48.53
Knox	3P	17040	8	406.853	11.58	51.81
Knox	3P	17041	8	339.808	10.16	51.89
Knox	3P	17042	8	547.217	13.19	51.05
Knox	3P	17043	8	749.024	43.12	37.46
Knox	3P	17044	12	651.374	26.45	44.86
Knox	3P	17047	12	1098.844	19.61	49.73
Knox	3P	17050	12	3969.086	15.84	50.14
Knox	3P	17053	12	1470.555	33.6	42.44
Knox	3P	17056	12	6033.271	12.09	50.68
Knox	3P	17059	12	1709.753	31.75	42.9
Knox	3P	17062	12	4892.368	42.64	41.01
Knox	3P	17065	12	3579.738	42.56	40.11

Mg	Al	Si	K	Ti	Fe	P	Cl	Ca	Na
0.15	1.14	13.76	0.79	6.66	1	0	0	0	0
0.43	3.97	21.66	2.4	0	0.62	0	0	0	0
0.35	3.36	28.99	2.02	0	0.8	0.21	0	0	0
0.47	4.36	25.11	2.72	0.25	0.92	0	0	0	0
0.47	4.32	25.58	2.91	0.25	0.89	0	0	0	0
0.31	2.63	19.65	2.01	0.16	0.51	0	0	0	0
0.52	4.56	25.45	2.9	0.13	1.11	0	0	0	0
0	0.47	17.13	0.49	0	0.16	0	0.09	0	0
0.34	3.64	24.46	2.4	0	0.66	0	0	0	0
0.49	4.25	29.51	2.81	0	1.32	0	0	0	0
0.49	4.52	27.38	3.01	0.24	1.19	0	0	0	0
0.19	1.96	25.28	1.57	0.24	0.63	0	0	0	0
0.48	4.09	28.21	2.73	0.18	0.93	0	0	0	0
0.53	4.33	29.45	2.81	0	0.82	0	0	0	0
0.49	4.08	27.68	2.62	0.21	0.68	0	0	0	0
0	0.26	18.66	0.26	0	0.14	0	0.09	0	0
0.21	3.55	21.89	1.84	0.7	0.29	0	0	0	0.21
0.2	1.3	26.87	0.91	0.19	0.51	0	0.29	0.14	0.25
0.54	4.63	24.37	3.27	0	1.21	0	0	0	0
0.2	1.64	19.69	1.11	0.32	0.58	0	0.21	0	0.19
0.42	4.42	23.05	3.44	0.36	0.62	1.75	0.14	2.75	0.28
0.29	2.66	19.36	1.88	0.37	0.65	0	0	0	0.16
0.16	1.57	13.08	1.12	0.19	0.23	0	0	0	0
0.2	1.52	14.17	1.01	0	0.32	0	0	0	0.1

Table 10. Continued

Sample	Section	Image #	Distance	Surface Area	C
Vermillion	2P	17275	4	5329.166	49.49
Vermillion	2P	17276	4	8412.012	48.31
Vermillion	2P	17277	4	10794.749	54.29
Vermillion	2P	17278	4	6916.568	52.53
Vermillion	2P	17279	4	11042.4	56.14
Vermillion	2P	17280	4	43184.621	58.84
Vermillion	2P	17281	4	11732.275	51.89
Vermillion	2P	17282	4	13382.252	49.85
Vermillion	2P	17283	8	20206.322	55.42
Vermillion	2P	17284	8	4399.458	40.85
Vermillion	2P	17285	8	14694.813	57.86
Vermillion	2P	17286	8	44955.055	54.94
Vermillion	2P	17287	8	8090.502	49.67
Vermillion	2P	17288	8	4583.438	45.26
Vermillion	2P	17289	8	23526.174	55.69
Vermillion	2P	17290	8	12326.883	50.27
Vermillion	2P	17291	12	11669.506	53.88
Vermillion	2P	17294	12	27020.45	50.22
Vermillion	2P	17297	12	13033.296	45.61
Vermillion	2P	17300	12	22015.564	41.2
Vermillion	2P	17303	12	7511.012	50.45
Vermillion	2P	17306	12	8065.51	48.15
Vermillion	2P	17309	12	11758.827	52.57
Vermillion	2P	17312	12	3960.86	47.69

O	Na	Mg	Al	Si	S	Cl	K	Ca	Fe
37.11	0	0	0.23	12.78	0	0	0.07	0.1	0.22
36.75	0.12	0	0.18	14.03	0	0.23	0.09	0.1	0.2
35.17	0	0	0.16	10.09	0	0	0.07	0.09	0.12
36.33	0	0.08	0	11.07	0	0	0	0	0
34.4	0	0	0.1	9.28	0	0	0	0.13	0.2
32.53	0	0	0.27	8.06	0	0	0.13	0.1	0.2
37	0	0	0.16	10.96	0	0.07	0.09	0	0.13
37.25	0	0	0	12.77	0	0	0	0	0.13
34.74	0	0	0.12	9.61	0	0.11	0	0	0
38.38	1.76	0.41	0.33	16.88	0	0	0.43	0.96	0
33.81	0	0	0	8.33	0	0	0	0	0
35.77	0	0	0.17	9.12	0	0	0	0	0
37.75	0.12	0	0	12.33	0	0	0	0	0.13
38.67	0	0	0.15	15.59	0	0	0.06	0.08	0.18
34.64	0	0	0.34	9.14	0	0	0.09	0	0.1
37.22	0	0	0.3	12.08	0	0	0	0	0.13
35.21	0.1	0	0.34	10.25	0	0.12	0	0	0.12
34.24	1.22	0.32	0.37	11.19	0.76	0.08	0.18	0.61	0.81
39.81	0.94	0.22	0.13	12.24	0	0.13	0.19	0.73	0
38.78	2.18	0.49	0.23	15.72	0	0.17	0.29	0.95	0
35.4	0.12	0	0.84	12.36	0	0.33	0.5	0.08	0
37.43	0.63	0.15	0.33	12.49	0	0.17	0.22	0.29	0.14
35.46	0.47	0.13	0.19	10.87	0	0	0.07	0.23	0
38.69	0.15	0	0.27	12.43	0	0.2	0.18	0.24	0.14

Table 10. Continued

Sample	Section	Image #	Distance	Surface Area	C	O	Na	Mg	Al	Si	S	Cl	K	Ca	Fe
Vermillion	3P	14672	4	4248.297	50.21	34.96	0	0	0.24	14.06	0	0.24	0.07	0.1	0.12
Vermillion	3P	14673	4	6904.659	44.24	38.57	0	0	1.06	14.57	0	0.41	0.33	0.21	0
Vermillion	3P	14674	4	6916.674	43.1	38.13	0.25	0	1.59	16.1	0.09	0.42	0.16	0.16	0
Vermillion	3P	14675	4	6465.044	47.18	36.13	0.1	0	1.87	13.81	0.11	0.37	0.08	0.19	0
Vermillion	3P	14676	4	4011.547	43.5	37.92	0	0.12	0.48	17.24	0	0.17	0.11	0.13	0
Vermillion	3P	17024	4	21145.195	0	56.59	0.35	0	1	39.11	0.23	1.45	0.28	0.54	0
Vermillion	3P	17025	4	4868.56	49.44	37.59	0	0	0.49	11.81	0.07	0.33	0.09	0.18	0
Vermillion	3P	17026	4	9815.378	50.7	35.46	0.18	0.09	1.34	11.32	0.08	0.34	0.11	0.17	0.22
Vermillion	3P	17027	4	9485.49	50.75	35.11	0	0	1.33	11.72	0.13	0.43	0.14	0.21	0
Vermillion	3P	14677	8	12880.508	39.24	39.51	0.12	0	4.8	15.05	0.23	0.33	0.15	0.26	0
Vermillion	3P	14678	8	29887.03	0	55.67	0	0	1.62	39.67	0.36	1.38	0	0.49	0.81
Vermillion	3P	14679	8	2129.454	42.43	38.47	0	0.22	0.88	16.74	0.16	0.08	0.16	0.28	0
Vermillion	3P	14680	8	6618.702	42.57	38.26	0.11	0	1.61	16.44	0.08	0.36	0.13	0.16	0
Vermillion	3P	14681	8	3114.975	42.91	38.42	0	0	0.31	17.69	0	0.19	0.1	0.11	0.27
Vermillion	3P	14682	8	3787.756	43.8	38.46	0	0	0.12	17.28	0	0.18	0	0	0.16
Vermillion	3P	14683	8	4575.558	43.96	37.95	0.1	0.09	0.22	16.89	0.11	0.2	0.07	0.18	0.23
Vermillion	3P	14684	8	2118.778	33.28	43.11	0	0	0.19	23.42	0	0	0	0	0
Vermillion	3P	14568	12	10545.749	47.54	36.31	0.2	0	1.68	13.38	0.08	0.25	0.21	0.18	0.17
Vermillion	3P	14571	12	2108.421	38.55	40.14	0.27	0.18	2.34	17.15	0.1	0.16	0.58	0.26	0.27
Vermillion	3P	14574	12	10449.591	35.44	42.72	0.17	0	3.82	19.36	0	0.1	0	0.17	0.51
Vermillion	3P	14577	12	32160.993	42.16	38.97	0	0	1.53	13.87	0.29	0.28	0	0.3	0.33
Vermillion	3P	14580	12	22512.619	41.76	38.65	0	0	4.64	13.42	0.38	0.38	0	0.42	0.35
Vermillion	3P	14583	12	13059.854	49.3	36.11	0.1	0.1	0.37	13.48	0	0.31	0	0.07	0
Vermillion	3P	14586	12	32160.993	48.08	35.86	0	0	1.05	14.36	0	0.38	0.27	0	0
Vermillion	3P	14589	12	22512.619	47.99	36.42	0.35	0.12	0.23	14.08	0.14	0.23	0	0.3	0.13

Table 11. EDX Bulk Analysis

Sample	Section	Image #	Distance
Vermillion 5806	1P	13975	0
Vermillion 5806	1P	13976	2
Vermillion 5806	1P	13977	2
Vermillion 5806	1P	13978	2
Vermillion 5806	1P	13979	2
Vermillion 5806	1P	13996	6.5
Vermillion 5806	1P	13997	6.5
Vermillion 5806	1P	13998	6.5
Vermillion 5806	1P	13999	6.5
Vermillion 5806	1P	14000	6.5
Vermillion 5806	1P	14001	6.5
Vermillion 5806	1P	14002	6.5
Vermillion 5806	1P	14003	6.5
Vermillion 5806	1P	13984	10.5
Vermillion 5807	1P	13985	10.5
Vermillion 5808	1P	13986	10.5
Vermillion 5806	1P	13987	10.5
Vermillion 5806	1P	13992	10.5
Vermillion 5806	1P	13993	10.5
Vermillion 5806	1P	13994	10.5
Vermillion 5806	1P	13995	10.5
Vermillion 5806	1P	13988	12.5
Vermillion 5806	1P	13989	12.5
Vermillion 5806	1P	13990	12.5
Vermillion 5806	1P	13991	12.5
Vermillion 5806	1P	13980	12.5
Vermillion 5806	1P	13981	12.5

C	O	Al	Si	K	Ti	Ca	Br
12.62	53.29	0	34.09	0	0	0	0
21.82	49.74	0.45	27.57	0.31	0	0.11	0
19.94	50.72	0.25	28.95	0.15	0	0	0
18.28	51.11	0.47	29.74	0.41	0	0	0
19.34	50.74	0.31	29.23	0.38	0	0	0
14.74	52.88	0	32.38	0	0	0	0
6.33	55.41	0	38.25	0	0	0	0
11.71	53.58	0	34.71	0	0	0	0
15.89	52.69	0	31.42	0	0	0	0
17.34	51.76	0.17	30.72	0	0	0	0
16.45	51.89	0.39	31.27	0	0	0	0
9.63	54.41	0	35.97	0	0	0	0
16.4	51.68	0.48	30.87	0.56	0	0	0
18.91	51.69	0	29.4	0	0	0	0
19.27	51.43	0.2	28.96	0	0.15	0	0
16.19	52.42	0.41	30.27	0.49	0.21	0	0
17.53	51.63	0.57	29.72	0.55	0	0	0
12.9	53.06	0.13	33.9	0	0	0	0
15.32	52.16	0.52	31.38	0.61	0	0	0
9.82	54.2	0.15	35.66	0.18	0	0	0
20.31	50.71	0	28.98	0	0	0	0
22.47	49.75	0	27.61	0.17	0	0	0
11.52	53.78	0	34.7	0	0	0	0
12.33	53.44	0	34.23	0	0	0	0
19.26	51.32	0	29.24	0.19	0	0	0
22.04	49.31	1.19	27.46	0	0	0	0
18.01	51.33	0.12	30.54	0	0	0	0

Table 11. Continued

Sample	Section	Image #	Distance
Vermillion 5806	2P	13790	0
Vermillion 5806	2P	13791	2
Vermillion 5806	2P	13792	2
Vermillion 5806	2P	13793	2
Vermillion 5806	2P	13794	2
Vermillion 5806	2P	13815	6.5
Vermillion 5806	2P	13816	6.5
Vermillion 5806	2P	13817	6.5
Vermillion 5806	2P	13818	6.5
Vermillion 5806	2P	13819	6.5
Vermillion 5806	2P	13820	6.5
Vermillion 5806	2P	13821	6.5
Vermillion 5806	2P	13822	6.5
Vermillion 5806	2P	13803	10.5
Vermillion 5807	2P	13804	10.5
Vermillion 5808	2P	13805	10.5
Vermillion 5806	2P	13806	10.5
Vermillion 5806	2P	13811	10.5
Vermillion 5806	2P	13812	10.5
Vermillion 5806	2P	13813	10.5
Vermillion 5806	2P	13814	10.5
Vermillion 5806	2P	13807	12.5
Vermillion 5806	2P	13808	12.5
Vermillion 5806	2P	13809	12.5
Vermillion 5806	2P	13810	12.5
Vermillion 5806	2P	13798	12.5
Vermillion 5806	2P	13799	12.5
Vermillion 5806	2P	13801	12.5
Vermillion 5806	2P	13802	12.5

C	O	Na	Al	Si	K	Ca	Br
20.95	50.54	0	0	28.16	0.35	0	0
19.98	51.05	0	0.34	28.34	0.29	0	0
17.71	51.76	0	0.16	30.2	0.16	0	0
20.08	50.92	0	0.33	28.34	0.33	0	0
25.48	48.36	0	0.36	25.36	0.46	0	0
20.12	50.59	0	0	28.74	0.13	0	0.42
21.74	50.23	0	0	27.43	0.18	0	0.41
24.78	48.72	0	0	25.62	0.21	0	0.68
20.76	50.58	0	0	28.34	0	0	0.31
14.01	53.3	0	0	32.69	0	0	0
19.57	50.77	0	0	29.25	0	0	0.41
20.65	50.29	0	0	27.79	0.42	0	0.85
20.54	50.8	0	0	28.1	0.19	0	0.37
16.82	52.17	0	0	31.01	0	0	0
18.25	51.48	0	0.18	29.92	0.17	0	0
19.64	51.15	0	0	29.21	0	0	0
15.26	52.62	0	0.25	31.65	0.23	0	0
26.69	48.63	0	0	24.69	0	0	0
20.71	50.51	0	0.16	28.62	0	0	0
25.15	48.54	0.19	0.37	25.24	0.5	0	0
18.74	51.6	0	0	29.67	0	0	0
21.81	50.57	0	0.17	27.31	0.14	0	0
21.82	50.08	0.21	0	27.77	0.12	0	0
26.39	48.31	0.22	0.19	24.5	0.25	0.13	0
20.33	50.74	0	0.41	28.17	0.36	0	0
21.79	49.42	0	1.25	27.17	0.36	0	0
18.53	51.09	0	0	30.39	0	0	0
16.99	51.97	0.27	0.27	30.24	0.27	0	0
21.28	50.25	0	0.21	28.06	0.2	0	0

Table 11.Continued

Sample	Section	Image #	Distance
Vermillion 5806	3P	14539	0
Vermillion 5806	3P	14540	2
Vermillion 5806	3P	14541	2
Vermillion 5806	3P	14542	2
Vermillion 5806	3P	14543	2
Vermillion 5806	3P	14560	6.5
Vermillion 5806	3P	14561	6.5
Vermillion 5806	3P	14562	6.5
Vermillion 5806	3P	14563	6.5
Vermillion 5806	3P	14564	6.5
Vermillion 5806	3P	14565	6.5
Vermillion 5806	3P	14566	6.5
Vermillion 5806	3P	14567	6.5
Vermillion 5806	3P	14548	10.5
Vermillion 5807	3P	14549	10.5
Vermillion 5808	3P	14550	10.5
Vermillion 5806	3P	14551	10.5
Vermillion 5806	3P	14556	10.5
Vermillion 5806	3P	14557	10.5
Vermillion 5806	3P	14558	10.5
Vermillion 5806	3P	14559	10.5
Vermillion 5806	3P	14544	12.5
Vermillion 5806	3P	14545	12.5
Vermillion 5806	3P	14546	12.5
Vermillion 5806	3P	14547	12.5
Vermillion 5806	3P	14552	12.5
Vermillion 5806	3P	14553	12.5
Vermillion 5806	3P	14554	12.5
Vermillion 5806	3P	14555	12.5

C	O	Al	Si	K	Cl	Ca	Br
19.33	49.59	0.52	30.4		0.16	0	0
18.05	49.7	0	32.25	0	0	0	0
17.7	50.27	0	32.03	0	0	0	0
19.75	49.48	0	30.77	0	0	0	0
18.14	49.9	0.21	31.5	0.25	0	0	0
18.94	49.55	0.19	31.33	0	0	0	0
17.37	50.33	0	32.17	0.12	0	0	0
17.8	50.11	0	32.09	0	0	0	0
18.4	49.86	0.28	31.29	0.17	0	0	0
16.14	50.55	0	33.16	0.15	0	0	0
18.54	49.91	0	31.55	0	0	0	0
16.83	50.36	0	32.81	0	0	0	0
16.1	50.58	0	33.32	0	0	0	0
14.47	51.34	0.19	33.99	0	0	0	0
13.51	51.54	0.21	34.73	0	0	0	0
10.8	52.21	0.22	36.78	0	0	0	0
12.38	52.04	0	35.59	0	0	0	0
17.04	49.96	0	33	0	0	0	0
19.84	49.1	0.21	30.84	0	0	0	0
16.2	50.6	0	32.98	0.22	0	0	0
15.47	50.61	0.14	33.77	0	0	0	0
23.33	47.24	1.34	27.68	0.4	0	0	0
18.07	49.66	0.23	32.04	0	0	0	0
28.69	46	0.16	24.81	0.2	0	0	0
20.3	48.65	0.33	30.2	0.29	0	0	0
18.1	50.07	0.14	31.7	0	0	0	0
26.83	46.75	0.18	26.24	0	0	0	0
24.14	47.78	0	28.08	0	0	0	0
20.22	49.03	0.21	30.39	0.14	0	0	0

Table 11.Continued

Sample	Section	Image #	Distance	C
Knox8642.5	1P	13948	0	25.91
Knox8642.5	1P	13949	2	0
Knox8642.5	1P	13950	2	4.28
Knox8642.5	1P	13951	2	0
Knox8642.5	1P	13952	2	4.7
Knox8642.5	1P	13953	2	4.46
Knox8642.5	1P	13954	2	0
Knox8642.5	1P	13941	6.5	4.91
Knox8642.5	1P	13942	6.5	4.98
Knox8642.5	1P	13943	6.5	28.98
Knox8642.5	1P	13944	6.5	4.49
Knox8642.5	1P	13945	6.5	3.68
Knox8642.5	1P	13946	6.5	3.96
Knox8642.5	1P	13947	6.5	3.81
Knox8642.5	1P	13948	6.5	4.29
Knox8642.5	1P	13932	10.5	4.8
Knox8642.5	1P	13929	10.5	4.58
Knox8642.5	1P	13930	10.5	5.58
Knox8642.5	1P	13931	10.5	5.4
Knox8642.5	1P	13937	10.5	5.33
Knox8642.5	1P	13938	10.5	0
Knox8642.5	1P	13939	10.5	0
Knox8642.5	1P	13940	10.5	3.75
Knox8642.5	1P	13925	12.5	14.17
Knox8642.5	1P	13926	12.5	7.76
Knox8642.5	1P	13927	12.5	14.35
Knox8642.5	1P	13928	12.5	10.19
Knox8642.5	1P	13933	12.5	12.43
Knox8642.5	1P	13934	12.5	10.85
Knox8642.5	1P	13935	12.5	12.28

O	Mg	Al	Si	K	Ti	Fe	Na	Mg	Ca
46	0.58	5.69	15.55	3.91	0.2	2.16	0	0	0
56.72	0	0.73	41.68	0.87	0	0	0	0	0
55.27	0	1.43	37.22	1.81	0	0	0	0	0
56.38	0	1.46	40.39	1.78	0	0	0	0	0
55.46	0	1.12	37.39	1.33	0	0	0	0	0
54.72	0	1.76	36.79	2.28	0	0	0	0	0
56.34	0	1.34	40.53	1.8	0	0	0	0	0
55.65	0	1.47	35.84	1.91	0.21	0	0	0	0
56.15	0	0.85	36.93	1.09	0	0	0	0	0
45.56	0.36	3.54	18.22	2.53	0.19	0.62	0	0	0
56	0	0.94	37.36	1.21	0	0	0	0	0
55.76	0	1.19	37.83	1.54	0	0	0	0	0
55.72	0	0.78	38.49	1.05	0	0	0	0	0
55.32	0	1.41	37.58	1.87	0	0	0	0	0
55.57	0	0.86	38.1	1.19	0	0	0	0	0
55.28	0	1.1	37.46	1.36	0	0	0	0	0
55.36	0	1.52	36.68	1.85	0	0	0	0	0
54.66	0	1.46	36.43	1.87	0	0	0	0	0
55.3	0	0.98	37.03	1.29	0	0	0	0	0
55.16	0	1.01	37.23	1.27	0	0	0	0	0
56.7	0	0.81	41.33	1.16	0	0	0	0	0
56.72	0	0.81	41.47	1	0	0	0	0	0
55.55	0	1.59	37.06	2.04	0	0	0	0	0
52.75	0	0.82	31.26	0.99	0	0	0	0	0
54	0	1.34	35.24	1.66	0	0	0	0	0
52.37	0	1.22	30.71	1.35	0	0	0	0	0
53.25	0	1.25	33.54	1.56	0	0	0.21	0	0
52.99	0	1.08	32.07	1.43	0	0	0	0	0
53.84	0	0.67	33.73	0.91	0	0	0	0	0
53.31	0	0.88	32.55	0.98	0	0	0	0	0

Table 11. Continued

Sample	Section	Image #	Distance	C
Knox8642.5	2P	14113	0	3.14
Knox8642.5	2P	14114	2	4.34
Knox8642.5	2P	14115	2	0
Knox8642.5	2P	14116	2	3.79
Knox8642.5	2P	14117	2	4.89
Knox8642.5	2P	14134	6.5	5.49
Knox8642.5	2P	14135	6.5	3.85
Knox8642.5	2P	14136	6.5	3.13
Knox8642.5	2P	14137	6.5	4.75
Knox8642.5	2P	14138	6.5	0
Knox8642.5	2P	14139	6.5	0
Knox8642.5	2P	14140	6.5	6.38
Knox8642.5	2P	14141	6.5	3.33
Knox8642.5	2P	14122	10.5	5.39
Knox8642.5	2P	14123	10.5	4.91
Knox8642.5	2P	14124	10.5	4.96
Knox8642.5	2P	14125	10.5	7.29
Knox8642.5	2P	14130	10.5	0
Knox8642.5	2P	14131	10.5	4.48
Knox8642.5	2P	14132	10.5	9.64
Knox8642.5	2P	14133	10.5	4.34
Knox8642.5	2P	14118	12.5	9.41
Knox8642.5	2P	14119	12.5	4.9
Knox8642.5	2P	14120	12.5	10.59
Knox8642.5	2P	14121	12.5	11.41
Knox8642.5	2P	14126	12.5	4.13
Knox8642.5	2P	14127	12.5	8.55

O	Na	Al	Si	K	Ti	Fe	Na	Mg	Ca
55.32	0	1.17	38.68	1.69	0	0	0	0	0
54.89	0	1.17	37.85	1.52	0	0.22	0	0	0
56.34	0	0.85	41.41	1.16	0	0.25	0	0	0
55.16	0	1.52	37.41	2.12	0	0	0	0	0
55.16	0	0.61	38.52	0.82	0	0	0	0	0
54.99	0	1.18	36.85	1.48	0	0	0	0	0
55.43	0	1.13	38.25	1.34	0	0	0	0	0
55.74	0	0.76	39.38	0.99	0	0	0	0	0
54.63	0	1.41	37.32	1.89	0	0	0	0	0
56.14	0	1.22	40.93	1.71	0	0	0	0	0
56.31	0	1.31	40.47	1.9	0	0	0	0	0
54.48	0	0.77	37.41	0.97	0	0	0	0	0
55.39	0	1.16	38.67	1.45	0	0	0	0	0
55.71	0	0.69	37.34	0.87	0	0	0	0	0
55.49	0	0.97	37.41	1.22	0	0	0	0	0
55.19	0	1.5	36.26	2.09	0	0	0	0	0
54.34	0	1.61	34.32	2.11	0.34	0	0	0	0
56.32	0	1.55	39.89	2.24	0	0	0	0	0
55.02	0	1.04	37.94	1.52	0	0	0	0	0
53.79	0	1.04	34.22	1.31	0	0	0	0	0
55.2	0.24	0.92	38.3	1.01	0	0	0	0	0
52.78	0	3.01	33.13	1.68	0	0	0	0	0
55.23	0	1.26	37.12	1.5	0	0	0	0	0
53.46	0.31	1.52	32	1.94	0.18	0	0	0	0
52.88	0.18	1.27	32.76	1.51	0	0	0	0	0
55.17	0.27	0.87	38.48	1.07	0	0	0	0	0
54.14	0.23	0.6	35.84	0.64	0	0	0	0	0

Table 11. Continued

Sample	Section	Image #	Distance	C	O	Na	Al	Si	K	Ti	Fe	Na	Mg	Ca
Knox8642.5	3P	13742	0	0	57.18	0	0.76	41.16	0.9	0	0	0	0	0
Knox8642.5	3P	13743	2	0	56.99	0	0.81	41.27	0.93	0	0	0	0	0
Knox8642.5	3P	13744	2	0	56.45	0	1.55	40.04	1.96	0	0	0	0	0
Knox8642.5	3P	13745	2	3.24	55.81	0	1.06	38.6	1.29	0	0	0	0	0
Knox8642.5	3P	13746	2	0	56.89	0	0.56	41.89	0.66	0	0	0	0	0
Knox8642.5	3P	13764	6.5	3.98	55.37	0	1.21	37.89	1.54	0	0	0	0	0
Knox8642.5	3P	13765	6.5	3.91	55.57	0	1.37	37.31	1.84	0	0	0	0	0
Knox8642.5	3P	13766	6.5	0	56.86	0	0.28	42.48	0.38	0	0	0	0	0
Knox8642.5	3P	13767	6.5	4.08	55.68	0	0.73	38.59	0.91	0	0	0	0	0
Knox8642.5	3P	13768	6.5	0	57.75	0	1.25	39.3	1.7	0	0	0	0	0
Knox8642.5	3P	13769	6.5	9.75	54.28	0	1.89	31.18	1.81	0.33	0.37	0	0.21	0.18
Knox8642.5	3P	13770	6.5	0	57.52	0	0.88	40.38	1.22	0	0	0	0	0
Knox8642.5	3P	13771	6.5	0	57.59	0	1.1	39.38	1.51	0.41	0	0	0	0
Knox8642.5	3P	13751-4	10.5	3.5	56.56	0	0.29	39.37	0.28	0	0	0	0	0
Knox8642.5	3P	13752-3	10.5	5.05	55.85	0	1.09	36.25	1.53	0.23	0	0	0	0
Knox8642.5	3P	13753-2	10.5	4	56.07	0	0.74	38.23	0.96	0	0	0	0	0
Knox8642.5	3P	13754-1	10.5	4.96	55.84	0	1.05	36.76	1.38	0	0	0	0	0
Knox8642.5	3P	13760	10.5	0	56.59	0	1.35	40.27	1.8	0	0	0	0	0
Knox8642.5	3P	13761	10.5	0	56.73	0	0.99	40.86	1.41	0	0	0	0	0
Knox8642.5	3P	13762	10.5	0	56.89	0	1.36	39.95	1.8	0	0	0	0	0
Knox8642.5	3P	13763	10.5	3.97	55.67	0	1.08	37.98	1.3	0	0	0	0	0
Knox8642.5	3P	13747-1	12.5	9.5	53.39	0.3	1.7	32.99	2.13	0	0	0	0	0
Knox8642.5	3P	13748-2	12.5	8.33	54	0	0.95	35.46	1.25	0	0	0	0	0
Knox8642.5	3P	13749-3	12.5	9	54.09	0.23	1.02	34.29	1.37	0	0	0	0	0
Knox8642.5	3P	13750-4	12.5	10.04	53.79	0	0.77	34.44	0.96	0	0	0	0	0
Knox8642.5	3P	13755	12.5	8.35	54.69	0.24	1.04	34.25	1.43	0	0	0	0	0
Knox8642.5	3P	13756	12.5	6.32	55.36	0	1.29	35.18	1.62	0.23	0	0	0	0
Knox8642.5	3P	13758	12.5	7.01	54.89	0.3	1.16	35.61	1.03	0	0	0	0	0
Knox8642.5	3P	13759	12.5	5.11	55.25	0	1.09	37.1	1.45	0	0	0	0	0

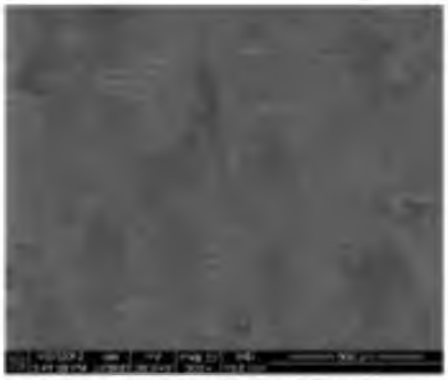

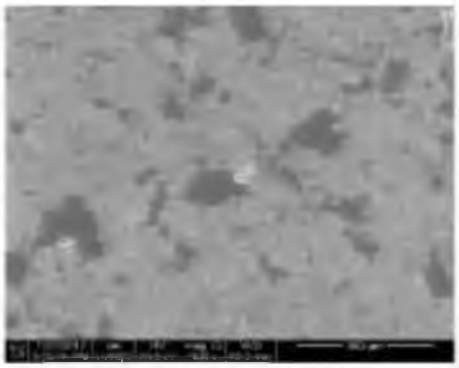

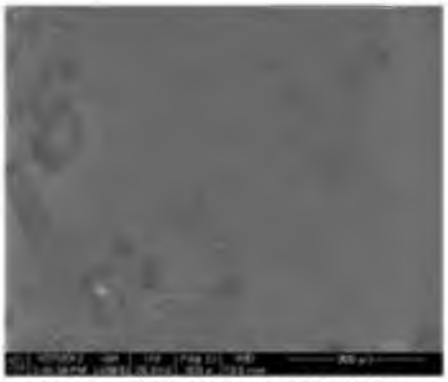

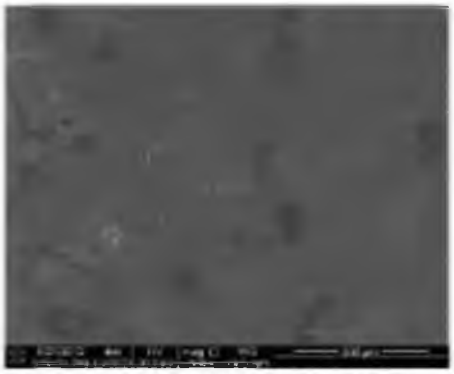

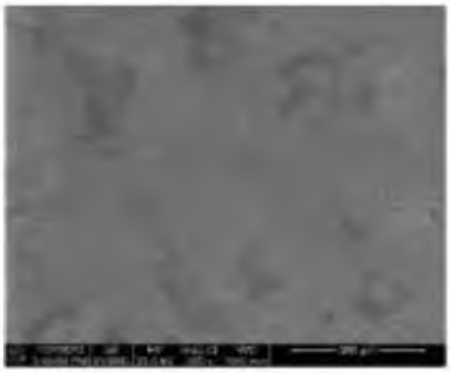

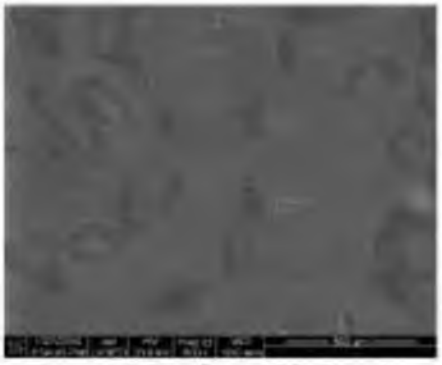

Figure 13. 300x SEM Images

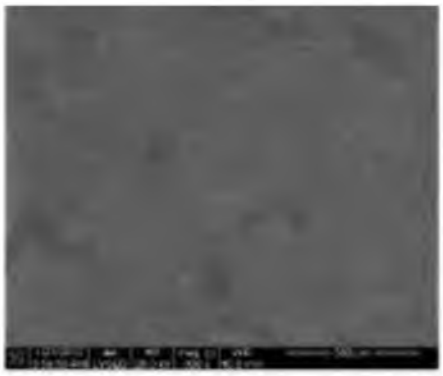

Knox EXP 8642.5-1P 13954

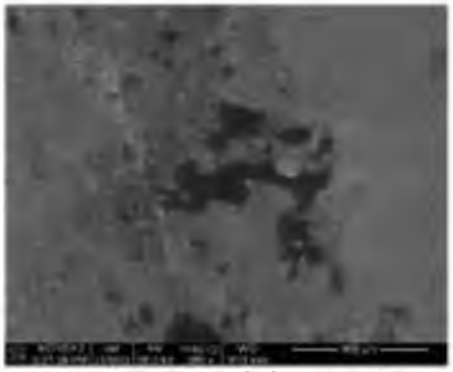

Knox EXP 8642.5-1P 13943

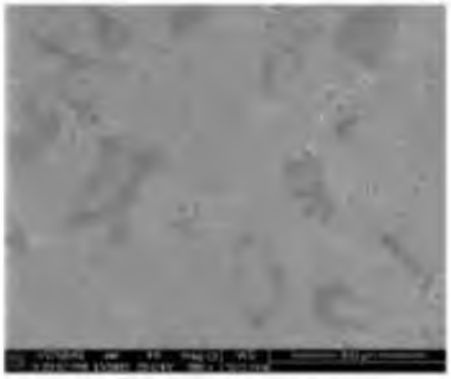

Knox EXP 8642.5-1P 13941

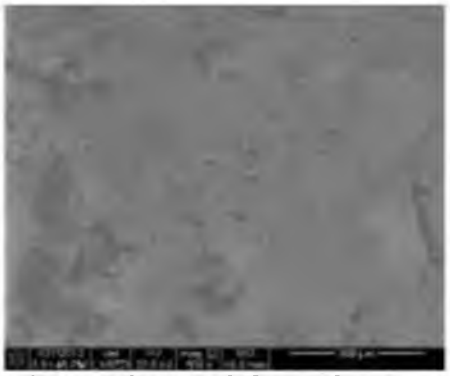

Knox EXP 8642.5-1P 13944

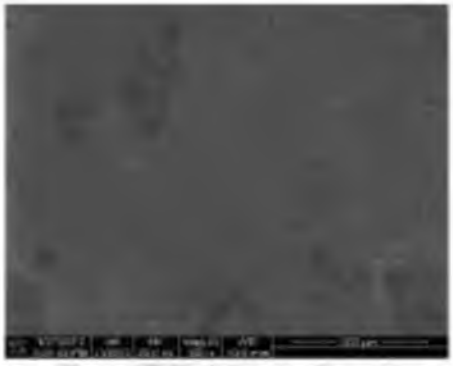

Knox EXP 8642.5-1P 13942

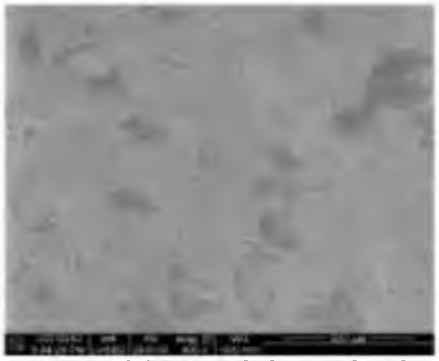

Knox EXP 8642.5-1P 13945

Figure 13. Continued

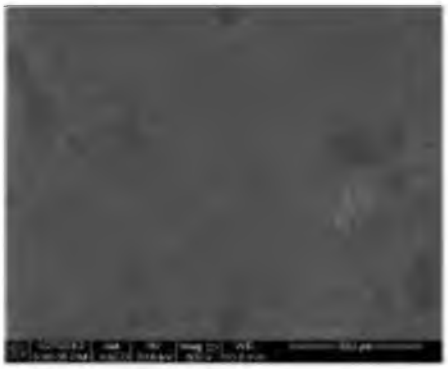

Knox EXP 8642.5-1P 13946

Knox EXP 8642.5-1P 13932

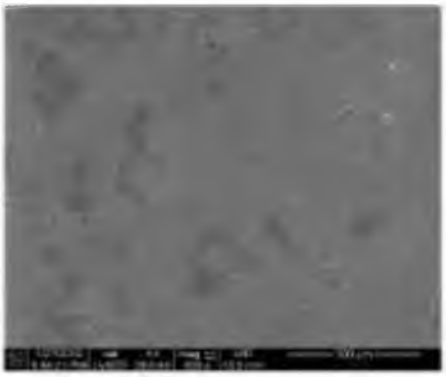

Knox EXP 8642.5-1P 13947

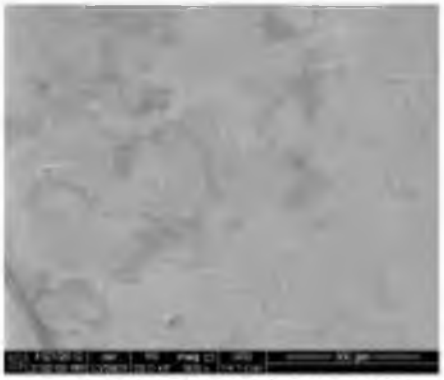

Knox EXP 8642.5-1P 13929

Knox EXP 8642.5-1P 13948

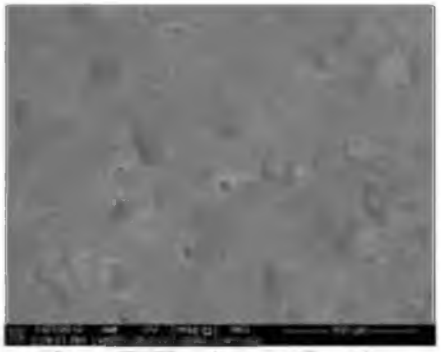

Knox EXP 8642.5-1P 13930

Figure 13. Continued

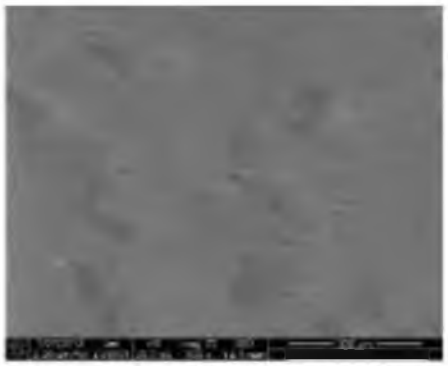

Knox EXP 8642.5-1P 13931

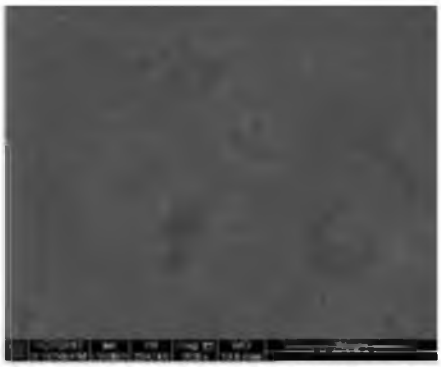

Knox EXP 8642.5-1P 13939

Knox EXP 8642.5-1P 13937

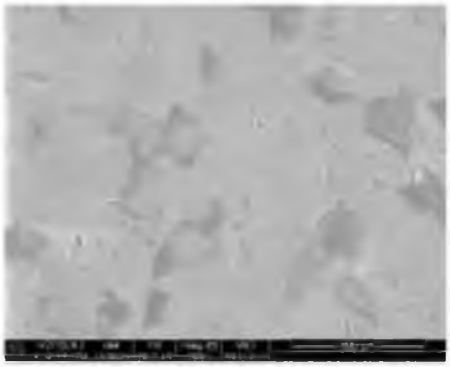

Knox EXP 8642.5-1P 13940

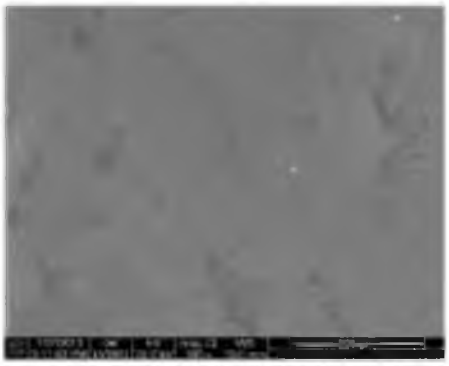

Knox EXP 8642.5-1P 13938

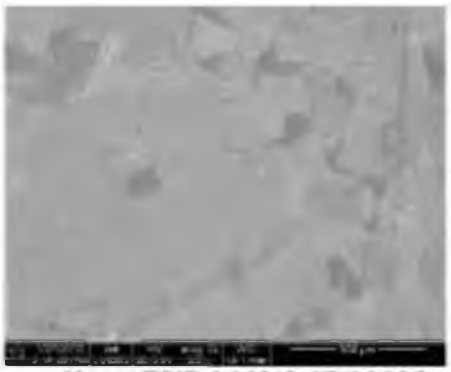

Knox EXP 8642.5-1P 13925

Figure 13. Continued

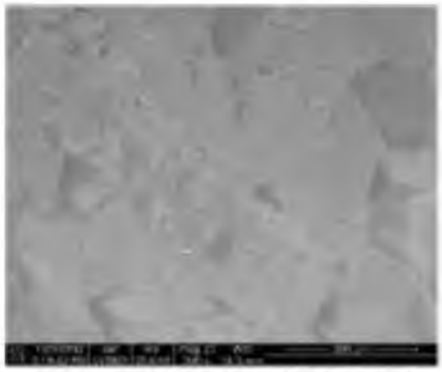

Knox EXP 8642.5-1P 139926

Knox EXP 8642.5-1P 139933

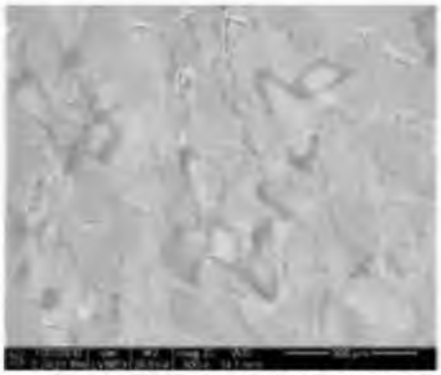

Knox EXP 8642.5-1P 139927

Knox EXP 8642.5-1P 139934

Knox EXP 8642.5-1P 139928

Knox EXP 8642.5-1P 139935

Figure 13. Continued

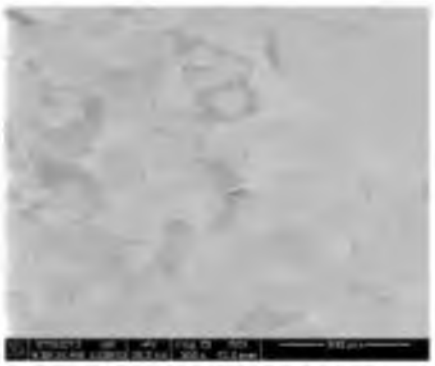
Knox EXP 8642.5-2P 14113

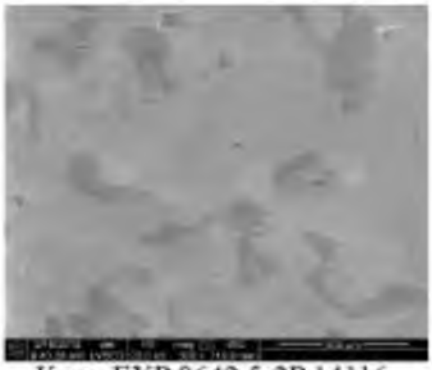
Knox EXP 8642.5-2P 14116

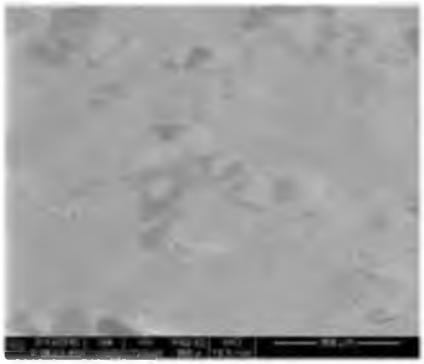
Knox EXP 8642.5-2P 14114


Knox EXP 8642.5-2P 14117

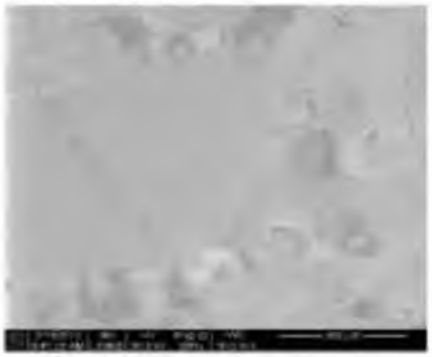
Knox EXP 8642.5-2P 14115

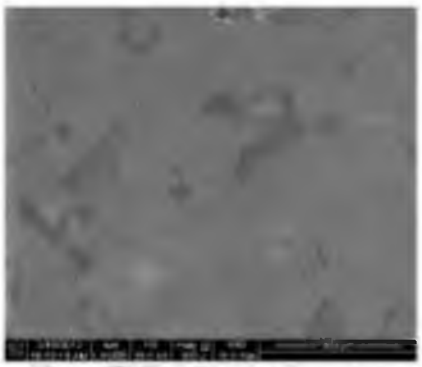
Knox EXP 8642.5-2P 14134

Figure 13. Continued

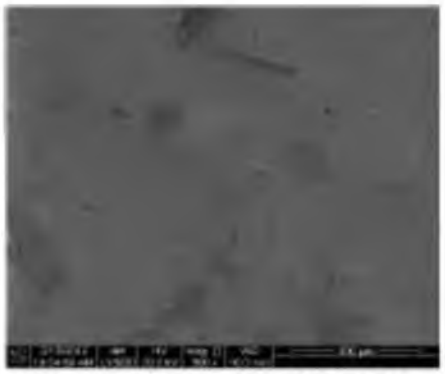

Knox EXP 8642.5-2P 14135

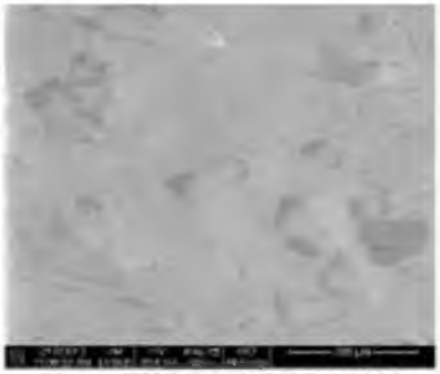

Knox EXP 8642.5-2P 14138

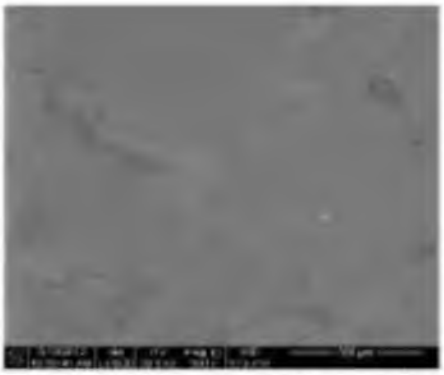

Knox EXP 8642.5-2P 14136

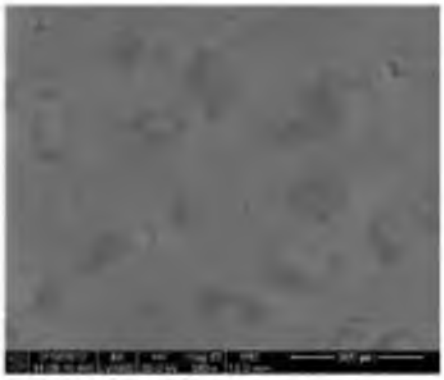

Knox EXP 8642.5-2P 14139

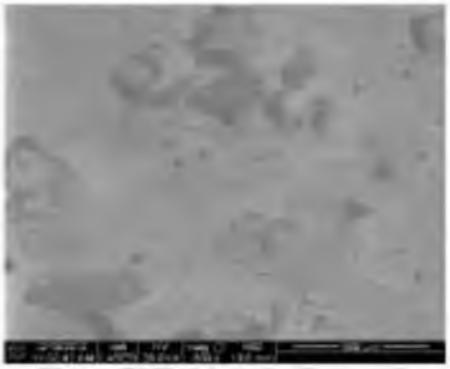

Knox EXP 8642.5-2P 14137

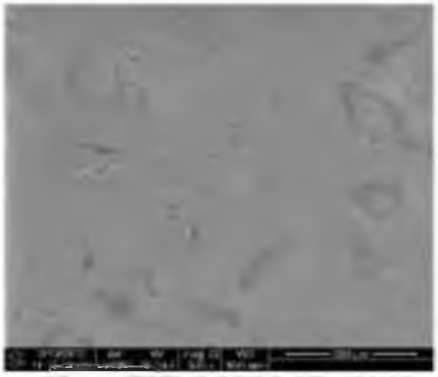

Knox EXP 8642.5-2P 14140

Figure 13. Continued

Knox EXP 8642.5-2P 14141

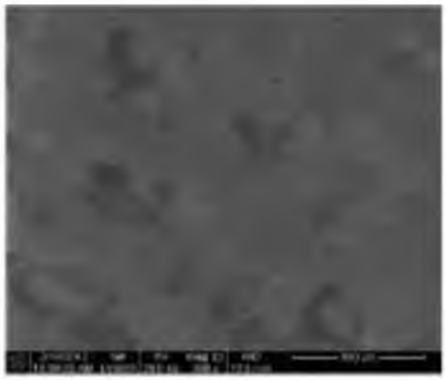

Knox EXP 8642.5-2P 14124

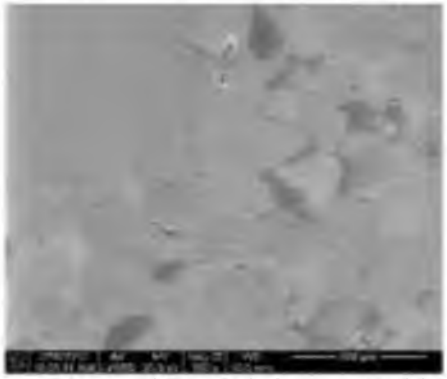

Knox EXP 8642.5-2P 141422

Knox EXP 8642.5-2P 14125

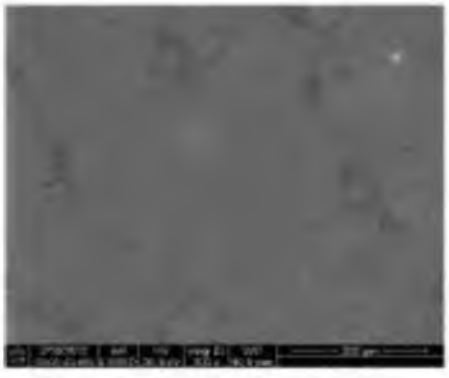

Knox EXP 8642.5-2P 14123

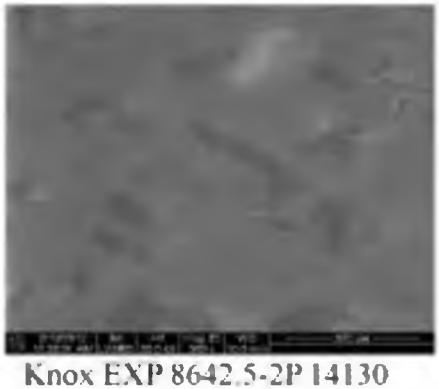

Knox EXP 8642.5-2P 14130

Figure 13. Continued

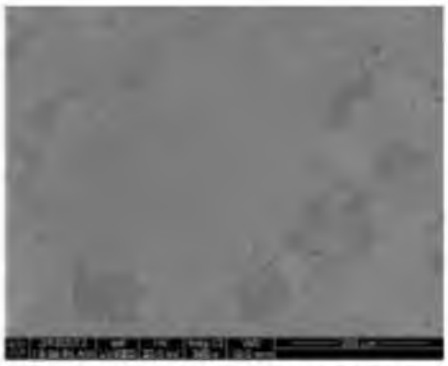

Knox EXP 8642.5-2P 14130

Knox EXP 8642.5-2P 14118

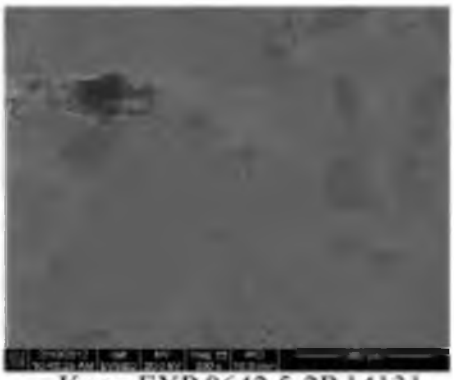

Knox EXP 8642.5-2P 14131

Knox EXP 8642.5-2P 14119

Knox EXP 8642.5-2P 14132

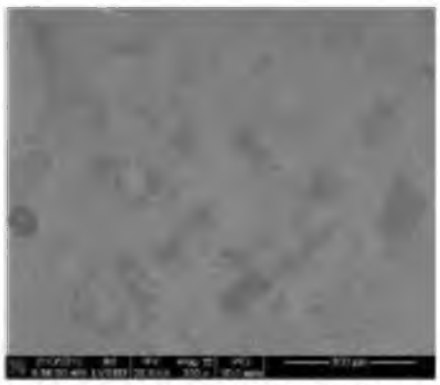

Knox EXP 8642.5-2P 14120

Figure 13. Continued

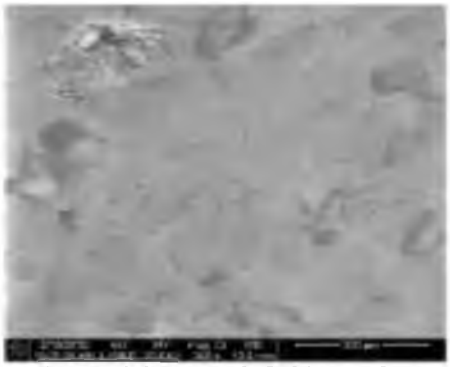

Knox EXP 8642.5-2P 14121

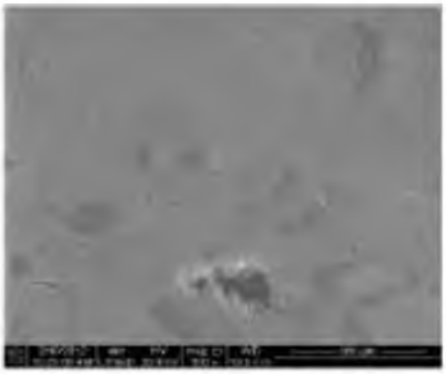

Knox EXP 8642.5-2P 14128

Knox EXP 8642.5-2P 14126

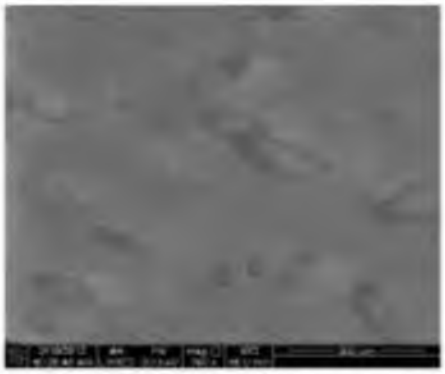

Knox EXP 8642.5-2P 14129

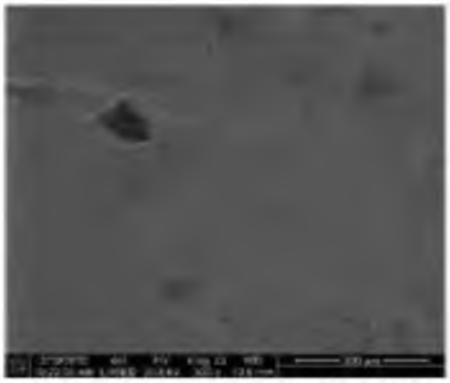

Knox EXP 8642.5-2P 14127

Figure 13. Continued

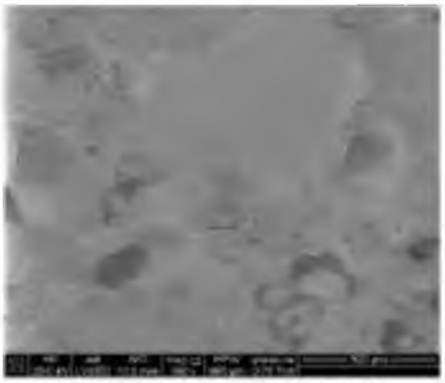

Knox EXP 8642.5-3P 13742

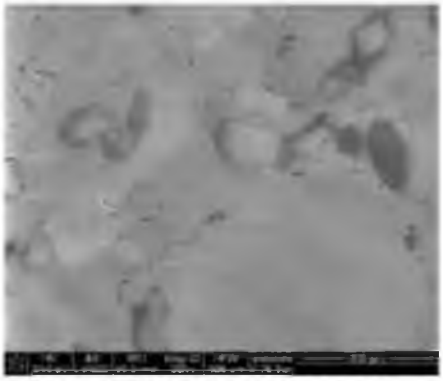

Knox EXP 8642.5-3P 13745

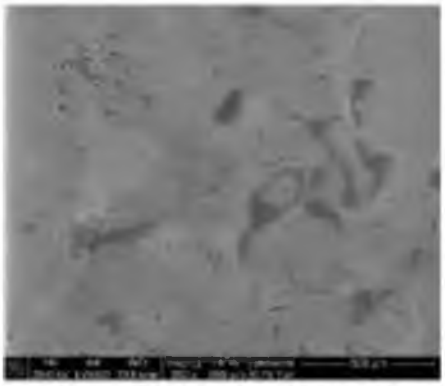

Knox EXP 8642.5-3P 13743

Knox EXP 8642.5-3P 13746

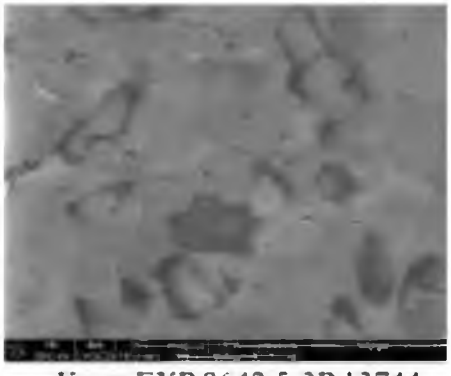

Knox EXP 8642.5-3P 13744

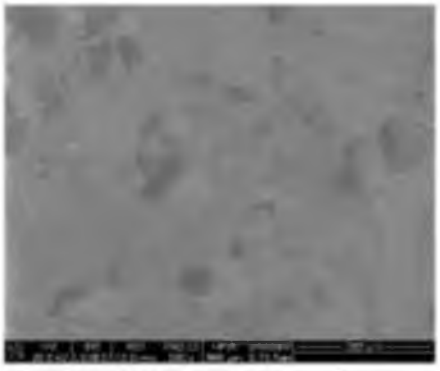

Knox EXP 8642.5-3P 13764

Figure 13. Continued

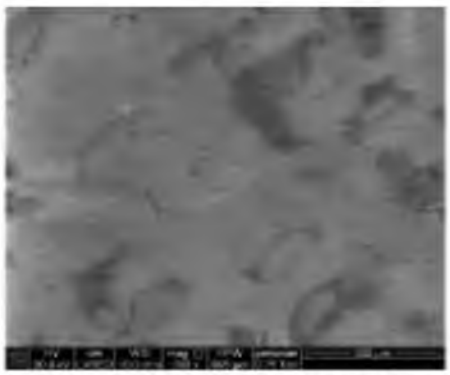

Knox EXP 8642.5-3P 13765

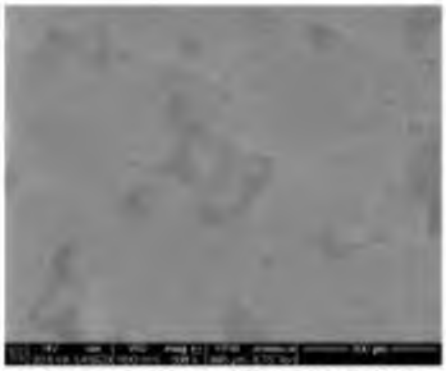

Knox EXP 8642.5-3P 13768

Knox EXP 8642.5-3P 13766

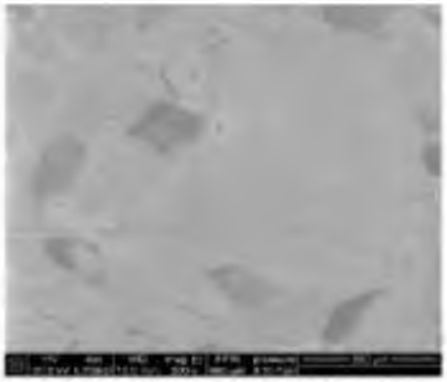

Knox EXP 8642.5-3P 13769

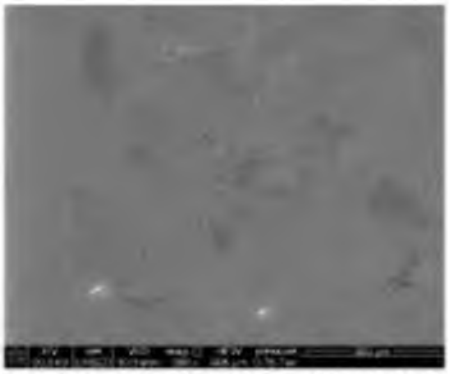

Knox EXP 8642.5-3P 13767

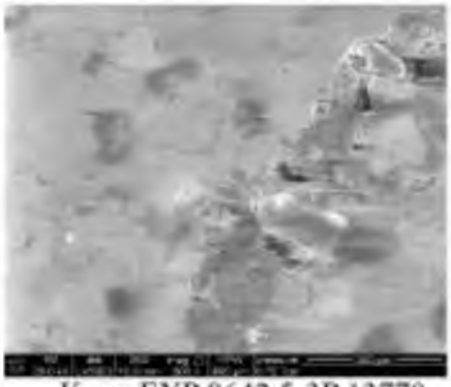

Knox EXP 8642.5-3P 13770

Figure 13. Continued

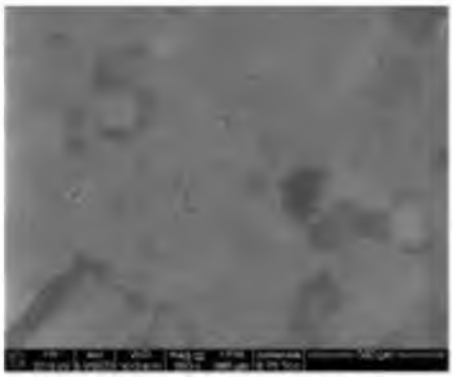

Knox EXP 8642.5-3P 13771

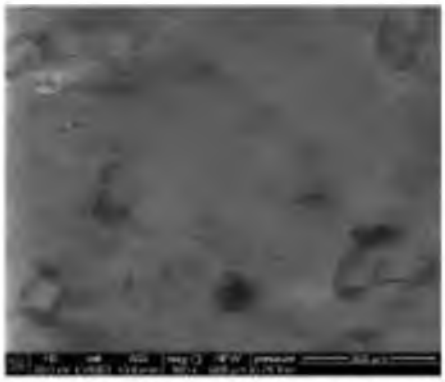

Knox EXP 8642.5-3P 13751-2

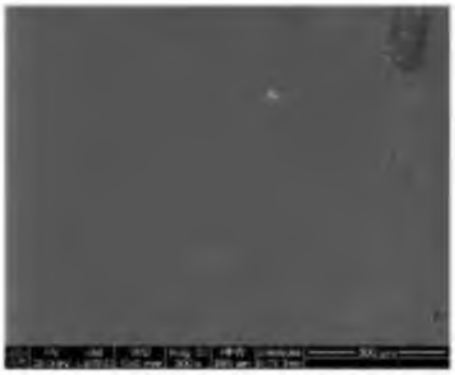

Knox EXP 8642.5-3P 13751-4

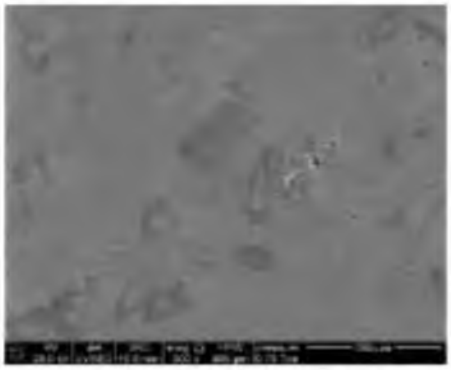

Knox EXP 8642.5-3P 13751-1

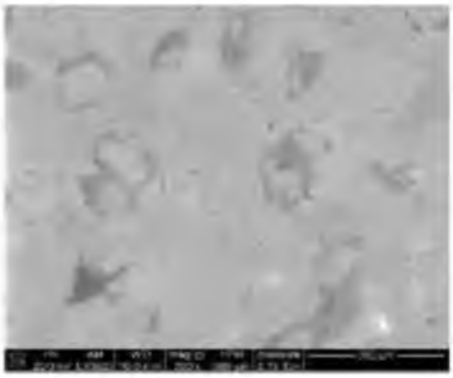

Knox EXP 8642.5-3P 13751-3

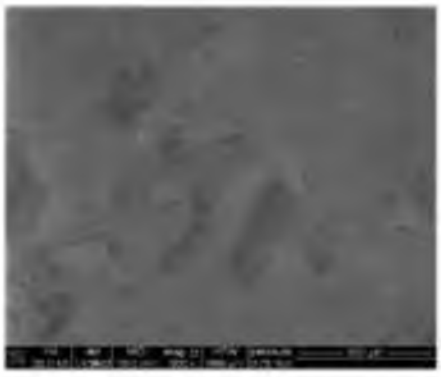

Knox EXP 8642.5-3P 13760

Figure 13. Continued

Knox EXP 8642.5-3P 13761

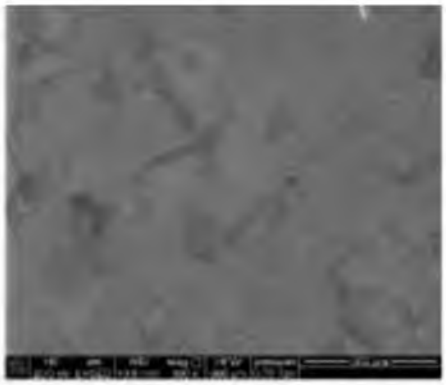

Knox EXP 8642.5-3P 13747

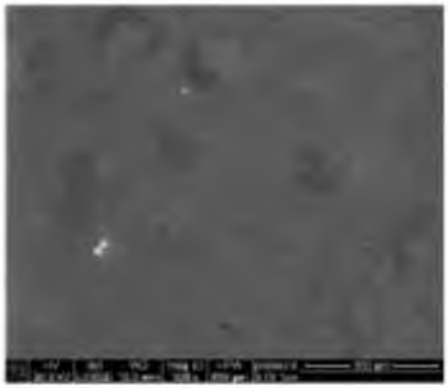

Knox EXP 8642.5-3P 13762

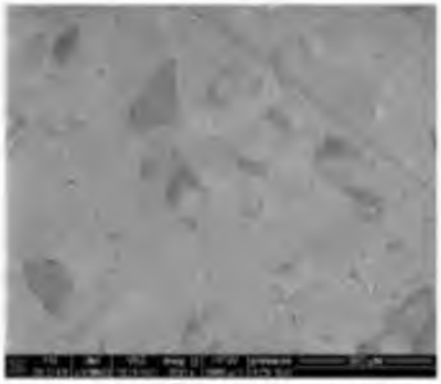

Knox EXP 8642.5-3P 13748

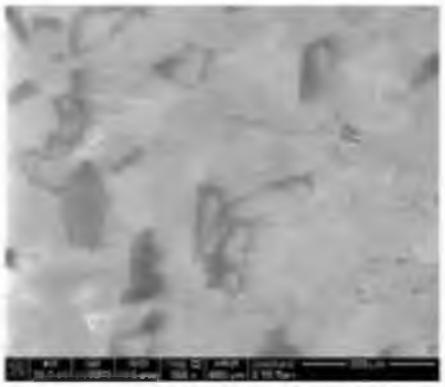

Knox EXP 8642.5-3P 13763

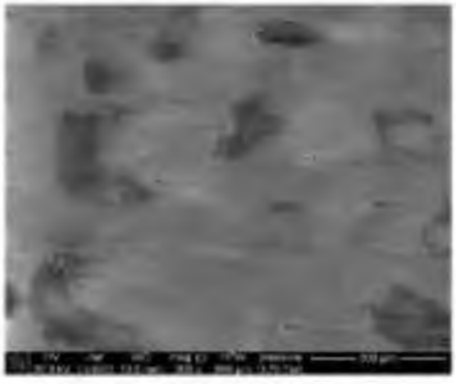

Knox EXP 8642.5-3P 13749

Figure 13. Continued

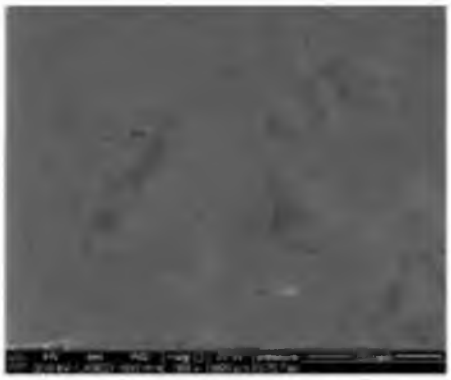

Knox EXP 8642.5-3P 13750

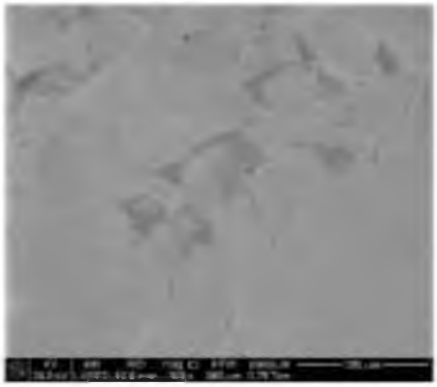

Knox EXP 8642.5-3P 13758

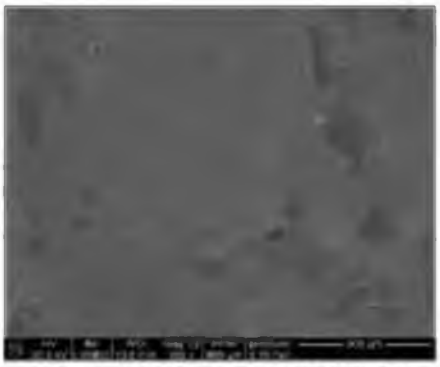

Knox EXP 8642.5-3P 13755

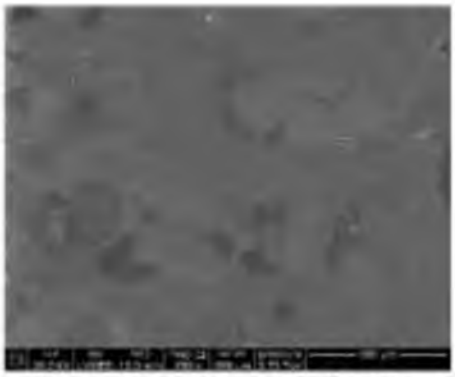

Knox EXP 8642.5-3P 13759

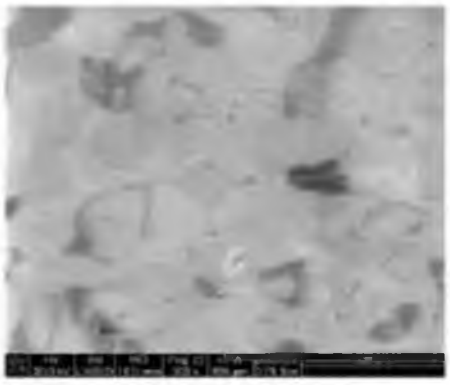

Knox EXP 8642.5-3P 13756

Figure 13. Continued

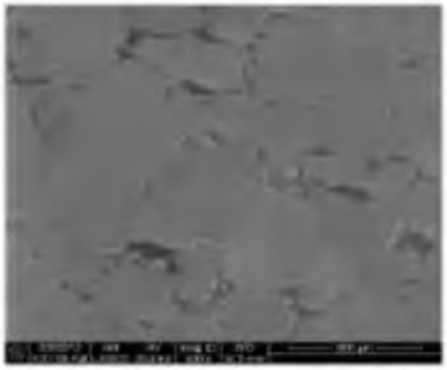

Vermillion EXP 5806-1P 13975

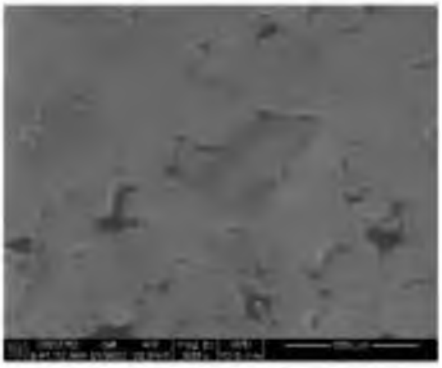

Vermillion EXP 5806-1P 13978

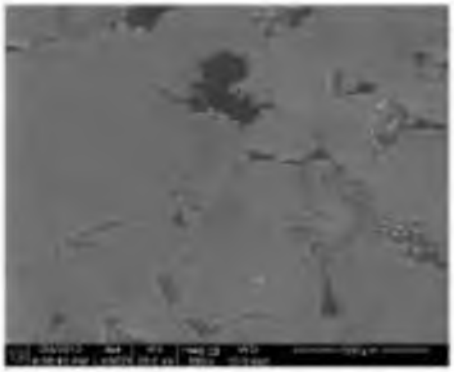

Vermillion EXP 5806-1P 13976

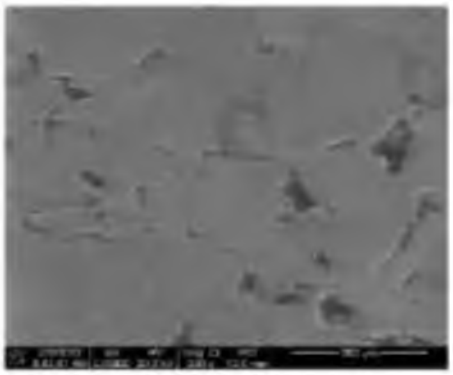

Vermillion EXP 5806-1P 13979

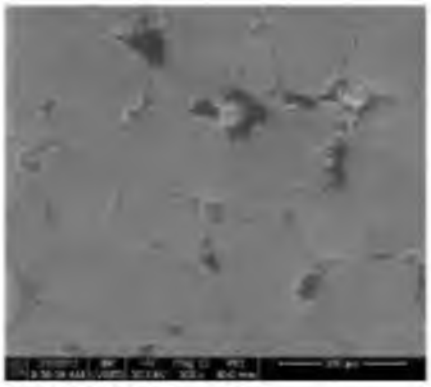

Vermillion EXP 5806-1P 13977

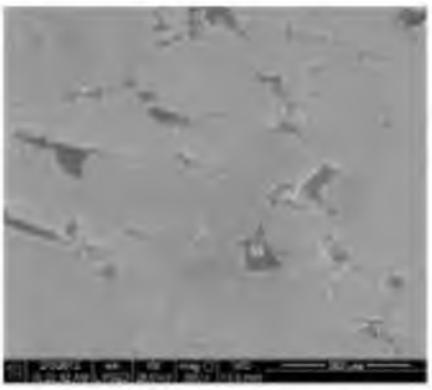

Vermillion EXP 5806-1P 13996

Figure 13. Continued

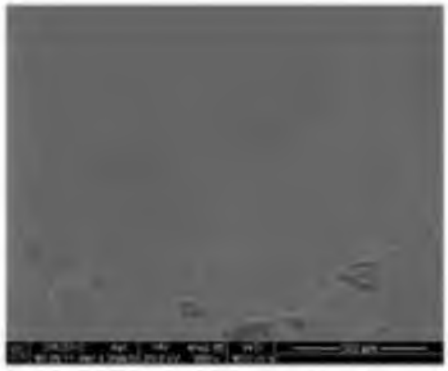

Vermillion EXP 5806-1P 13997

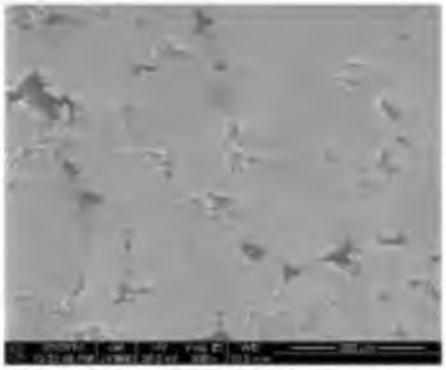

Vermillion EXP 5806-1P 1400

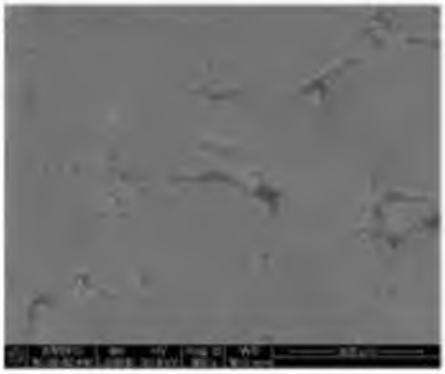

Vermillion EXP 5806-1P 13998

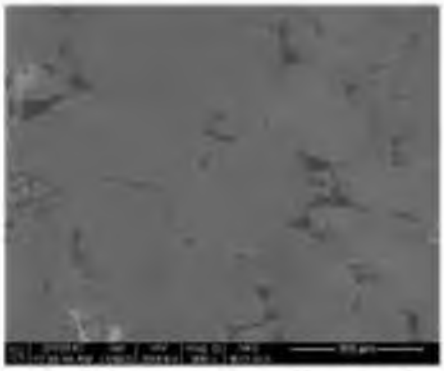

Vermillion EXP 5806-1P 1401

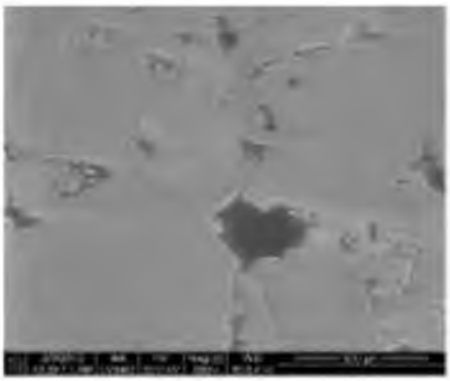

Vermillion EXP 5806-1P 13999

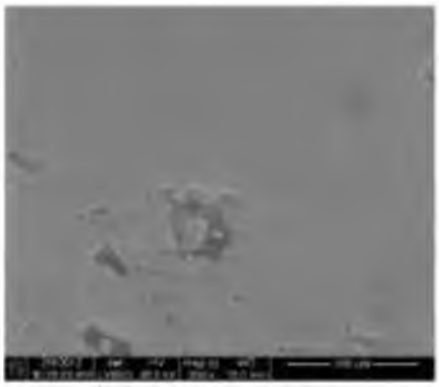

Vermillion EXP 5806-1P 1402

Figure 13. Continued

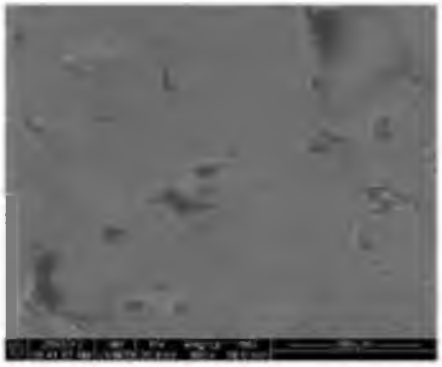

Vermillion EXP 5806-1P 14003

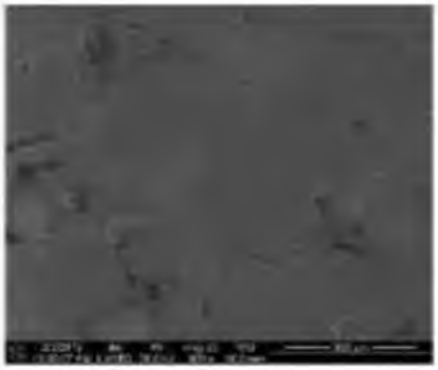

Vermillion EXP 5806-1P 13986

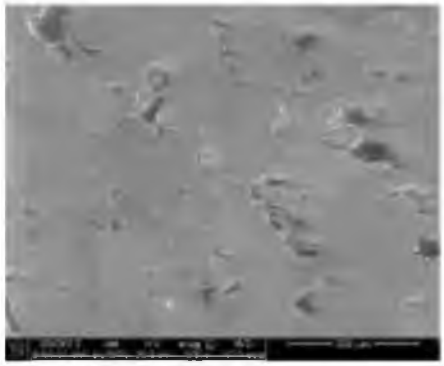

Vermillion EXP 5806-1P 13984

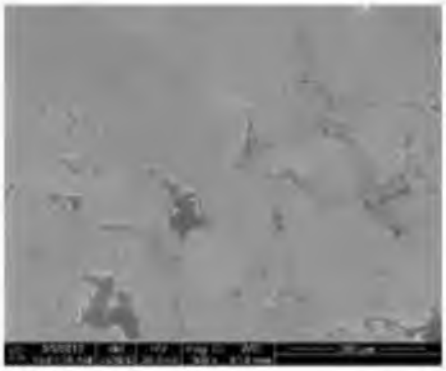

Vermillion EXP 5806-1P 13987

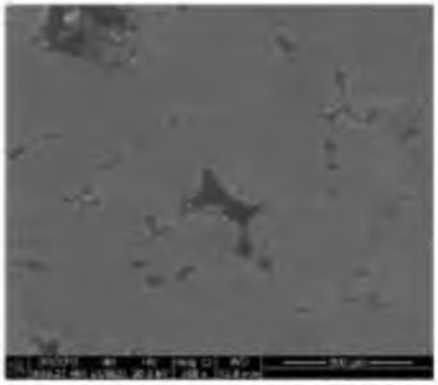

Vermillion EXP 5806-1P 13985

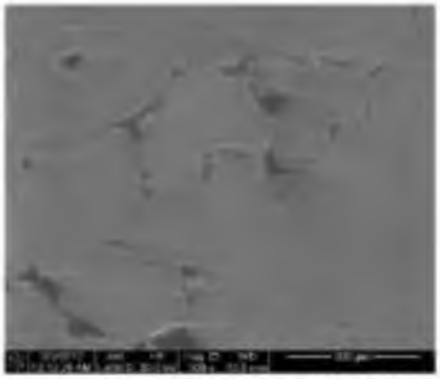

Vermillion EXP 5806-1P 13992

Figure 13. Continued

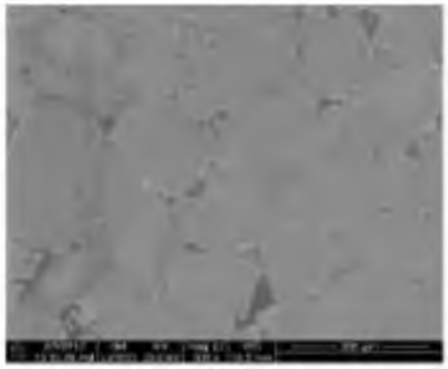

Vermillion EXP 5806-1P 13993

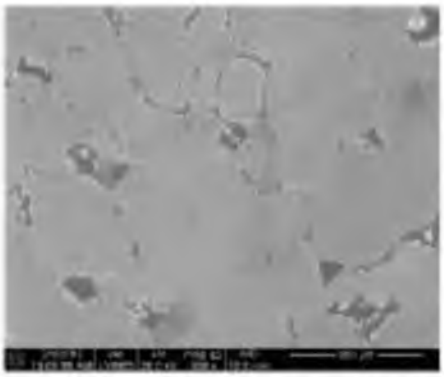

Vermillion EXP 5806-1P 13988

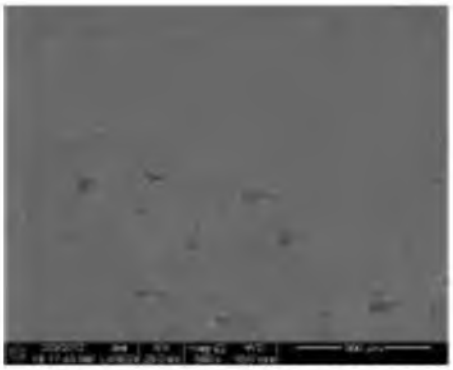

Vermillion EXP 5806-1P 13994

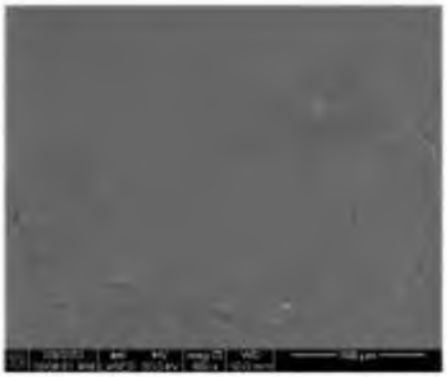

Vermillion EXP 5806-1P 13989

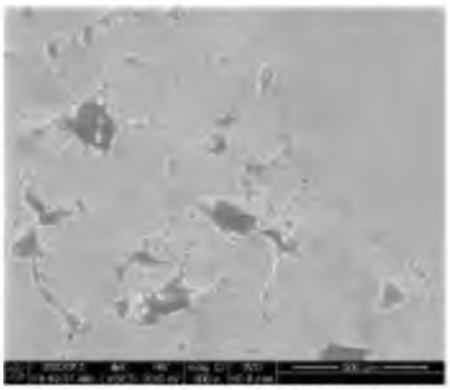

Vermillion EXP 5806-1P 13995

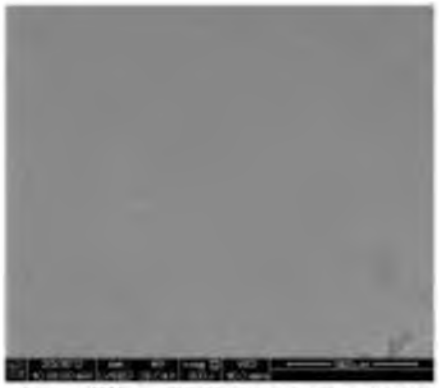

Vermillion EXP 5806-1P 13990

Figure 13. Continued

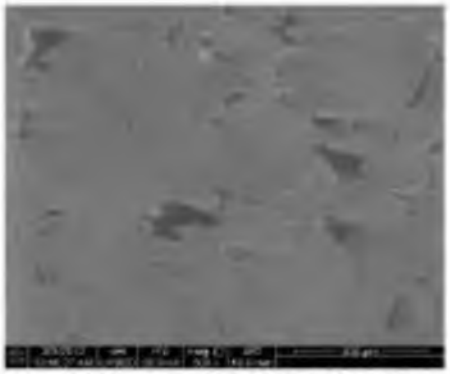

Vermillion EXP 5806-1P 1391

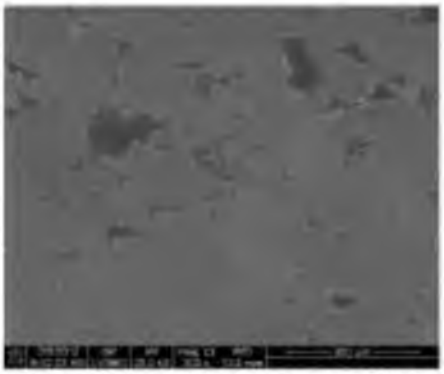

Vermillion EXP 5806-1P 13982

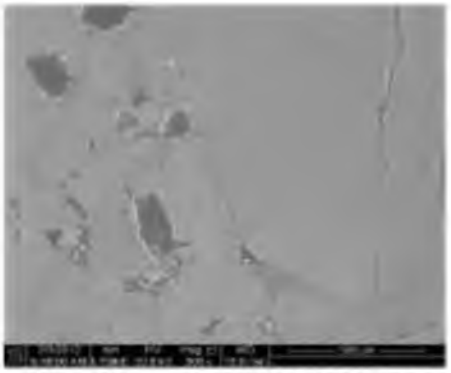

Vermillion EXP 5806-1P 13980

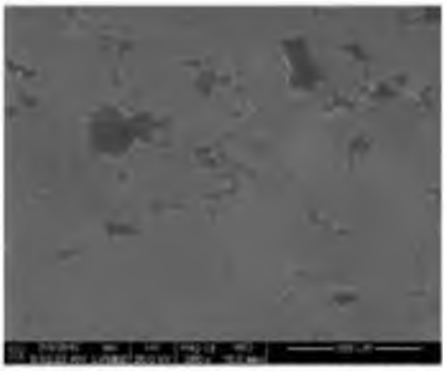

Vermillion EXP 5806-1P 13983

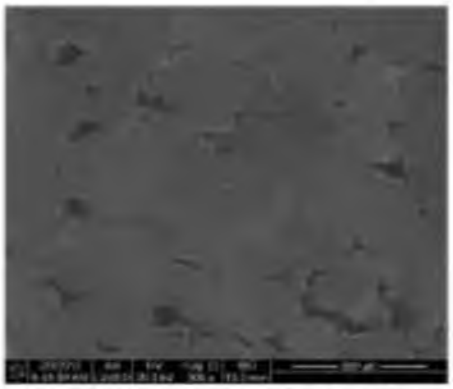

Vermillion EXP 5806-1P 13981

Figure 13. Continued

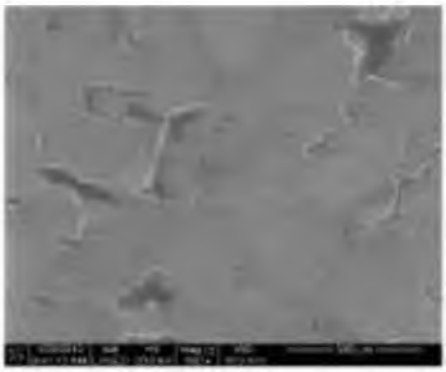

Vermillion EXP 5806-1P 13790

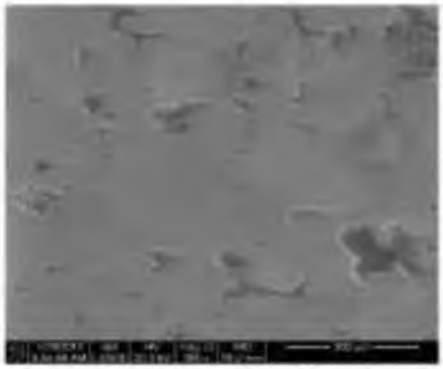

Vermillion EXP 5806-1P 13793

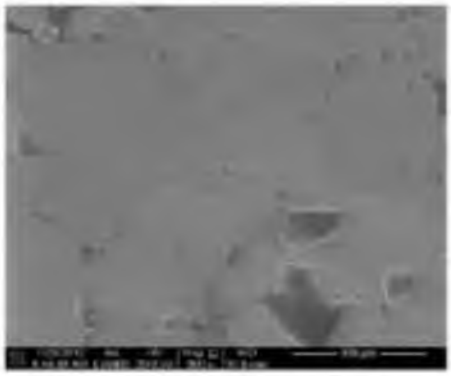

Vermillion EXP 5806-1P 13791

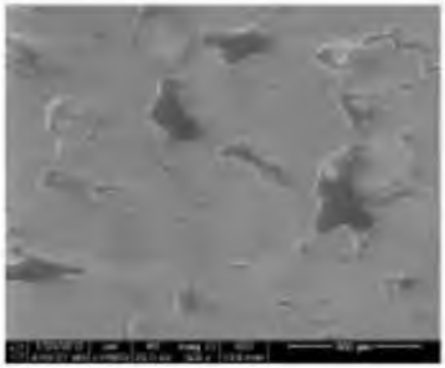

Vermillion EXP 5806-1P 13794

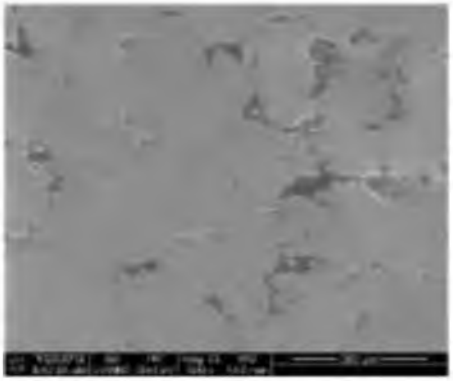

Vermillion EXP 5806-1P 13792

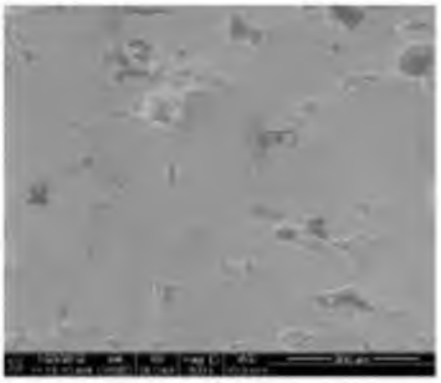

Vermillion EXP 5806-1P 13815

Figure 13. Continued

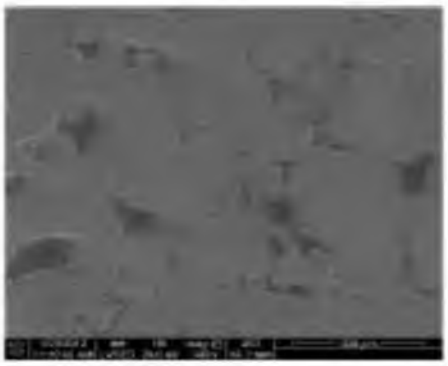

Vermillion EXP 5806-1P 13816

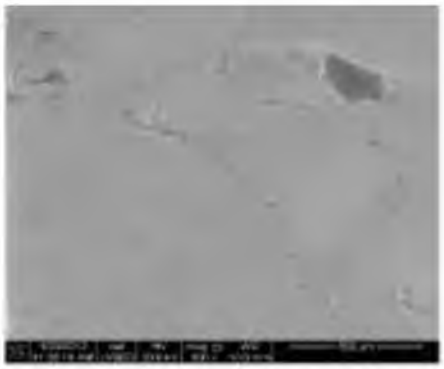

Vermillion EXP 5806-1P 13819

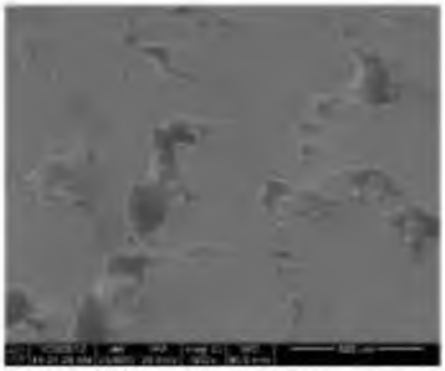

Vermillion EXP 5806-1P 13817

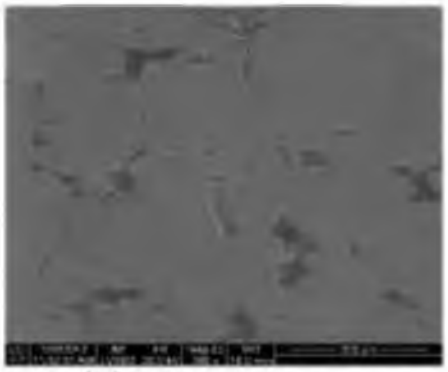

Vermillion EXP 5806-1P 13820

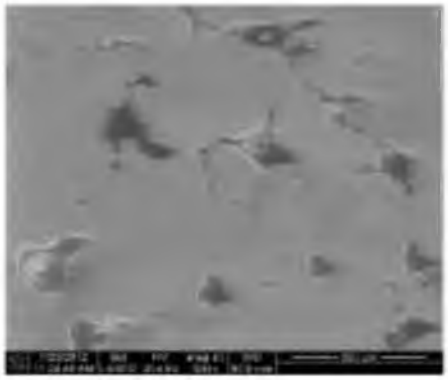

Vermillion EXP 5806-1P 13818

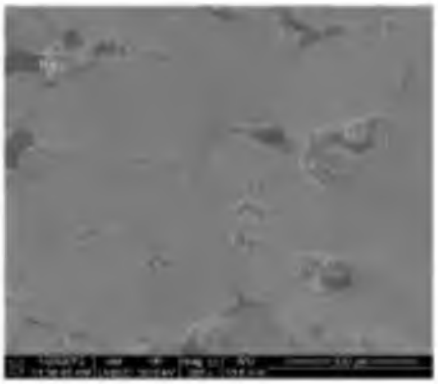

Vermillion EXP 5806-1P 13821

Figure 13. Continued

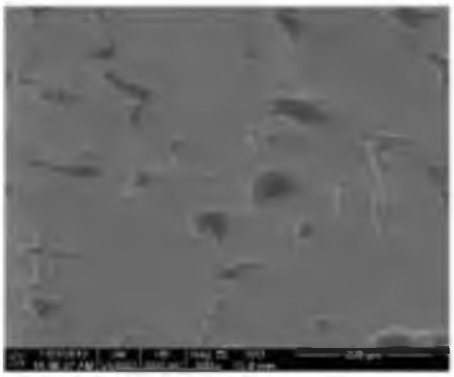

Vermillion EXP 5806-1P 13822

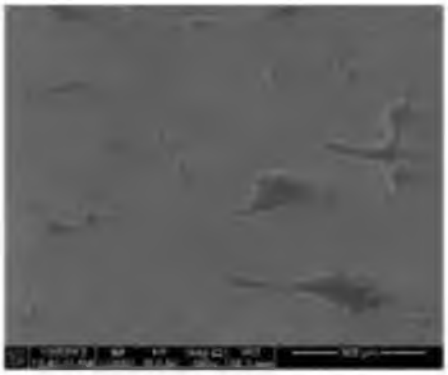

Vermillion EXP 5806-1P 13805

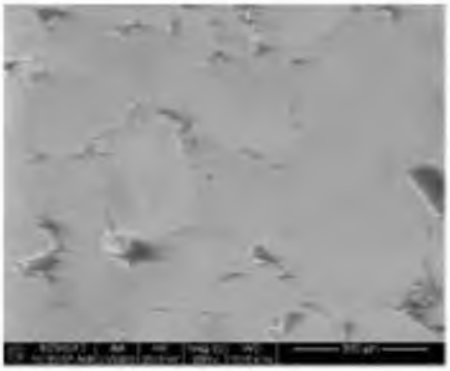

Vermillion EXP 5806-1P 13803

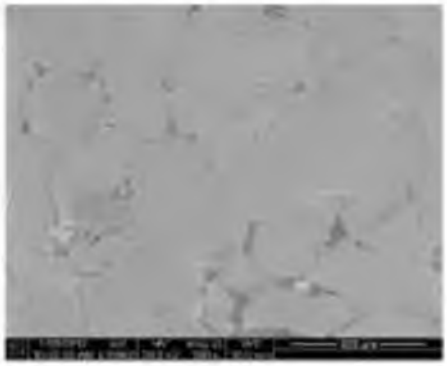

Vermillion EXP 5806-1P 13806

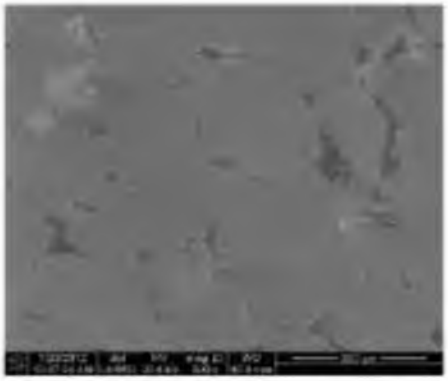

Vermillion EXP 5806-1P 13804

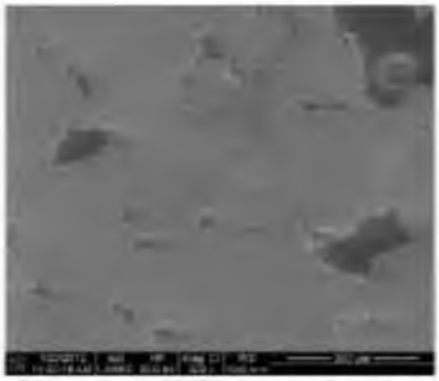

Vermillion EXP 5806-1P 13811

Figure 13. Continued

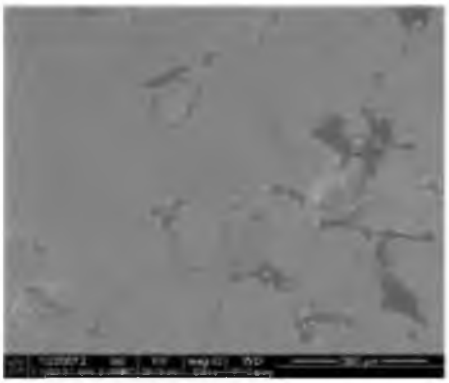

Vermillion EXP 5806-1P 13812

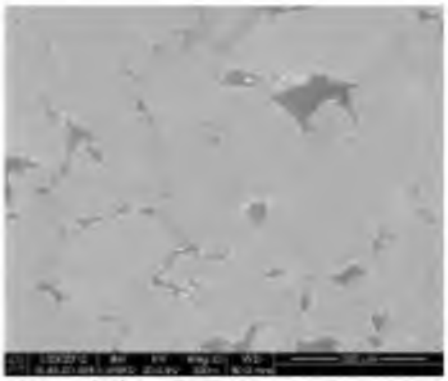

Vermillion EXP 5806-1P 13807

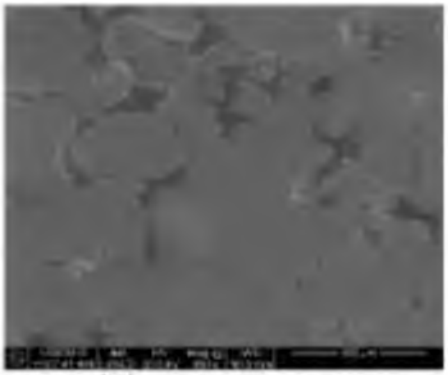

Vermillion EXP 5806-1P 13813

Vermillion EXP 5806-1P 13808

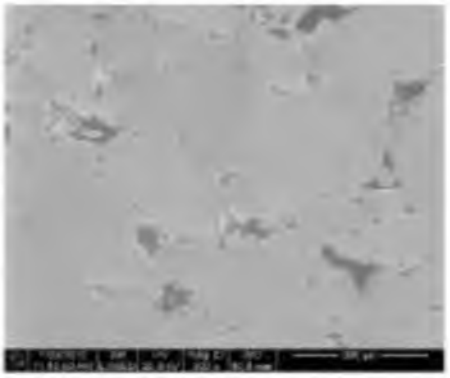

Vermillion EXP 5806-1P 13814

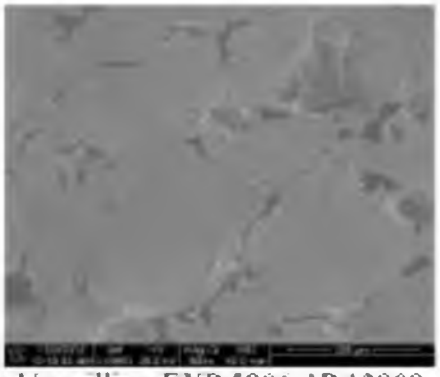

Vermillion EXP 5806-1P 13809

Figure 13. Continued

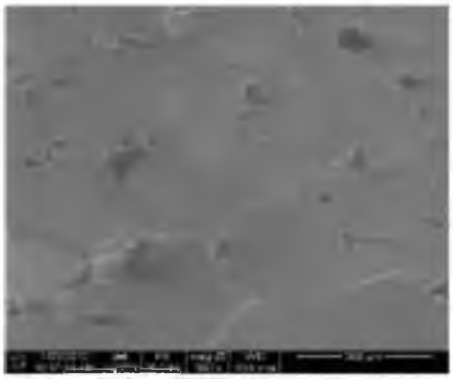

Vermillion EXP 5806-1P 13810

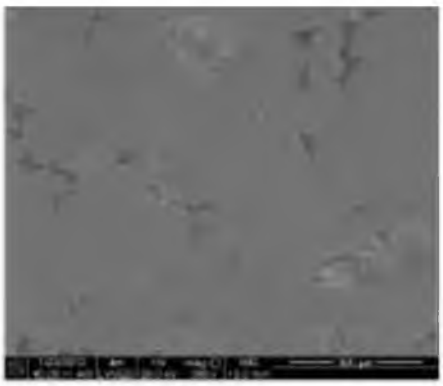

Vermillion EXP 5806-1P 13801

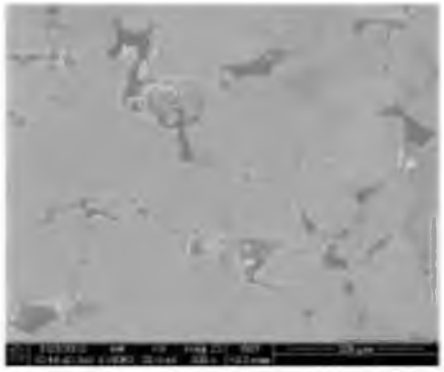

Vermillion EXP 5806-1P 13798

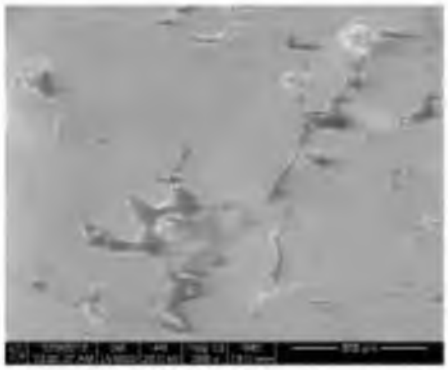

Vermillion EXP 5806-1P 13802

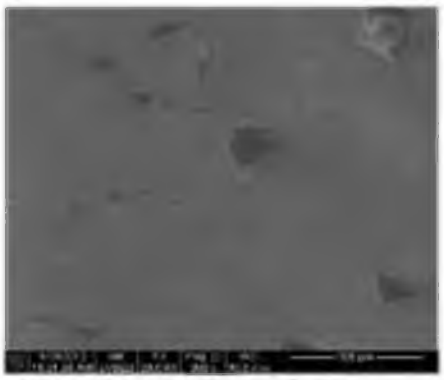

Vermillion EXP 5806-1P 13799

Figure 13. Continued

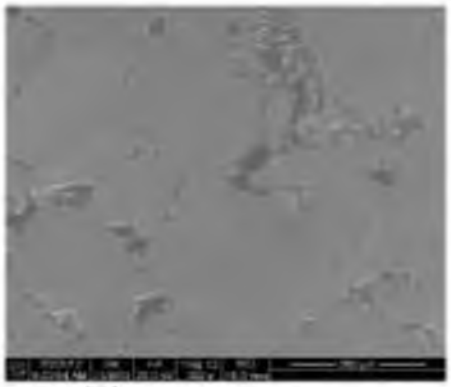

Vermillion EXP 5806-1P 14539

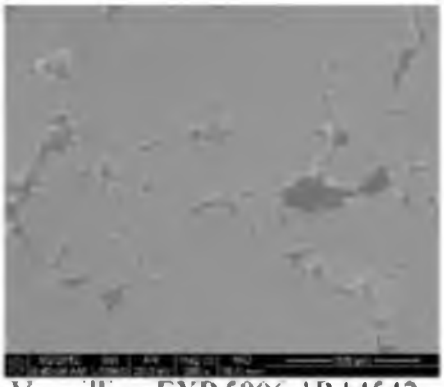

Vermillion EXP 5806-1P 14542

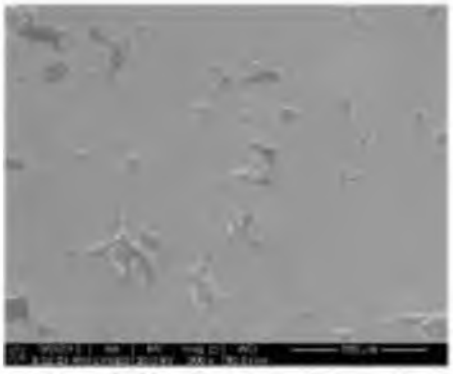

Vermillion EXP 5806-1P 14540

Vermillion EXP 5806-1P 14543

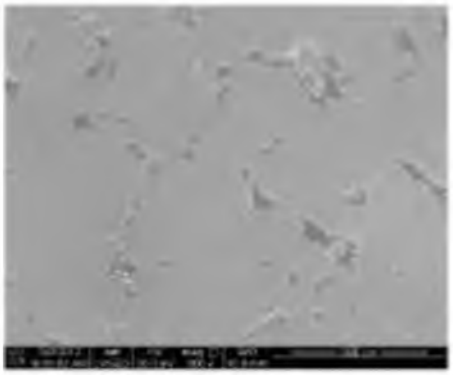

Vermillion EXP 5806-1P 14541

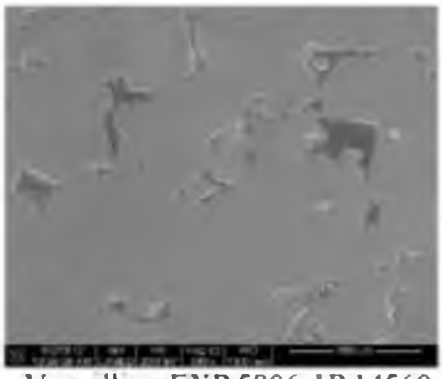

Vermillion EXP 5806-1P 14560

Figure 13. Continued

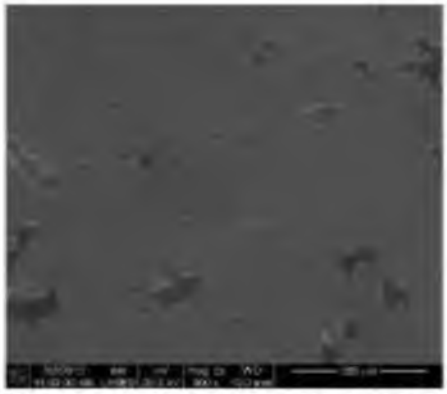

Vermillion EXP 5806-1P 14561

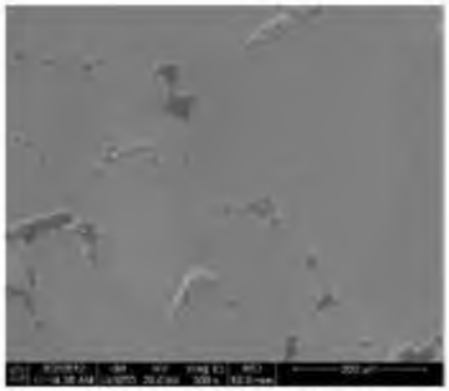

Vermillion EXP 5806-1P 14564

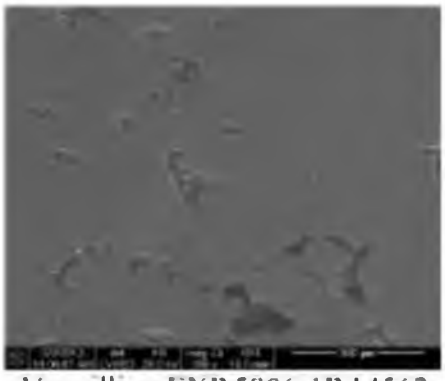

Vermillion EXP 5806-1P 14562

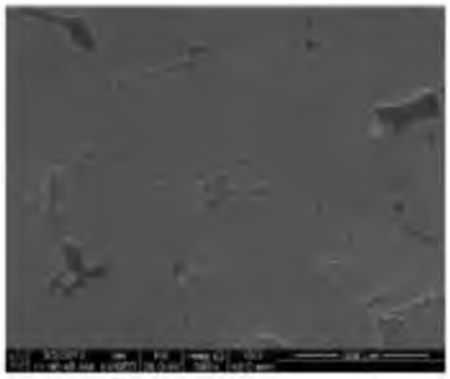

Vermillion EXP 5806-1P 14565

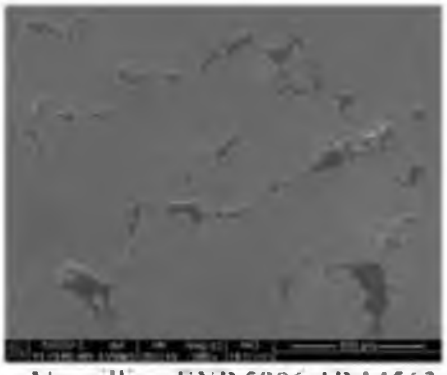

Vermillion EXP 5806-1P 14563

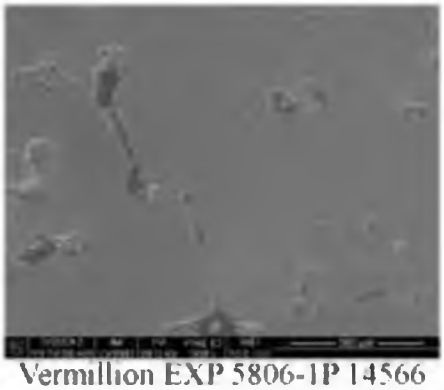

Vermillion EXP 5806-1P 14566

Figure 13. Continued

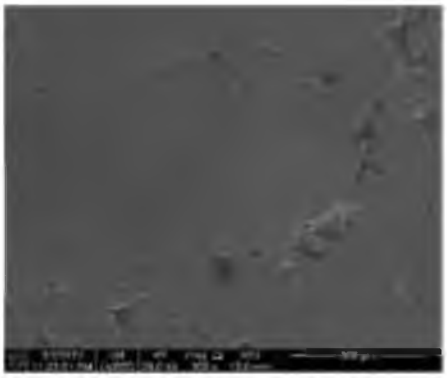

Vermillion EXP 5806-1P 14567

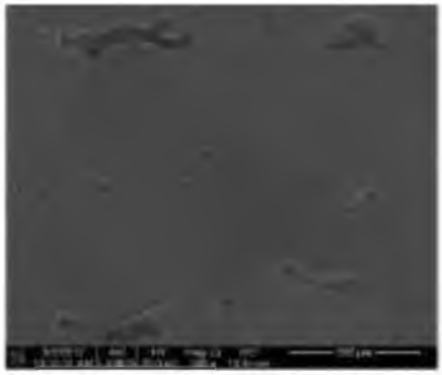

Vermillion EXP 5806-1P 14550

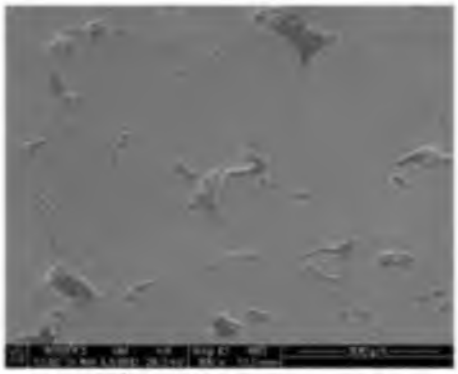

Vermillion EXP 5806-1P 14548

Vermillion EXP 5806-1P 14551

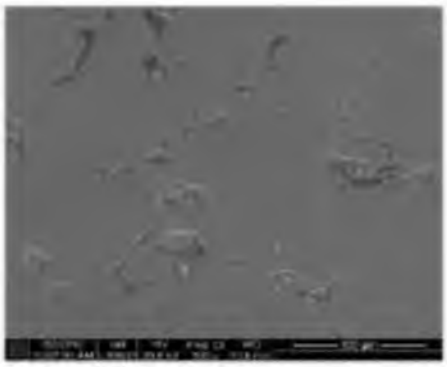

Vermillion EXP 5806-1P 14549

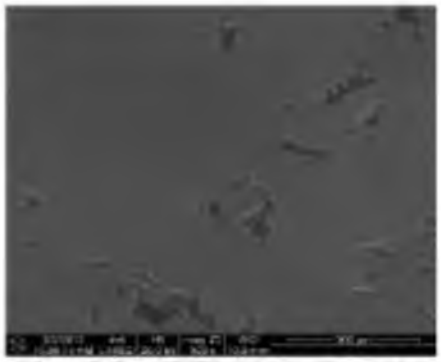

Vermillion EXP 5806-1P 14556

Figure 13. Continued

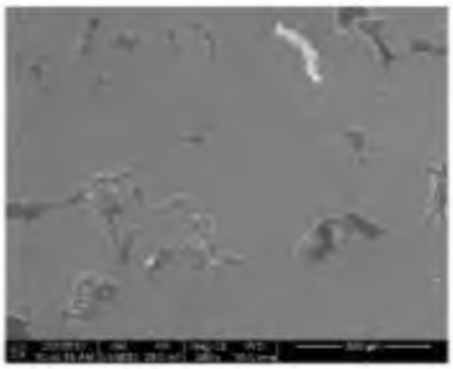

Vermillion EXP 5806-1P 14557

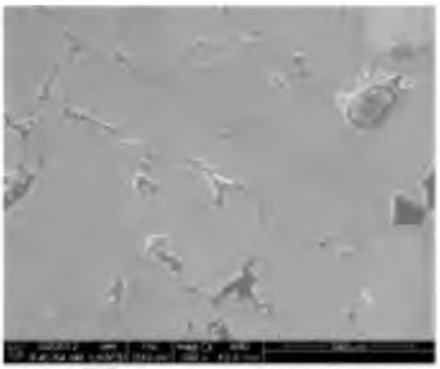

Vermillion EXP 5806-1P 14544

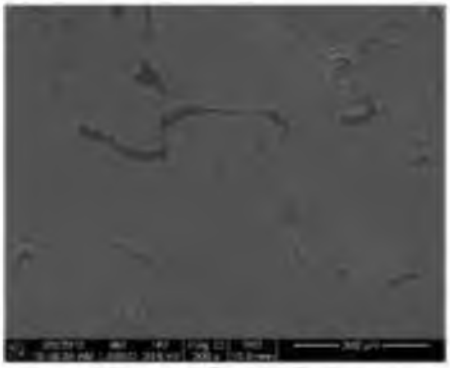

Vermillion EXP 5806-1P 14558

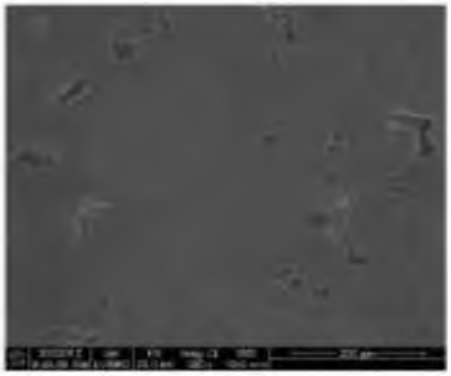

Vermillion EXP 5806-1P 14545

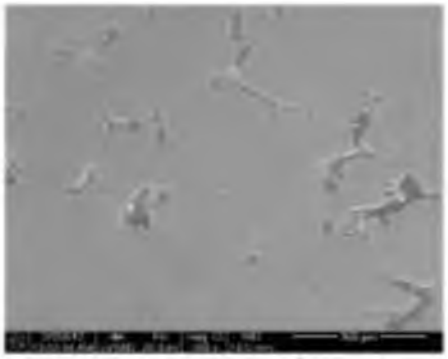

Vermillion EXP 5806-1P 14559

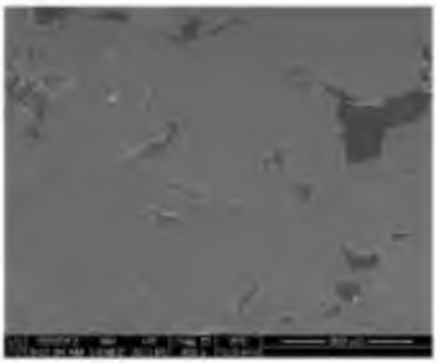

Vermillion EXP 5806-1P 14546

Figure 13. Continued

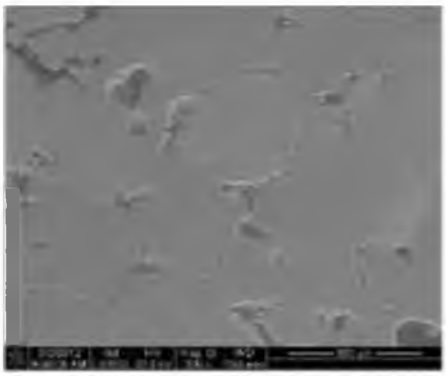

Vermillion EXP 5806-1P 14547

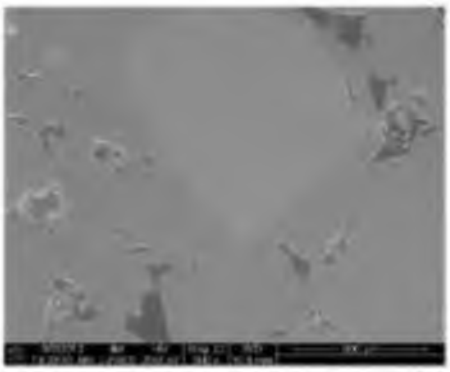

Vermillion EXP 5806-1P 14554

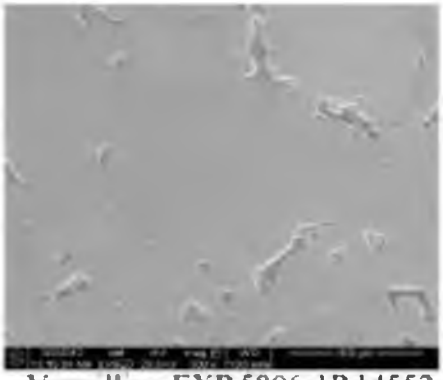

Vermillion EXP 5806-1P 14552

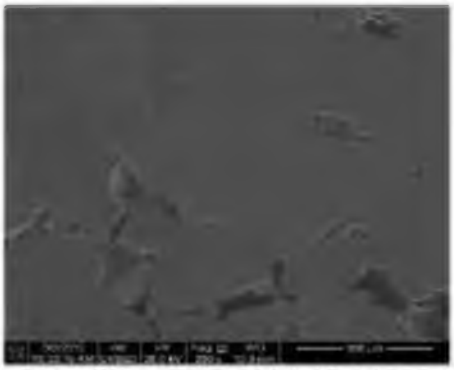

Vermillion EXP 5806-1P 14555

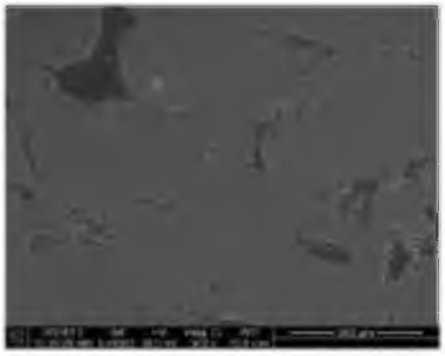

Vermillion EXP 5806-1P 14553

Figure 13. Continued

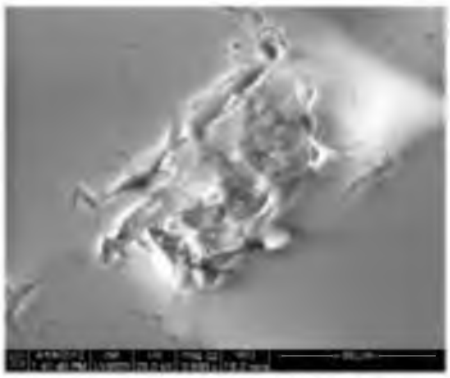

Knox EXP 8642.5-1P 17160

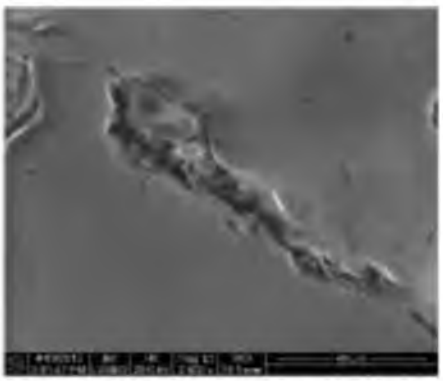

Knox EXP 8642.5-1P 17163

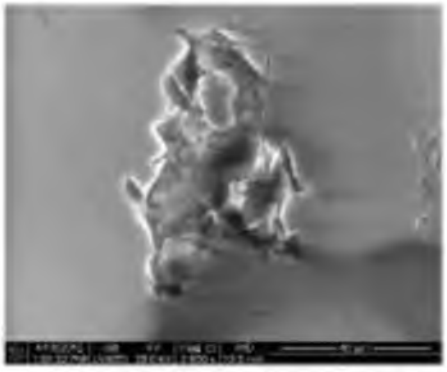

Knox EXP 8642.5-1P 17161

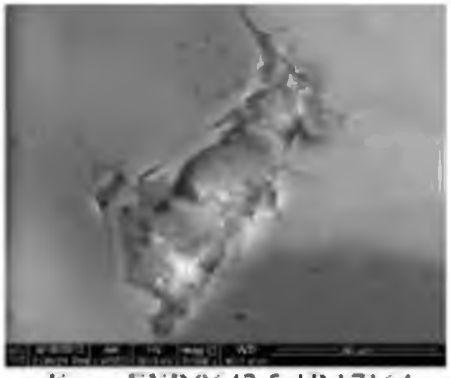

Knox EXP 8642.5-1P 17164

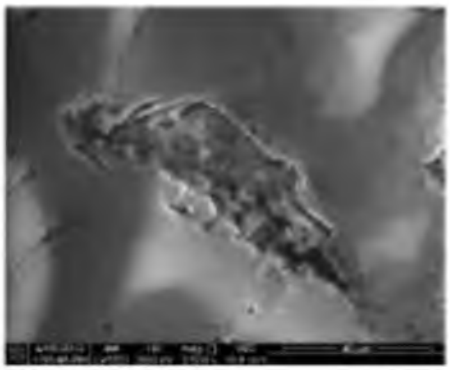

Knox EXP 8642.5-1P 17162

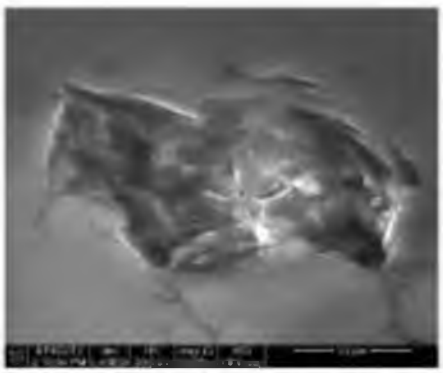

Knox EXP 8642.5-1P 17165

Figure 14. Pore SEM Images

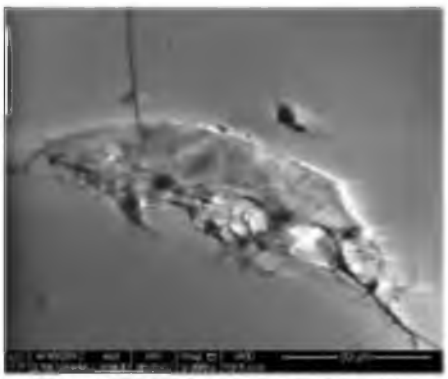
Knox EXP 8642.5-1P 17166

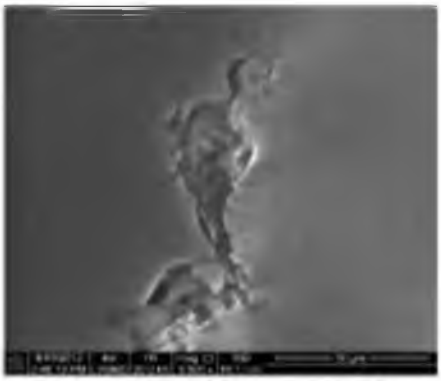
Knox EXP 8642.5-1P 17169

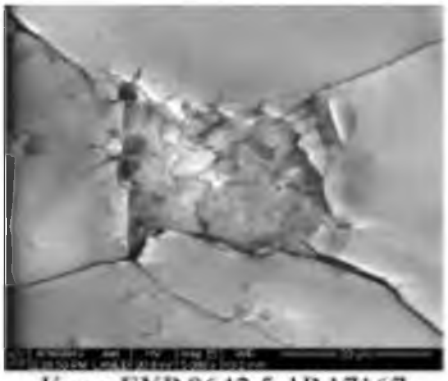
Knox EXP 8642.5-1P 17167

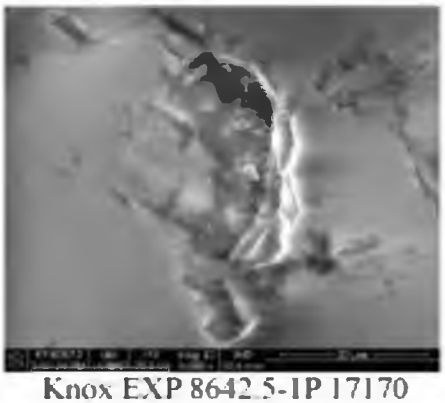
Knox EXP 8642.5-1P 17170

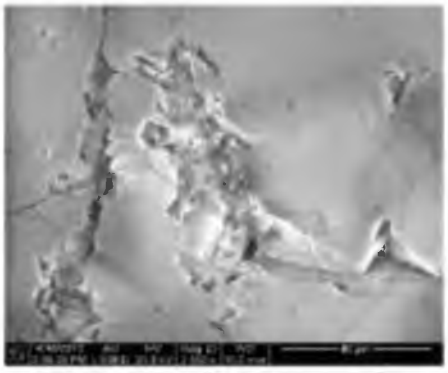
Knox EXP 8642.5-1P 17168

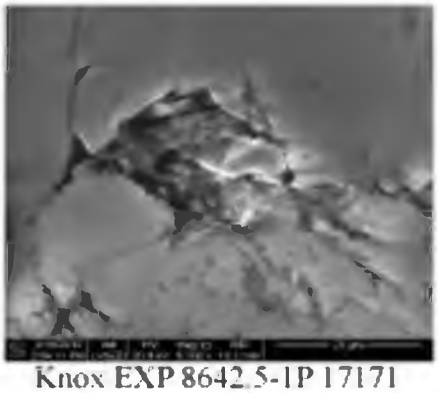
Knox EXP 8642.5-1P 17171

Figure 14. Continued

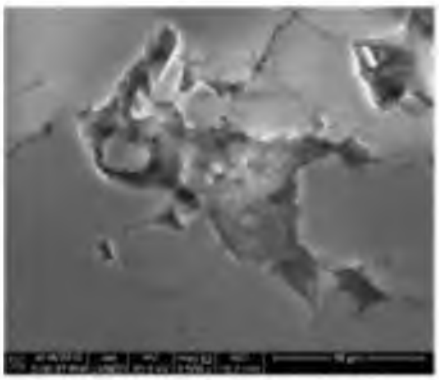

Knox EXP 8642.5-1P 17172

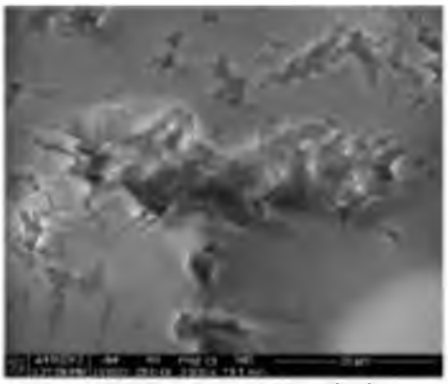

Knox EXP 8642.5-1P 17175

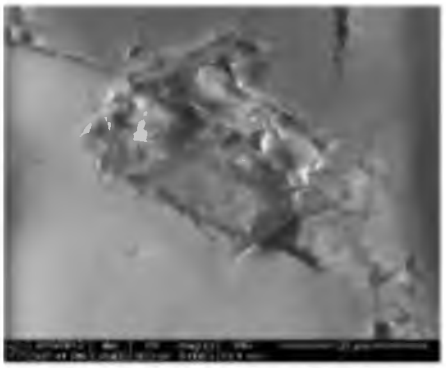

Knox EXP 8642.5-1P 17173

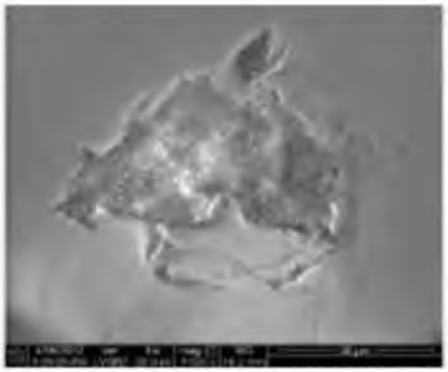

Knox EXP 8642.5-1P 17176

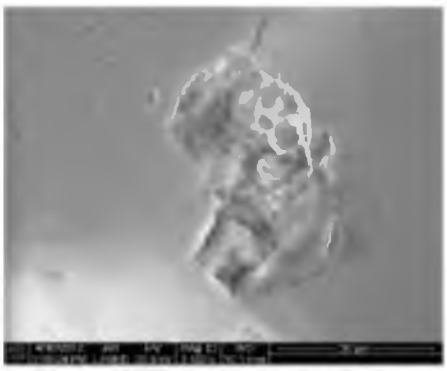

Knox EXP 8642.5-1P 17174

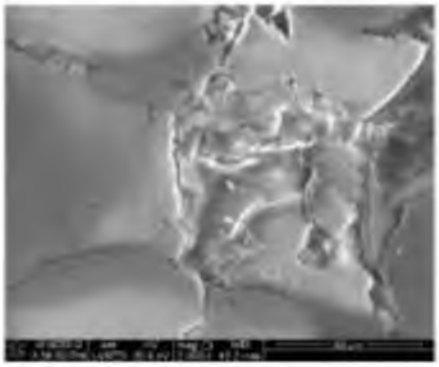

Knox EXP 8642.5-1P 17179

Figure 14. Continued

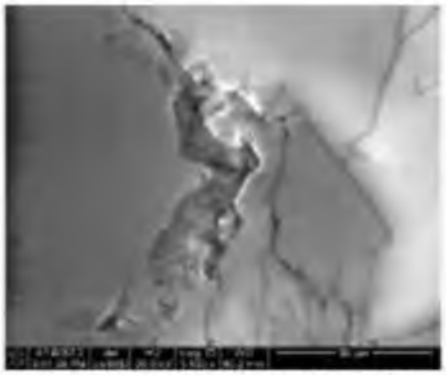

Knox EXP 8642.5-1P 17182

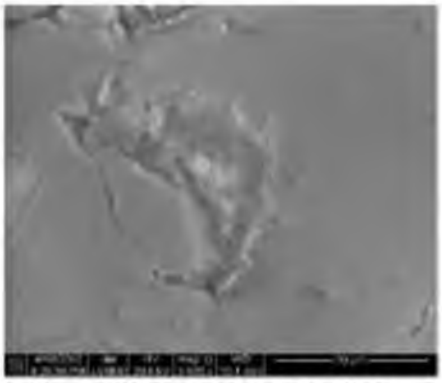

Knox EXP 8642.5-1P 17191

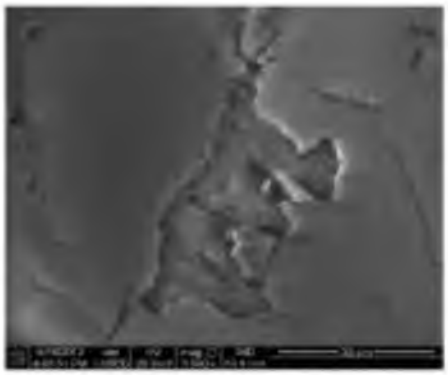

Knox EXP 8642.5-1P 17185

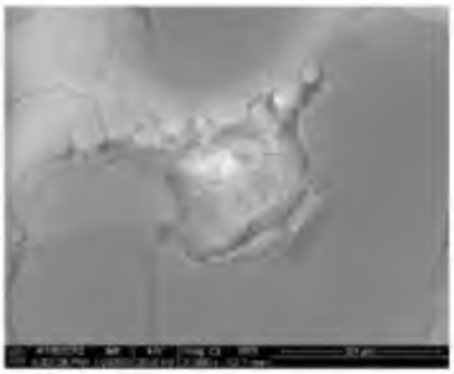

Knox EXP 8642.5-1P 17194

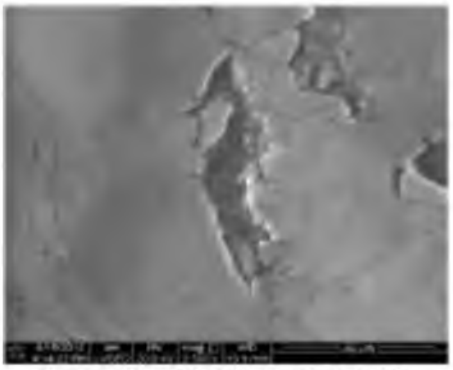

Knox EXP 8642.5-1P 17188

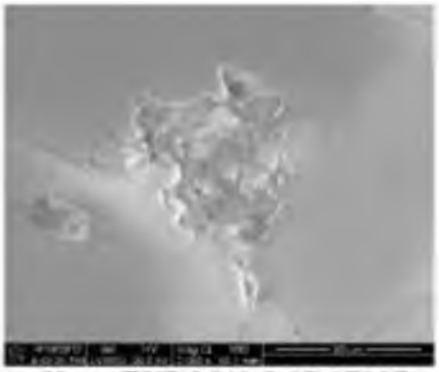

Knox EXP 8642.5-1P 17197

Figure 14. Continued

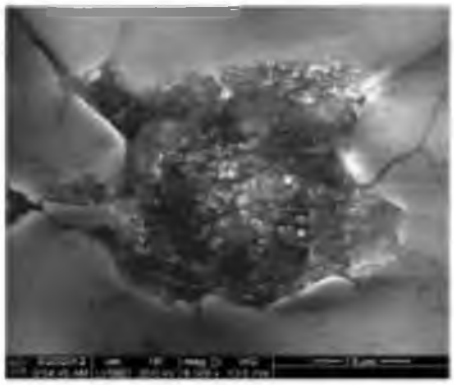

Knox EXP 8642.5-2P 16830

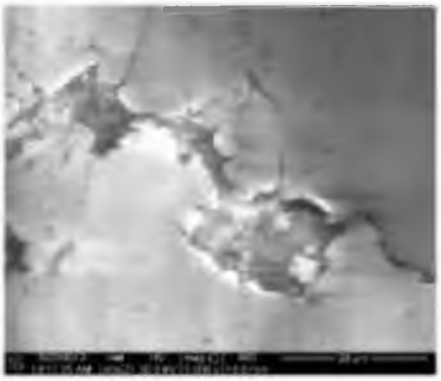

Knox EXP 8642.5-2P 16833

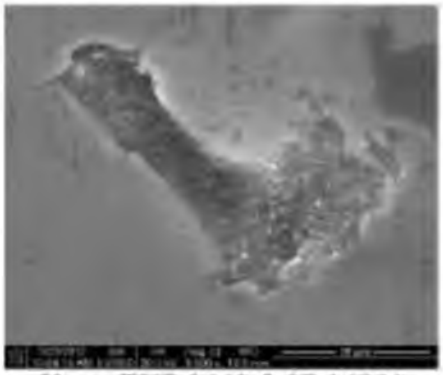

Knox EXP 8642.5-2P 16831

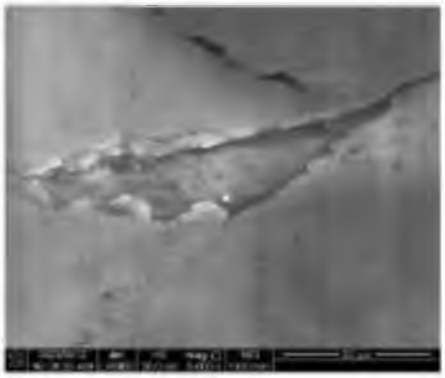

Knox EXP 8642.5-2P 16834

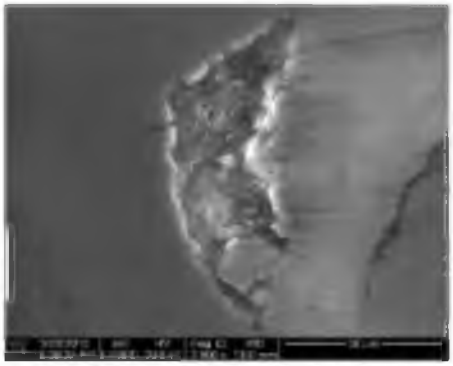

Knox EXP 8642.5-2P 16832

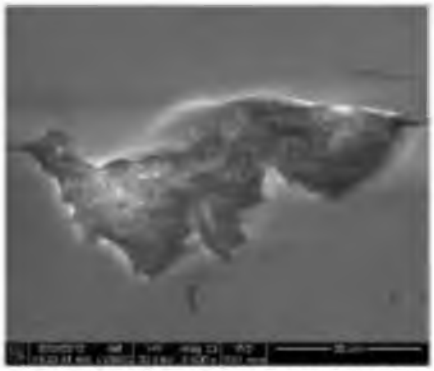

Knox EXP 8642.5-2P 16835

Figure 14. Continued

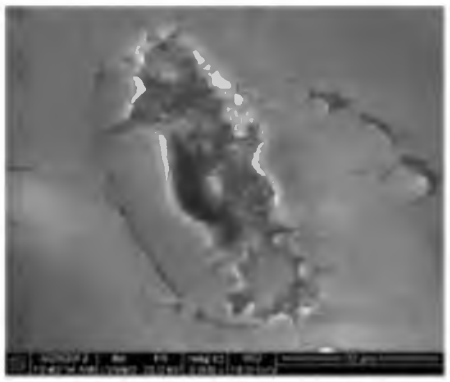
Knox EXP 8642.5-2P 16836

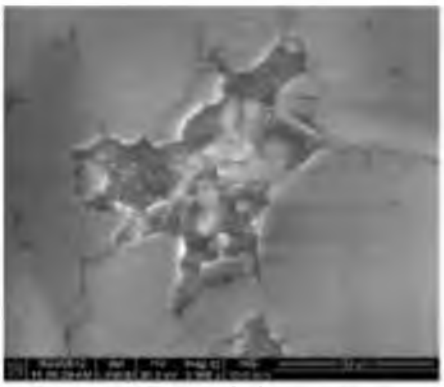
Knox EXP 8642.5-2P 16839

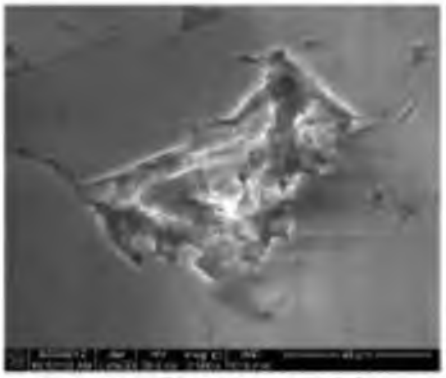
Knox EXP 8642.5-2P 16837

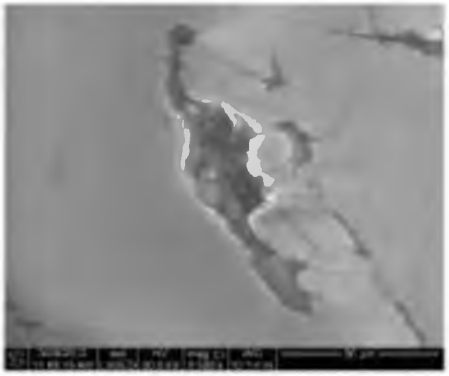
Knox EXP 8642.5-2P 16840


Knox EXP 8642.5-2P 16838

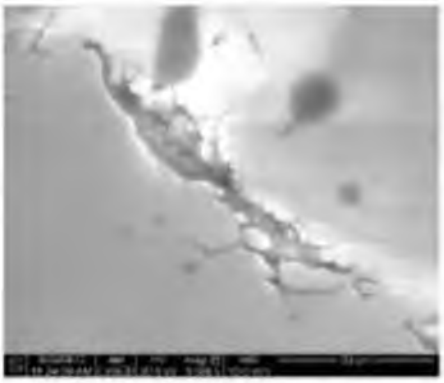
Knox EXP 8642.5-2P 16841

Figure 14. Continued

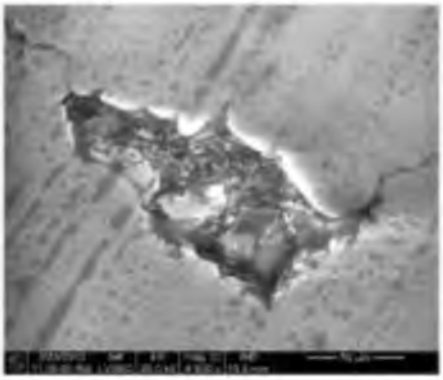

Knox EXP 8642.5-2P 16842

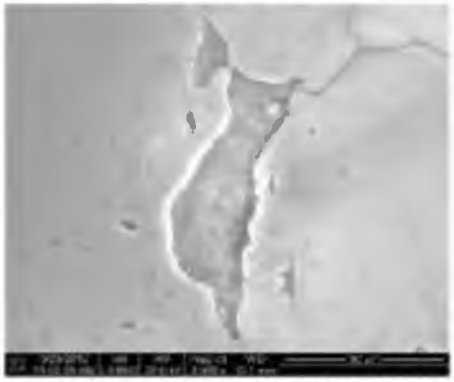

Knox EXP 8642.5-2P 16845

Knox EXP 8642.5-2P 16843

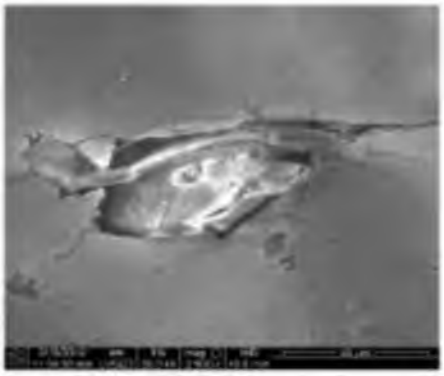

Knox EXP 8642.5-2P 14142

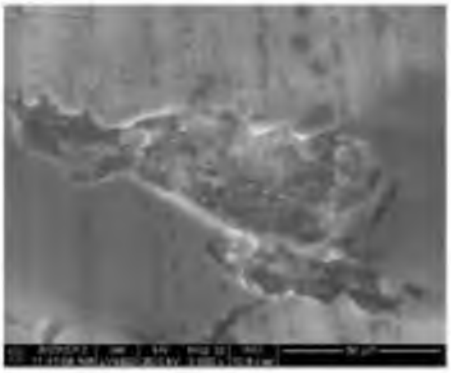

Knox EXP 8642.5-2P 16844

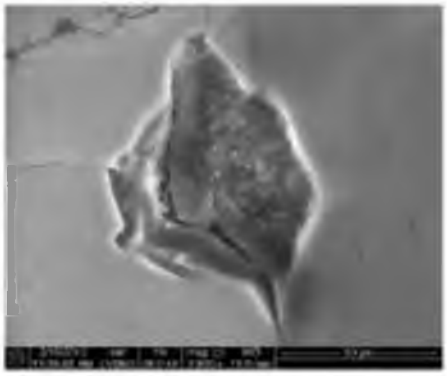

Knox EXP 8642.5-2P 14145

Figure 14. Continued

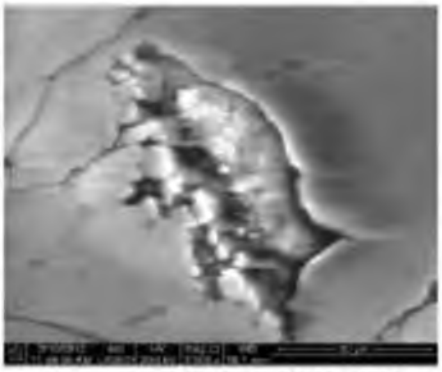

Knox EXP 8642.5-2P 14148

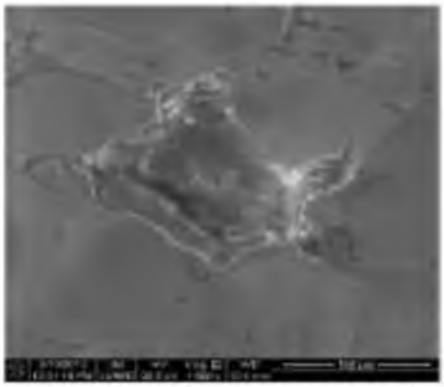

Knox EXP 8642.5-2P 14162

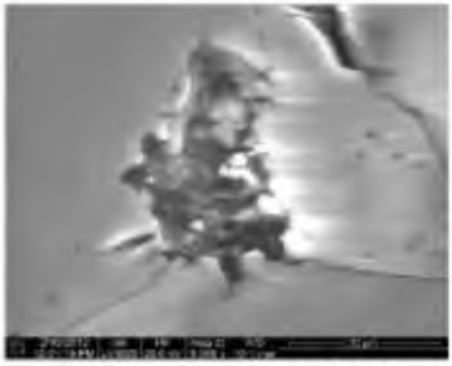

Knox EXP 8642.5-2P 14151

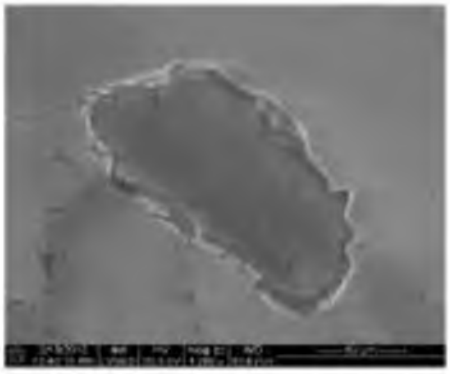

Knox EXP 8642.5-2P 14165

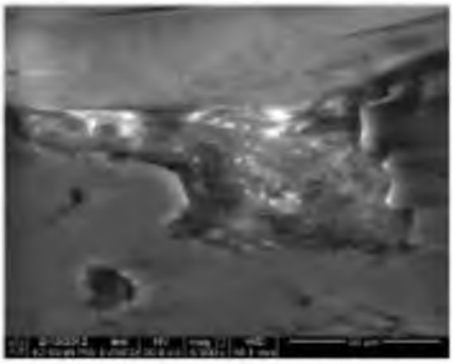

Knox EXP 8642.5-2P 14154

Figure 14. Continued

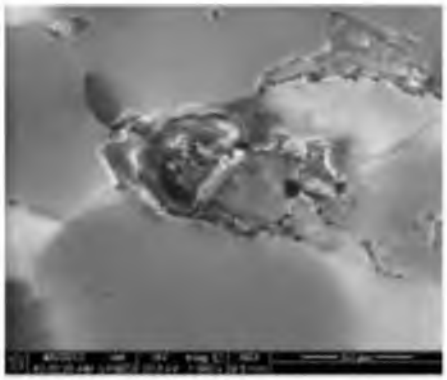

Knox EXP 8642.5-3P 17028

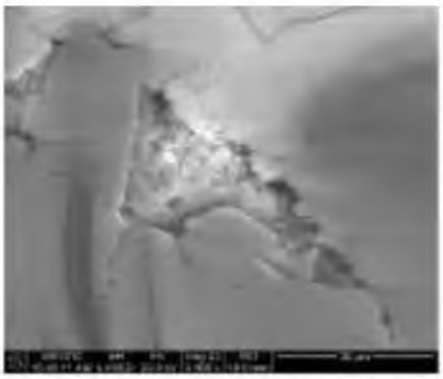

Knox EXP 8642.5-3P 17031

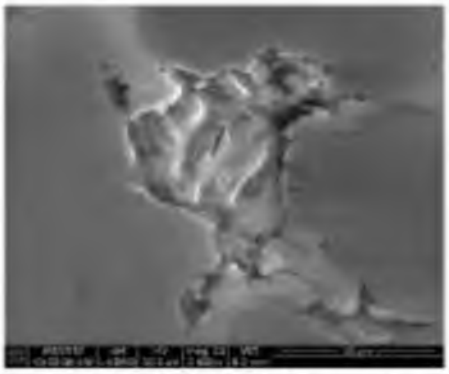

Knox EXP 8642.5-3P 17029

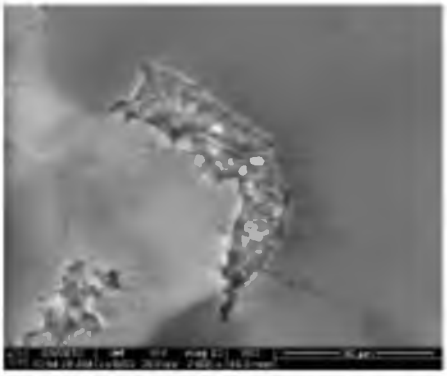

Knox EXP 8642.5-3P 17032

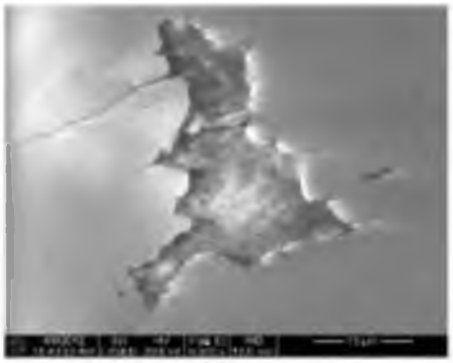

Knox EXP 8642.5-3P 17030

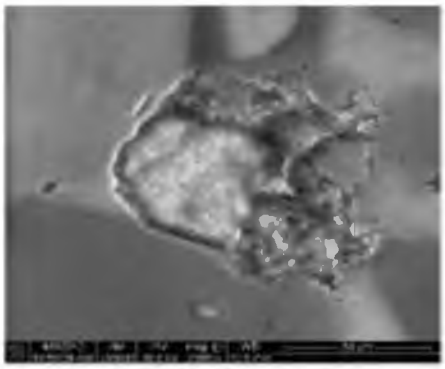

Knox EXP 8642.5-3P 17033

Figure 14. Continued

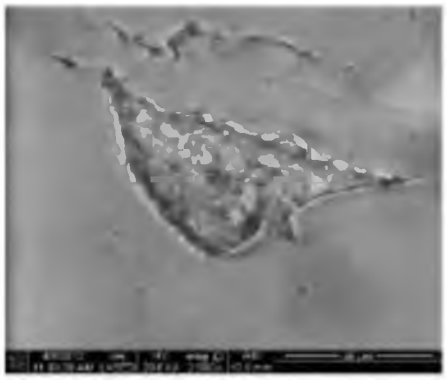

Knox EXP 8642.5-3P 17034

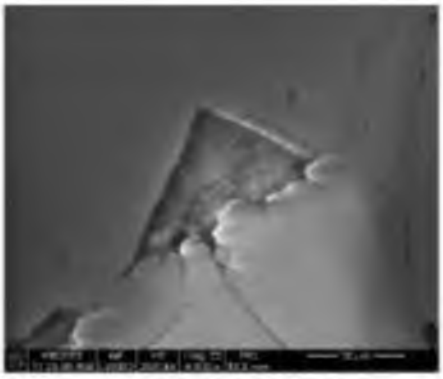

Knox EXP 8642.5-3P 17037

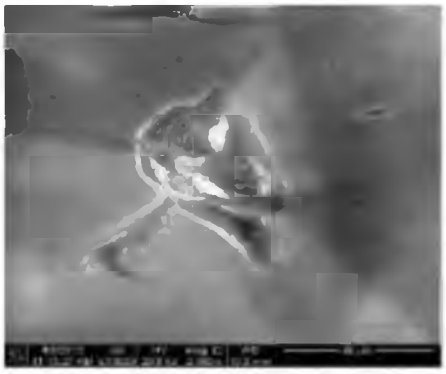

Knox EXP 8642.5-3P 17035

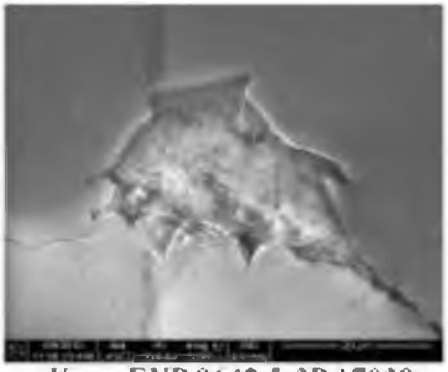

Knox EXP 8642.5-3P 17038

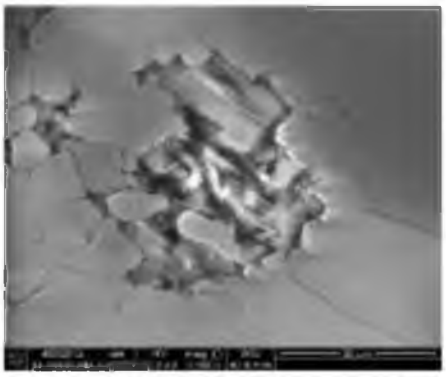

Knox EXP 8642.5-3P 17036

Knox EXP 8642.5-3P 17039

Figure 14. Continued

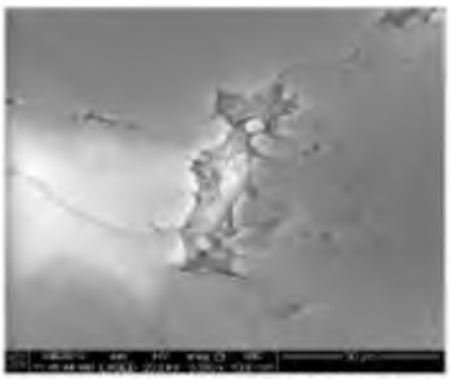

Knox EXP 8642.5-3P 17040

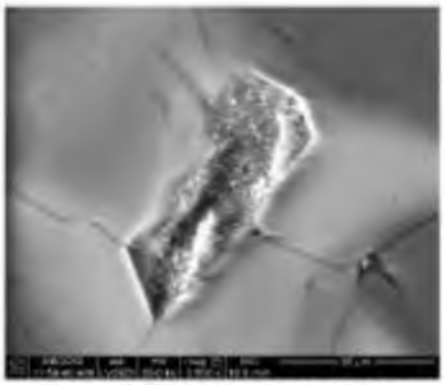

Knox EXP 8642.5-3P 17043

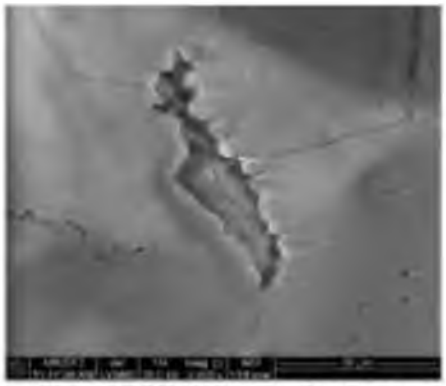

Knox EXP 8642.5-3P 17041

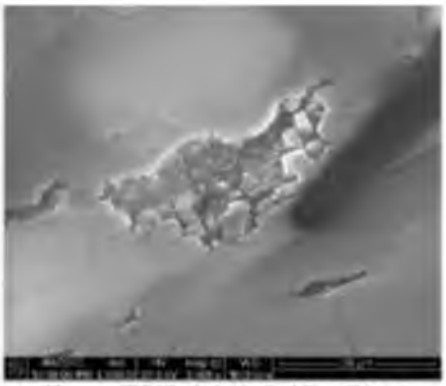

Knox EXP 8642.5-3P 17044

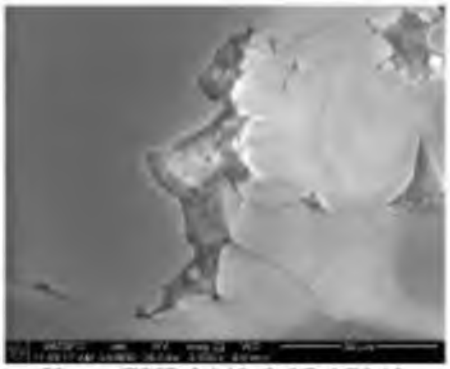

Knox EXP 8642.5-3P 17042

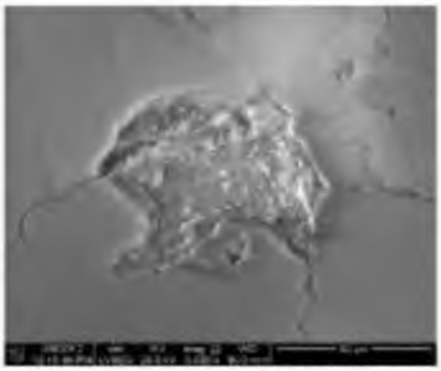

Knox EXP 8642.5-3P 17047

Figure 14. Continued

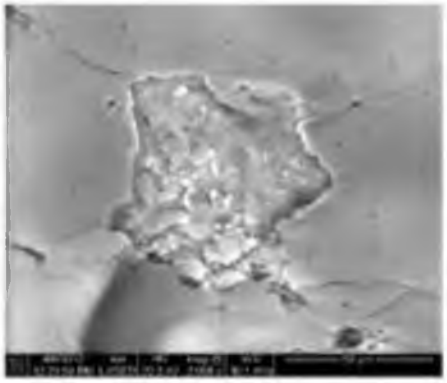

Knox EXP 8642.5-3P 17050

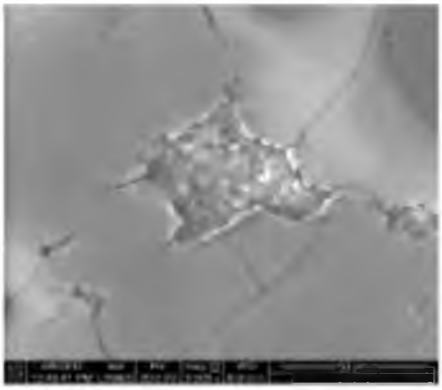

Knox EXP 8642.5-3P 17059

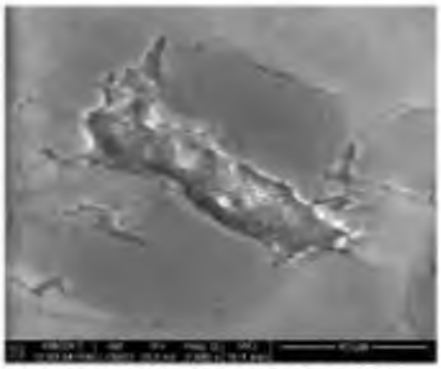

Knox EXP 8642.5-3P 17053

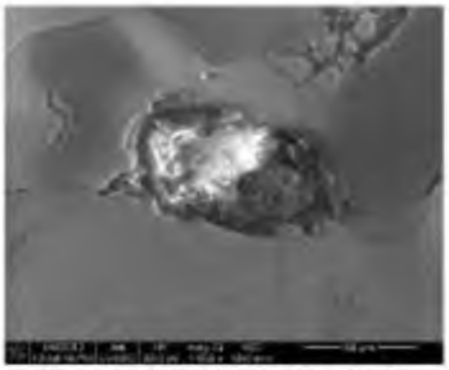

Knox EXP 8642.5-3P 17062

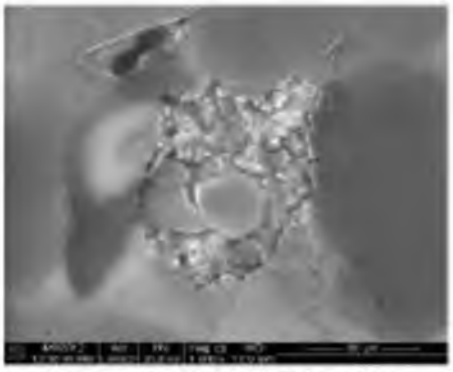

Knox EXP 8642.5-3P 17056

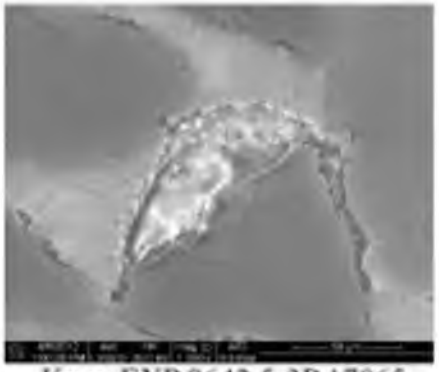

Knox EXP 8642.5-3P 17065

Figure 14. Continued

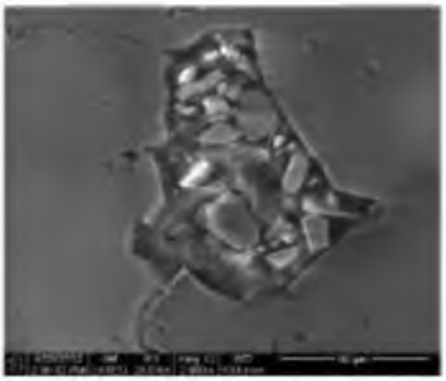
Vermillion EXP 5806-1P 17436

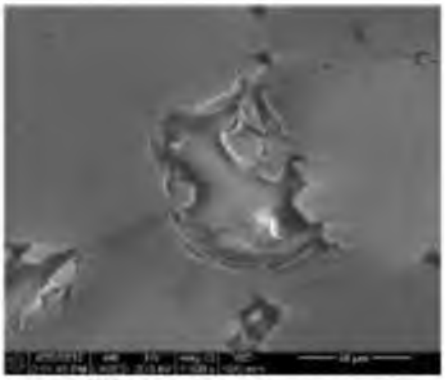
Vermillion EXP 5806-1P 17439


Vermillion EXP 5806-1P 17437

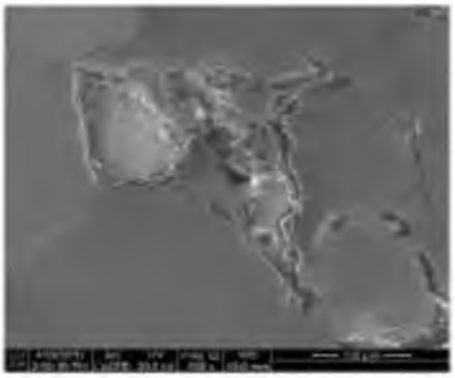
Vermillion EXP 5806-1P 17440

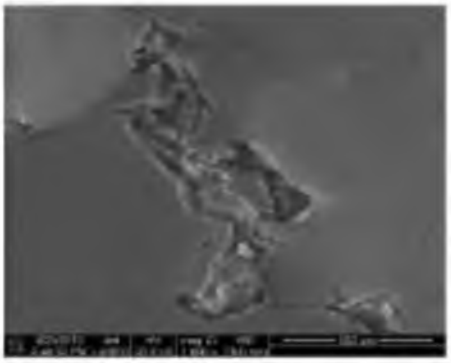
Vermillion EXP 5806-1P 17438

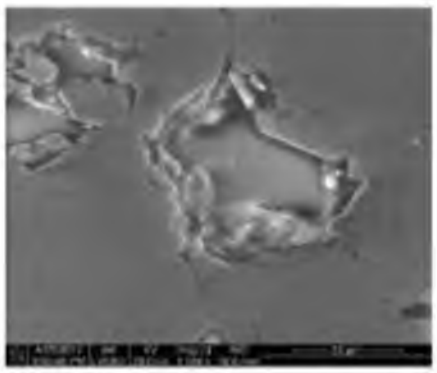
Vermillion EXP 5806-1P 17441

Figure 14. Continued

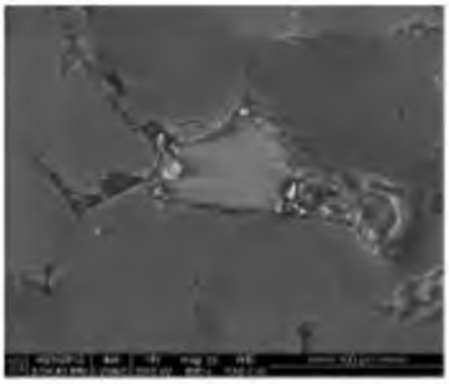

Vermillion EXP 5806-1P 17442

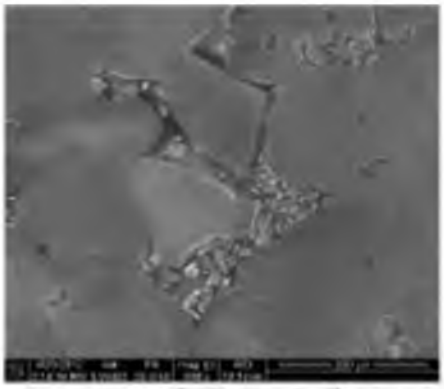

Vermillion EXP 5806-1P 17445

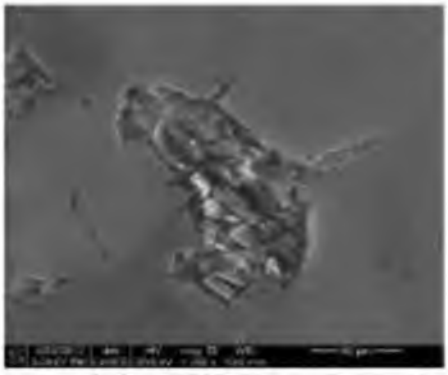

Vermillion EXP 5806-1P 17443

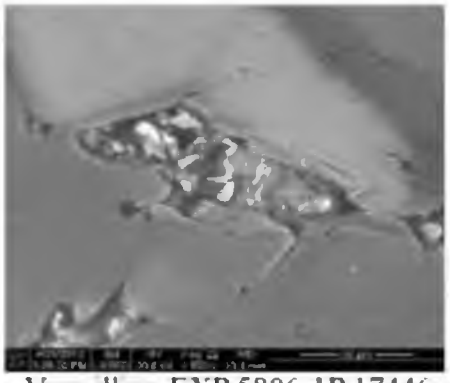

Vermillion EXP 5806-1P 17446

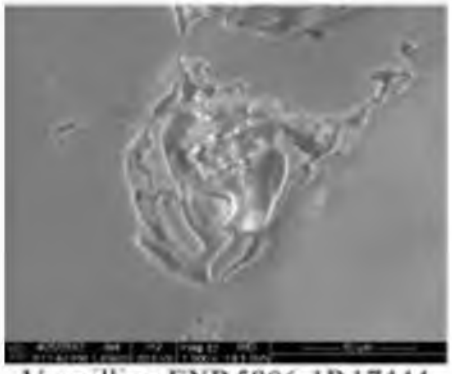

Vermillion EXP 5806-1P 17444

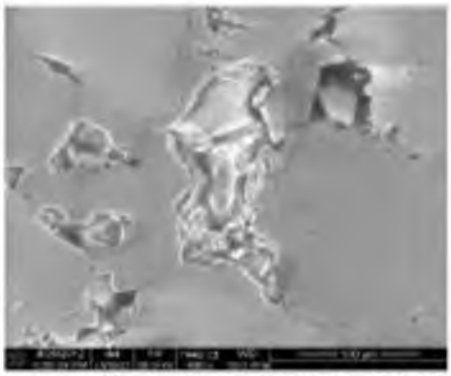

Vermillion EXP 5806-1P 17447

Figure 14. Continued

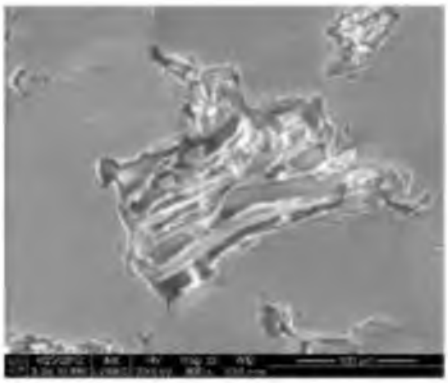

Vermillion EXP 5806-1P 17448

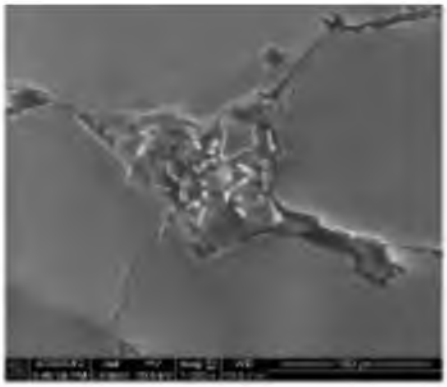

Vermillion EXP 5806-1P 17451

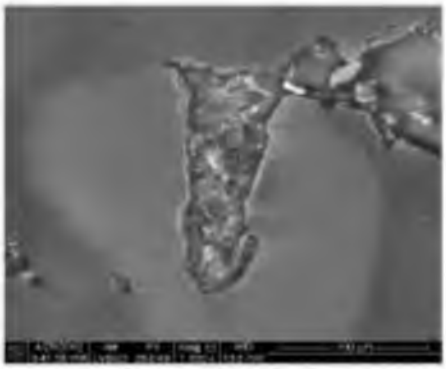

Vermillion EXP 5806-1P 17449

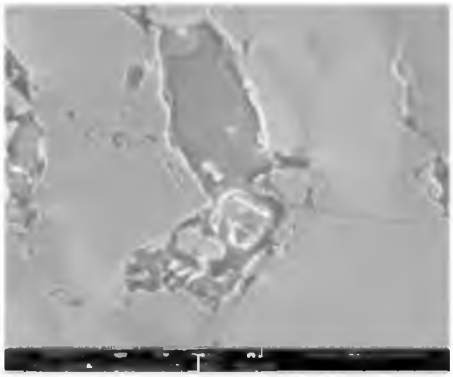

Vermillion EXP 5806-1P 14004

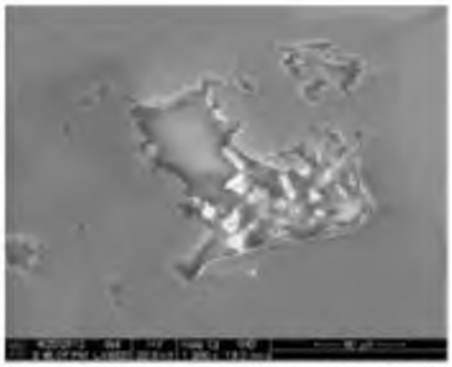

Vermillion EXP 5806-1P 17450

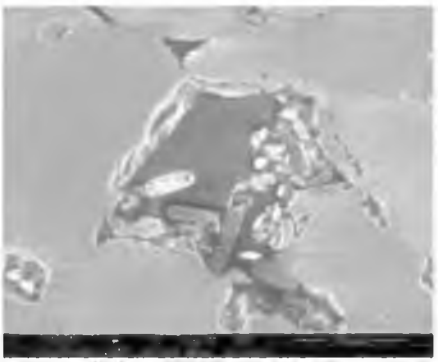

Vermillion EXP 5806-1P 14007

Figure 14. Continued

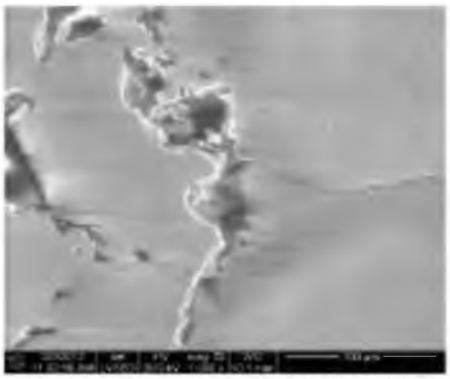
Vermillion EXP 5806-1P 14007

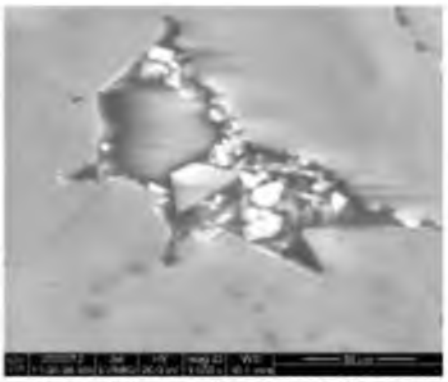
Vermillion EXP 5806-1P 14007

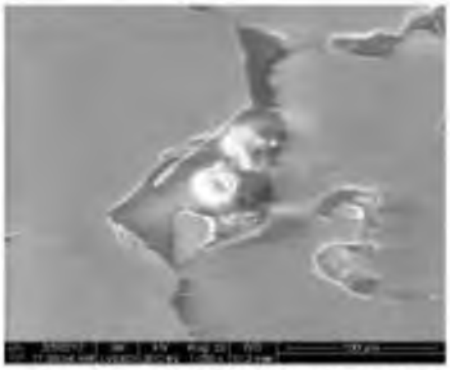
Vermillion EXP 5806-1P 14007

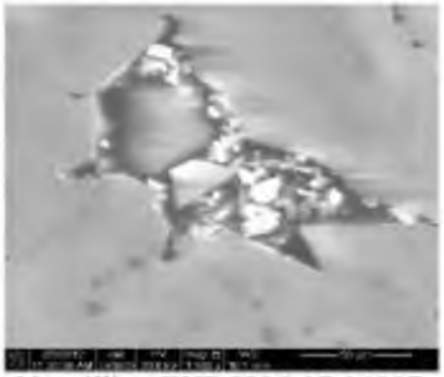
Vermillion EXP 5806-1P 14007

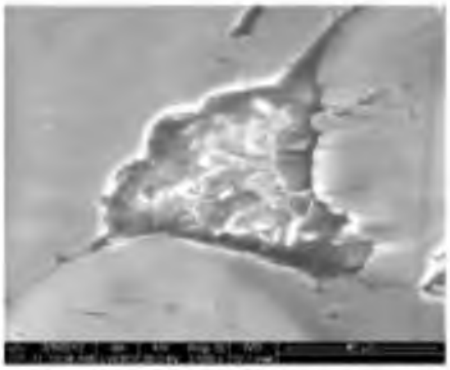
Vermillion EXP 5806-1P 14007

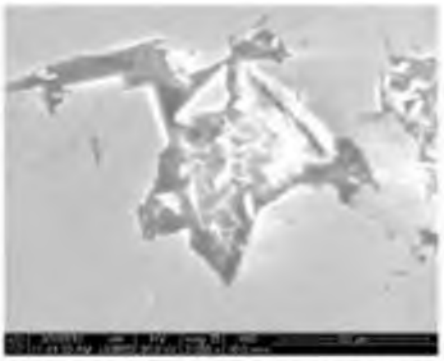
Vermillion EXP 5806-1P 14007

Figure 14. Continued

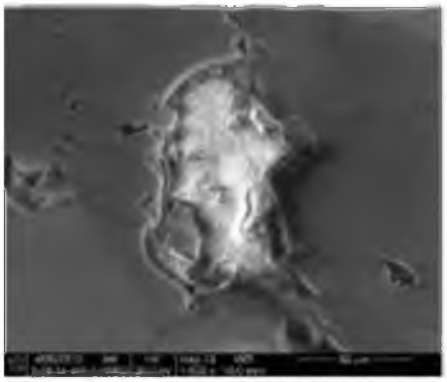

Vermillion EXP 5806-2P 17275

Vermillion EXP 5806-2P 17278

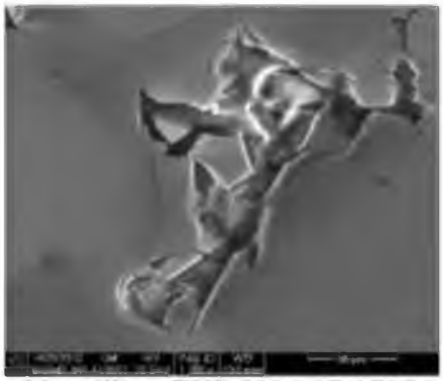

Vermillion EXP 5806-2P 17276

Vermillion EXP 5806-2P 1727

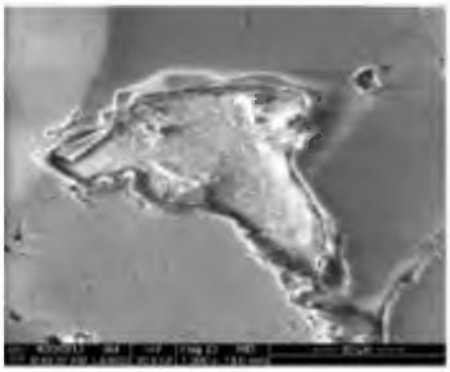

Vermillion EXP 5806-2P 17277

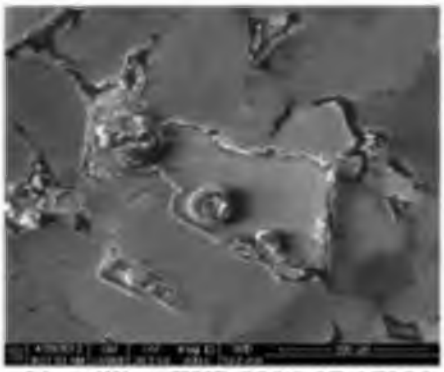

Vermillion EXP 5806-2P 17280

Figure 14. Continued

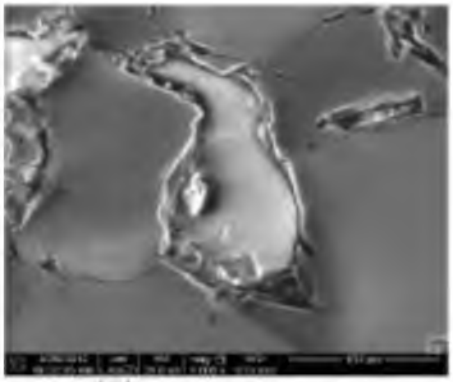
Vermillion EXP 5806-2P 17281

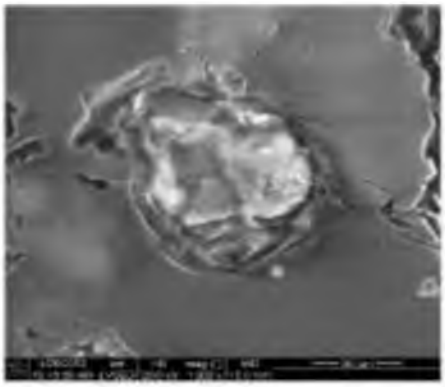
Vermillion EXP 5806-2P 17284

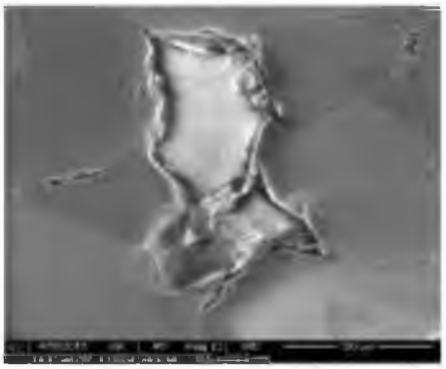
Vermillion EXP 5806-2P 17282

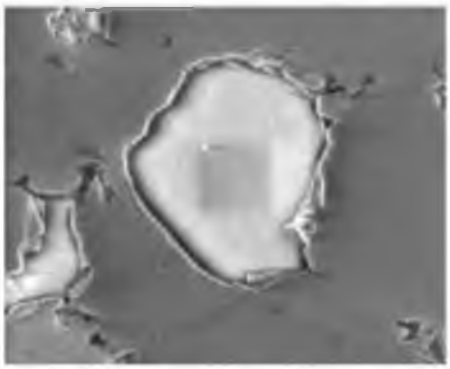
Vermillion EXP 5806-2P 17285

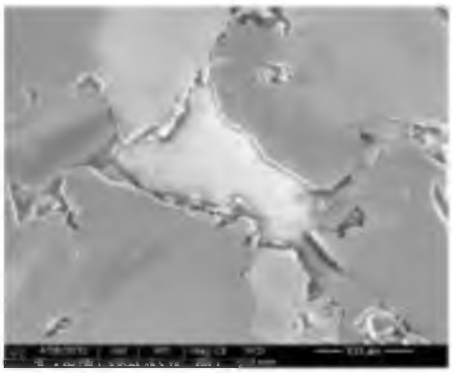
Vermillion EXP 5806-2P 17283

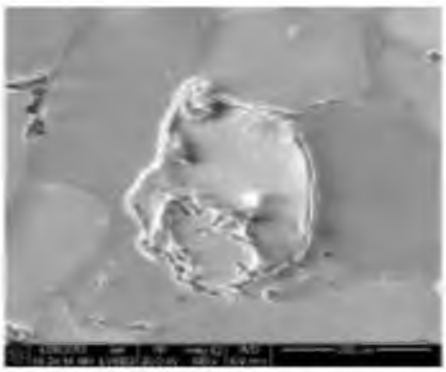
Vermillion EXP 5806-2P 17286

Figure 14. Continued

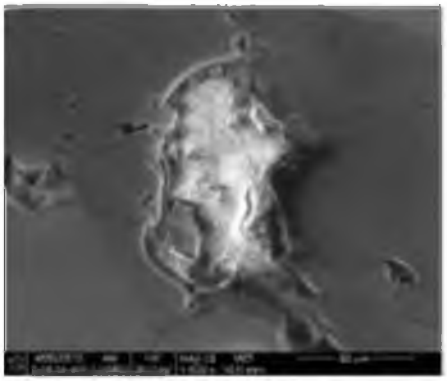

Vermillion EXP 5806-2P 17275

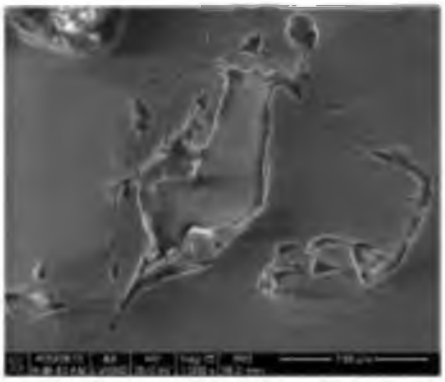

Vermillion EXP 5806-2P 17278

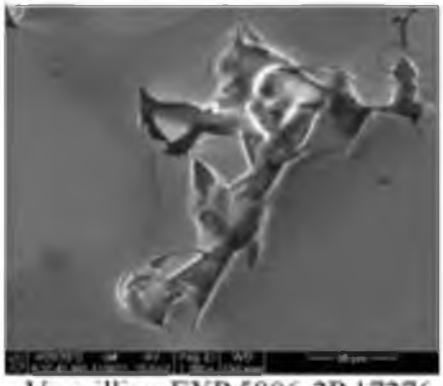

Vermillion EXP 5806-2P 17276

Vermillion EXP 5806-2P 1727

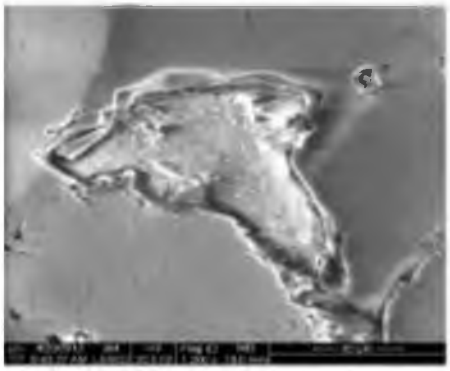

Vermillion EXP 5806-2P 17277

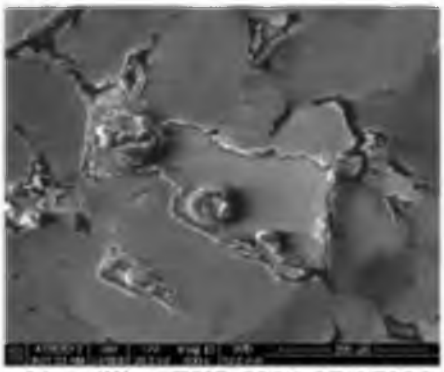

Vermillion EXP 5806-2P 17280

Figure 14. Continued

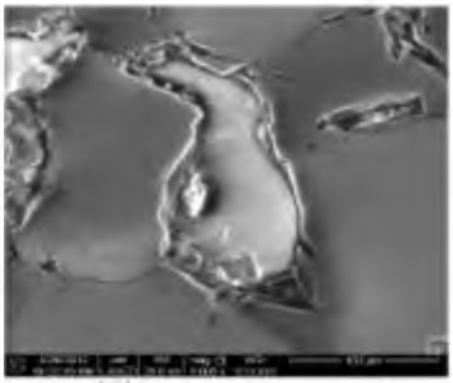

Vermillion EXP 5806-2P 17281

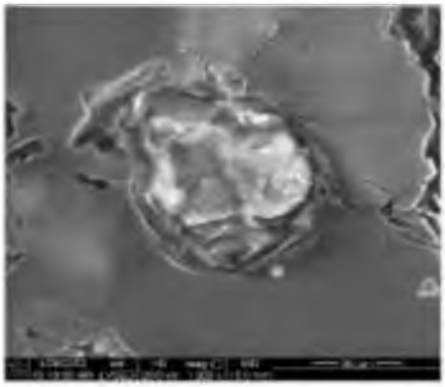

Vermillion EXP 5806-2P 17284

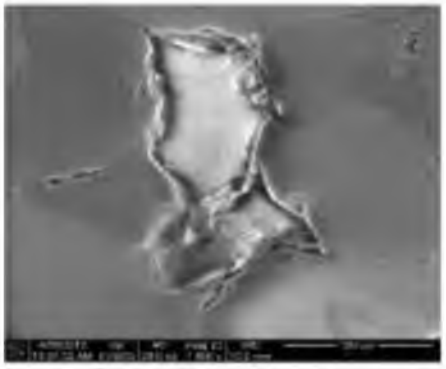

Vermillion EXP 5806-2P 17282

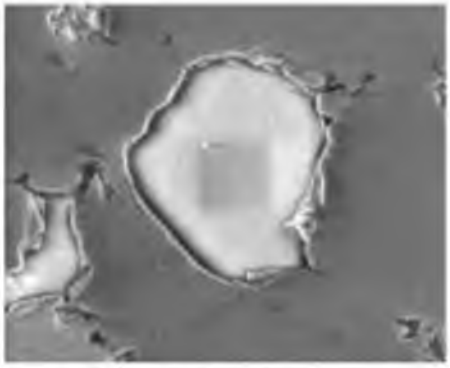

Vermillion EXP 5806-2P 17285

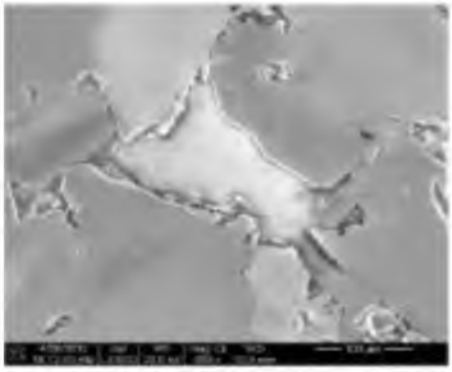

Vermillion EXP 5806-2P 17283

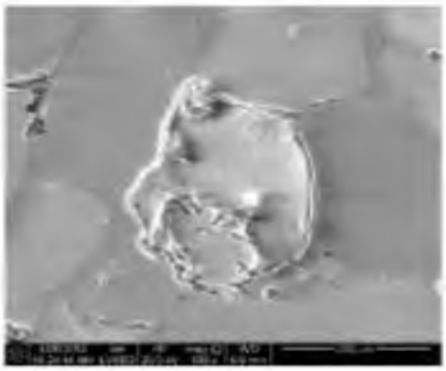

Vermillion EXP 5806-2P 17286

Figure 14. Continued

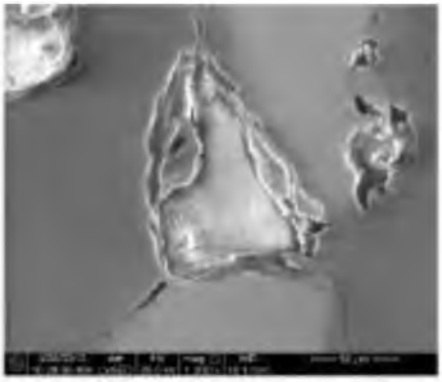

Vermillion EXP 5806-2P 17287

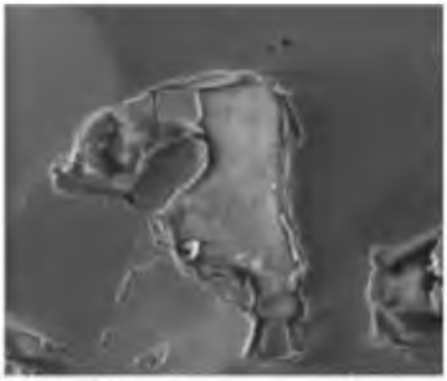

Vermillion EXP 5806-2P 17290

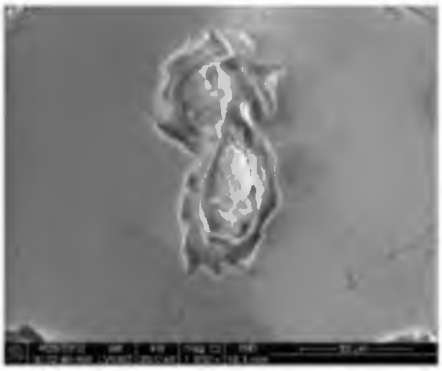

Vermillion EXP 5806-2P 17288

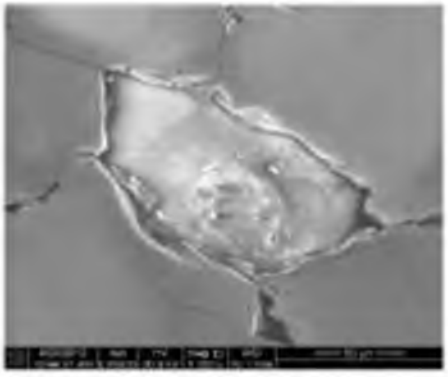

Vermillion EXP 5806-2P 17291

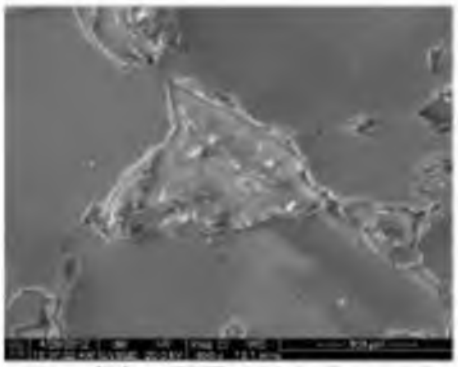

Vermillion EXP 5806-2P 17289

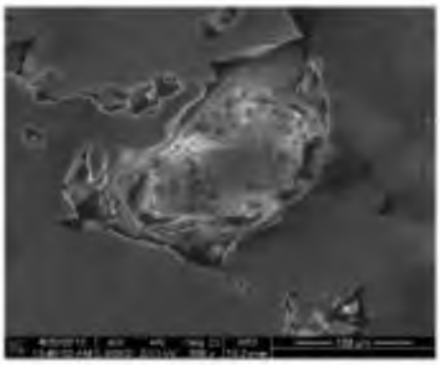

Vermillion EXP 5806-2P 17294

Figure 14. Continued

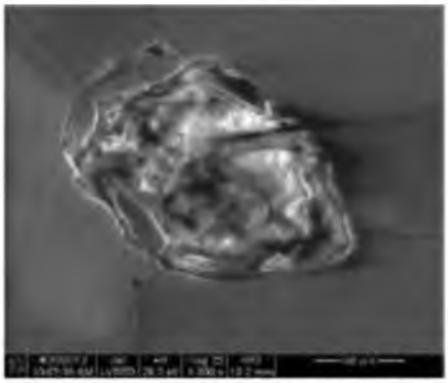

Vermillion EXP 5806-2P 17297

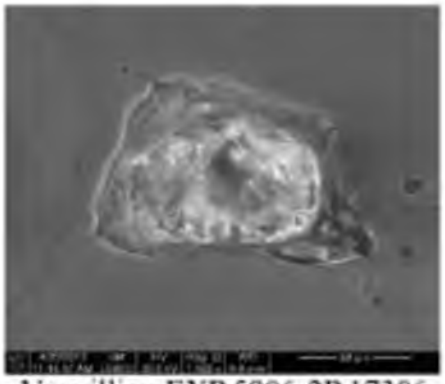

Vermillion EXP 5806-2P 17306

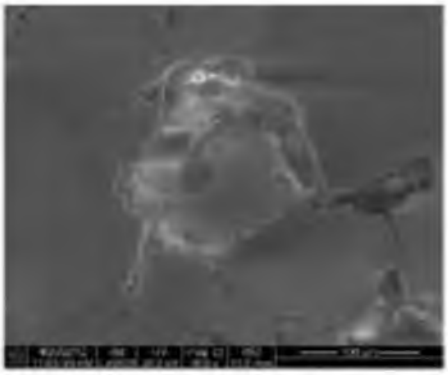

Vermillion EXP 5806-2P 17300

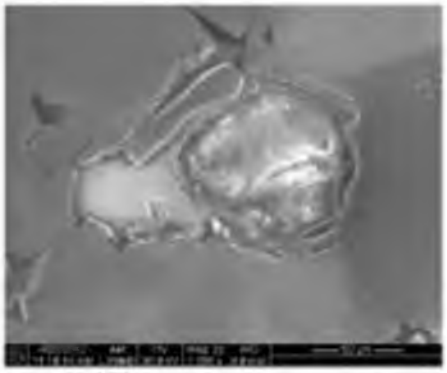

Vermillion EXP 5806-2P 17309

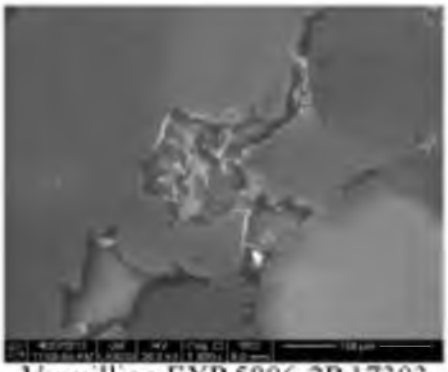

Vermillion EXP 5806-2P 17303

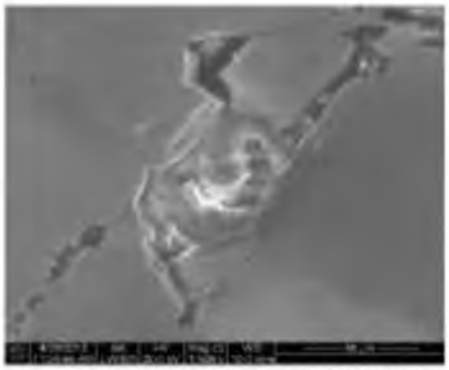

Vermillion EXP 5806-2P 17312

Figure 14. Continued

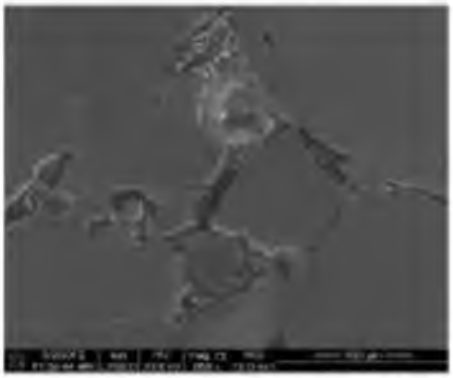

Vermillion EXP 5806-3P 14672

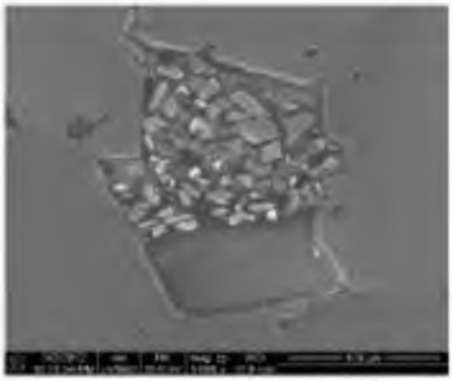

Vermillion EXP 5806-3P 14675

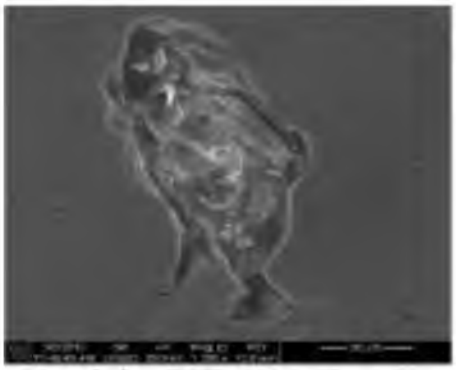

Vermillion EXP 5806-3P 14673

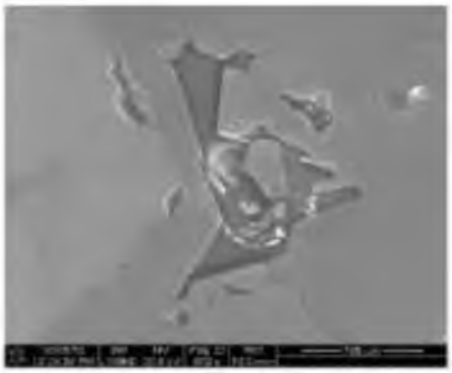

Vermillion EXP 5806-3P 14676

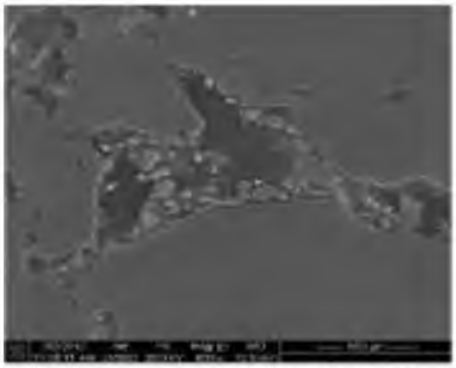

Vermillion EXP 5806-3P 14674

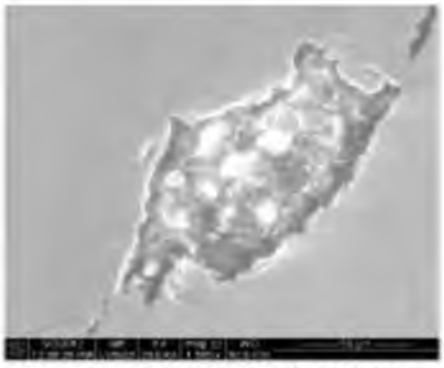

Vermillion EXP 5806-3P 17024

Figure 14. Continued

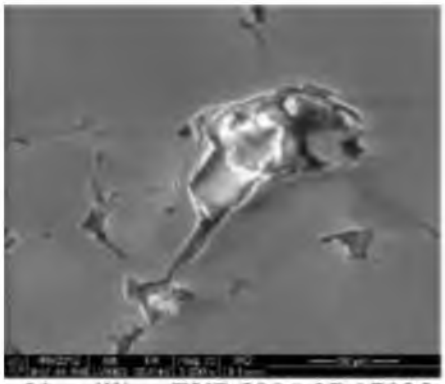

Vermillion EXP 5806-3P 17025

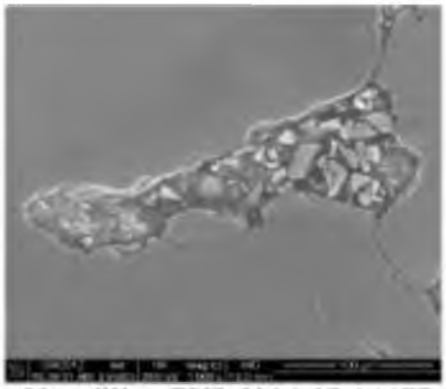

Vermillion EXP 5806-3P 14677

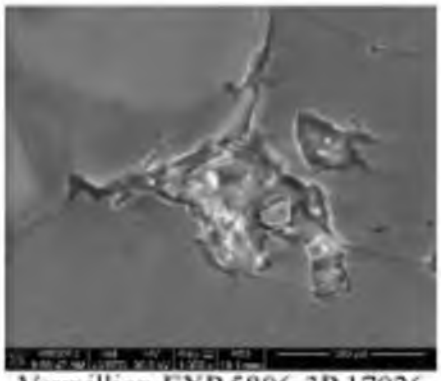

Vermillion EXP 5806-3P 17026

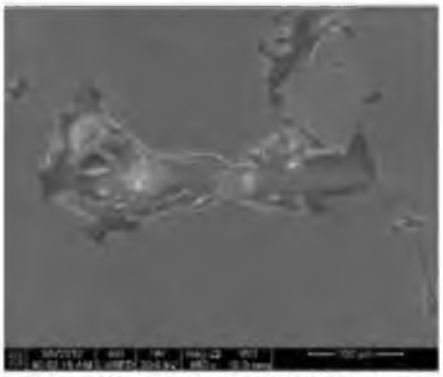

Vermillion EXP 5806-3P 14678

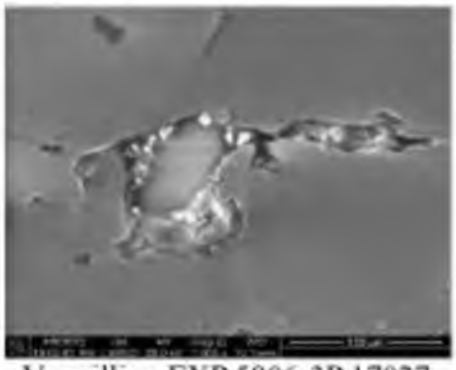

Vermillion EXP 5806-3P 17027

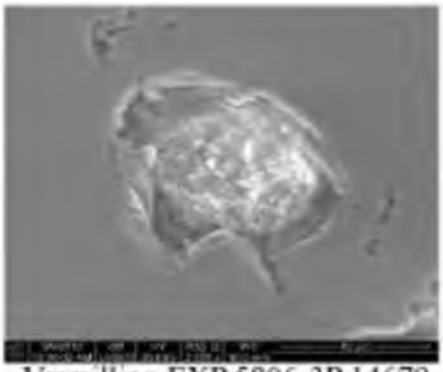

Vermillion EXP 5806-3P 14679

Figure 14. Continued

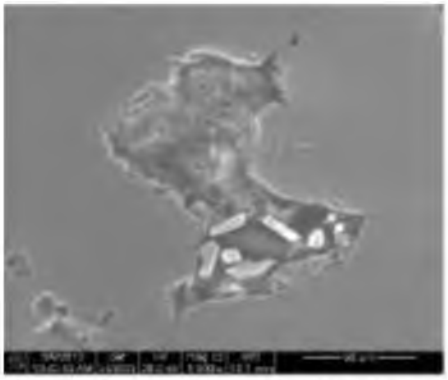

Vermillion EXP 5806-3P 14680

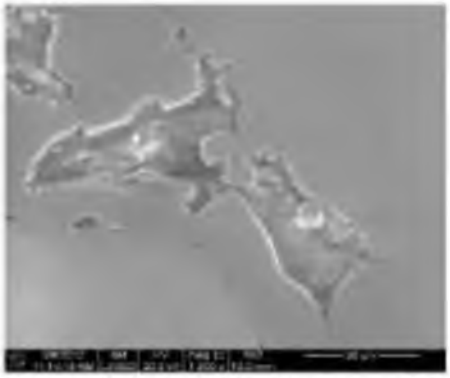

Vermillion EXP 5806-3P 14683

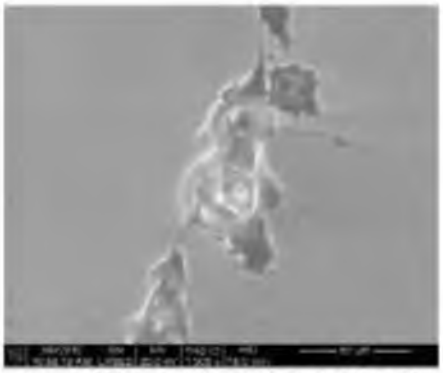

Vermillion EXP 5806-3P 14681

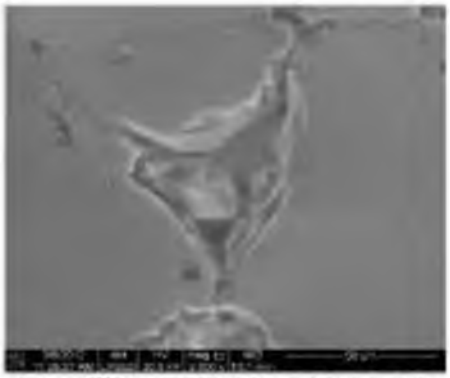

Vermillion EXP 5806-3P 14684

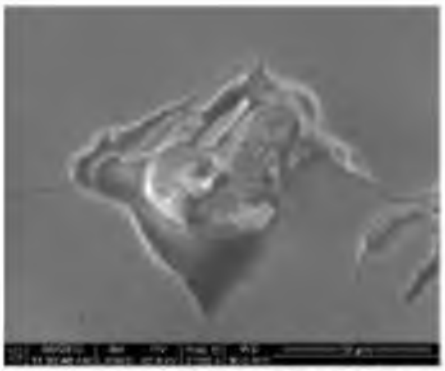

Vermillion EXP 5806-3P 14682

Vermillion EXP 5806-3P 14568

Figure 14. Continued

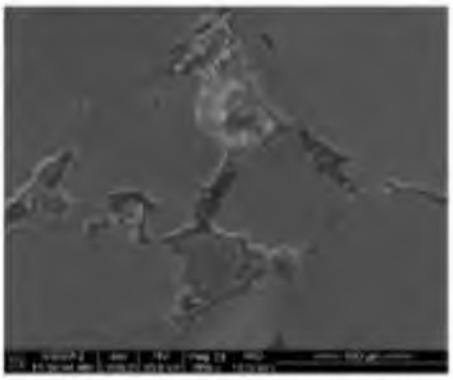

Vermillion EXP 5806-3P 14571

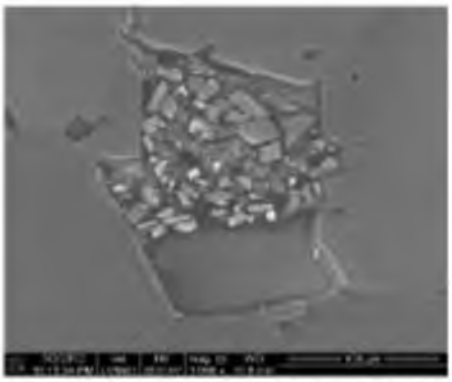

Vermillion EXP 5806-3P 14580

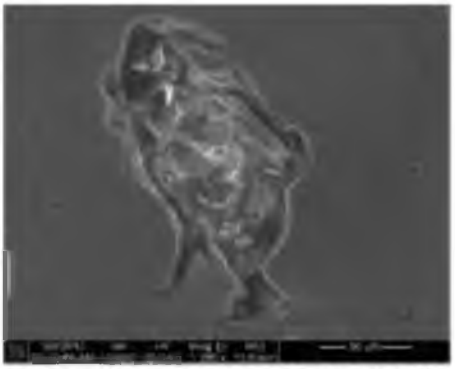

Vermillion EXP 5806-3P 14574

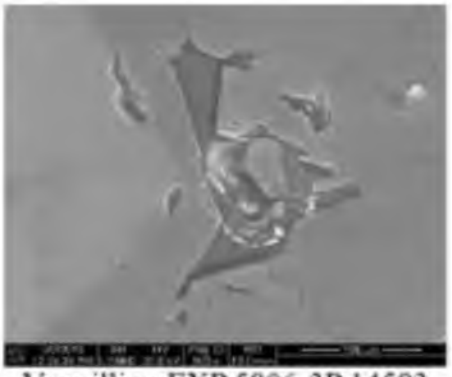

Vermillion EXP 5806-3P 14583

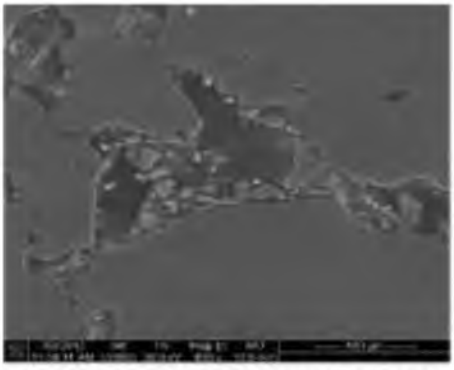

Vermillion EXP 5806-3P 14577

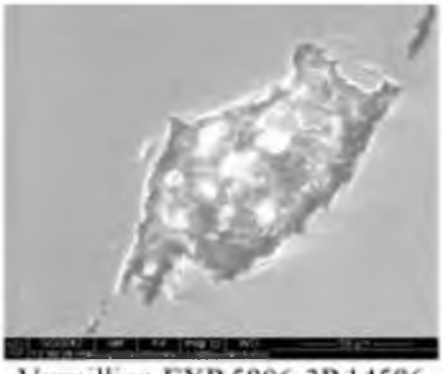

Vermillion EXP 5806-3P 14586

Figure 14. Continued

APPENDIX B

POINT COUNT RESULTS

Table 12. Vermillion 5805 2EE-013 Point Count Results

Grain #	Magnification	Long Axis	Short Axis	Composition	Roundness
1	10	8	7	q	R
2	10	11	7	q	R
3	10	20	6	q	A
4	10	5	3	q	SA
5	40	35	20	f5	SA
6	10	17	14	q	SR
7	40	40	35	f	VA
8	10	13	12	q	SR
9	10	27	10	f	A
10	40	60	50	q	SA
11	40	23	20	q	SA
12	40	65	30	f	SR
13	40	70	27	q	A
14	40	40	30	q	SR
15	40	55	43	q	SA
16	10	20	20	q	R
17	40	65	20	q	A
18	40	55	32	q	A
19	40	110	60	q	SA
20	10	12	8	q	SA
21	10	18	15	q	SA
22	40	40	30	q	SR
23	40	45	40	q	SR
24	40	70	35	q	SR
25	40	60	25	q	SR
26	40	65	55	q	R
27	40	30	20	q	VA
28	40	45	30	q	R
29	40	35	17	q	SA
30	40	35	20	q	SA
31	10	18	15	f	SA
32	40	45	37	q	SR
33	40	35	30	q	R
34	40	35	41	q	SA
35	40	45	25	q	A
36	40	35	18	q	SR
37	40	75	35	q	SA

Table 12. Continued

Grain #	Magnification	Long Axis	Short Axis	Composition	Roundness
38	40	45	43	q	R
39	40	50	42	q	SR
40	40	65	35	f	SA
41	40	60	15	q	SA
42	40	55	52	q	R
43	40	55	50	q	R
44	40	50	32	q	VA
45	40	45	40	f5	VA
46	40	60	18	q	VA
47	10	45	17	f5	A
48	10	25	15	q	R
49	10	55	50	q	VR
50	40	55	47	q	SA
51	40	35	33	f	A
52	10	18	14	q	SA
53	40	23	18	q	SA
54	40	74	54	q	A
55	40	49	46	q	A
56	10	16	13	f	SA
57	40	65	35	f	A
58	40	60	45	f	SA
59	40	75	55	q	SA
60	40	45	22	q	SR
61	40	64	40	q	SA
62	40	44	20	f	SR
63	40	25	22	q	A
64	40	20	48	q	SR
65	40	43	37	q	SA
66	10	30	25	q	SA
67	40	80	25	q5	SA
68	40	30	50	f	SR
69	40	60	20	f5	A
70	40	55	45	q	SA
71	40	85	47	f	SA
72	40	85	57	f	SR
73	40	65	43	q	SA
74	40	60	50	q	SR

Table 12. Continued

Grain #	Magnification	Long Axis	Short Axis	Composition	Roundness
75	40	12	11	l	SR
76	40	75	40	f	A
77	40	65	35	q	R
78	40	65	40	q	R
79	40	35	40	q	A
80	40	55	17	q	A
81	40	90	40	f	A
82	40	60	50	f	SR
83	40	80	45	q	SR
84	40	70	70	f	A
85	40	45	40	q	SR
86	40	45	20	q	SR
87	40	45	40	q	R
88	40	55	45	f	R
89	40	40	40	q	SR
90	40	50	15	q	SR
91	10	30	70	q	R
92	40	20	45	f5	SR
93	40	45	14	q	R
94	40	70	35	q	SA
95	40	80	7	f	SR
96	10	55	25	f	SA
97	40	75	65	q	SA
98	40	70	35	q	SR
99	10	10	7	q	SA
100	40	40	25	q	S
101	40	80	65	q	R
102	40	110	35	f	A
103	40	35	20	q	SA
104	40	25	20	q5	R
105	40	50	35	q	A
106	40	15	7	q	R
107	10	45	40	q	SR
108	40	15	12	q	SR
109	40	25	50	q	SA
110	40	60	30	q	VR
111	40	90	60	q	ST

Table 12. Continued

Grain #	Magnification	Long Axis	Short Axis	Composition	Roundness
112	40	105	20	q	SR
113	40	60	50	q	VR
114	40	80	80	q	SA
115	40	50	75	f	SA
116	40	60	40	f	SR
117	40	40	40	q	SA
118	40	80	18	q	A
119	40	65	20	q	A
120	40	40	20	q	R
121	40	20	35	q	VA
122	40	7	15	q5	VA
123	10	8	3	f	VR
124	40	50	6	q1	SR
125	40	65	30	q	SA
126	40	25	28	q	R
127	40	125	25	f	VR
128	40	125	40	q	SA
129	40	40	20	q	SR
130	40	75	75	q	A
131	40	50	25	q	SA
132	40	50	25	q	A
133	40	55	35	f	SA
134	40	70	20	q	R
135	40	75	25	q	SR
136	40	50	45	q	SR
137	40	105	55	q	A
138	40	40	25	q	SR
139	40	60	45	f	R
140	40	40	32	q	SR
141	40	60	30	q	A
142	10	40	35	q	SR
143	40	90	30	f	A
144	40	25	20	l	R
145	40	65	40	q	SR
146	40	70	60	q	R
147	40	80	20	q5	R
148	40	50	35	q	SA
149	40	50	30	q	SR

Table 12. Continued

Grain #	Magnification	Long Axis	Short Axis	Composition	Roundness
150	40	80	35	q	SR
151	40	50	45	f	R
152	40	90	40	f5	SA
153	40	50	30	l	A
154	10	15	5	q	SR
155	10	15	5	q	SR
156	10	25	15	q	SA
157	40	75	40	fq	A
158	40	20	5	f5	VA
159	10	40	20	q	VA
160	10	12	7	q	SR
161	40	65	40	q	SR
162	40	50	35	q	SR
163	40	75	60	f	SR
164	40	70	65	q5	SA
165	40	95	30	q	SR
166	40	70	40	q	SA
167	40	30	25	f	R
168	40	20	10	q	VA
169	40	2	10	l	VA
170	40	45	30	f	SA
171	40	65	35	q	R
172	40	55	45	q	R
173	40	50	35	q	SA
174	40	35	25	f	SA
175	40	45	45	q	R
176	40	80	55	q	SR
177	40	20	10	q	R
178	40	80	40	q	R
179	40	40	30	q	SA
180	40	70	35	q	SR
181	40	40	5	l	R
182	40	35	25	q	S
183	40	65	35	q	R
184	40	50	25	q	R
185	40	100	65	f	SR
186	40	120	75	f	SA

Table 12. Continued

Grain #	Magnification	Long Axis	Short Axis	Composition	Roundness
187	10	70	15	f	SR
188	40	60	45	f	R
189	40	20	12	q	R
190	40	15	5	q	R
191	40	40	40	q	SA
192	40	85	60	f	R
193	10	50	50	q	A
194	10	20	10	f	SR
195	10	30	15	q	R
196	10	60	60	q	A
197	10	40	20	q	R
198	10	35	30	q	SR
199	10	40	20	q	R
200	40	40	35	f	R
201	40			q	SR
202	40			f	VA
203	40			q	SR
204	40			f	A
205	40			q	SR
206	40			q	R
207	40			q	SA
208	40			q	S
209	40			q	SA
210	40			q	R
211	10			q	R
212	40			q	R
213	40			q5	A
214	40			f	SA
215	40			q	SA
216	40			q	SR
217	40			f	SA
218	40			q	VR
219	40			q	SR
220	40			f	A
221	40			f	SR
222	40			q	VA
223	40			f5	R

Table 12. Continued

Grain #	Magnification	Long Axis	Short Axis	Composition	Roundness
224	40			q	SR
225	40			q	SR
226	40			q	R
227	40			q	R
228	40			q	SR
229	40			f	SR
230	40			q	R
231	40			q	S
232	40			q	SR
233	40			q	SR
234	40			q	VR
235	40			q	SR
236	40			q	SA
237	40			q	SA
238	40			f	A
239	40			q	SR
240	40			q	VA
241	40			q	SR
242	40			q	SA
243	40			f	SA
244	40			q	SA
245	40			q	A
246	40			f	VR
247	40			q	SA
248	40			q	SA
249	40			q	A
250	40			q	S
251	10			q	SR
252	10			q	SR
253	40			q	SA
254	40			q	SA
255	40			q	A
256	40			q5	SA
257	40			q	R
258	40			f	A
259	40			q	SR
260	40			q	R

Table 12. Continued

Grain #	Magnification	Long Axis	Short Axis	Composition	Roundness
261	40			q	R
262	40			q	SA
263	40			f	A
264	40			q	R
265	40			q	VR
266	40			q	SR
267	40			q5	SA
268	40			q	VA
269	40			q	SR
270	40			q	R
271	40			q	R
272	40			q	A
273	40			q	SR
274	40			q	S
275	40			q	SR
276	40			q	R
277	40			q	R
278	40			q	SA
279	40			q	SR
280	40			q	SR
281	40			q	R
282	40			q	SR
283	40			q	A
284	40			q	R
285	10			l	A
286	10			q	S
287	10			q5	A
288	10			q	R
289	10			q	R
290	40			q	S
291	40			q	R
292	40			q	R
293	40			q	R
294	40			q	SA
295	40			q	SR
296	40			q	SR
297	40			q	SR

Table 12. Continued

Grain #	Magnification	Long Axis	Short Axis	Composition	Roundness
298	40			q	VA
299	40			q	SR
300	40			q	VR
301	40			q5	SA
302	40			q	S
303	40			q	SR
304	40			q	SR
305	40			f	SA
306	40			q	VR
307	10			q	R
308	10			q	SR
309	10			q	SR
310	10			q	SR
311	10			q	SR
312	40			q	VA
313	40			q	SR
314	40			f	R
315	40			q	A
316	40			f	A
317	40			q	R
318	40			f	SR
319	40			q	SA
320	10			q	R
321	40			q	SA
322	40			q	SA
323	40			f	SR
324	40			q	SA
325	40			q	SR
326	40			q	SR
327	40			q	SR
328	40			q5	SR
329	40			q1	R
330	40			f	SR
331	40			q	SA
332	40			q	R
333	10			q	SA
334	10			f	SA

Table 12. Continued

Grain #	Magnification	Long Axis	Short Axis	Composition	Roundness
335	10			q	SR
336	10			q	SA
337	10			q	A
338	10			q	R
339	40			q	SR
340	40			q1	SA
341	10			f	VA
342	10			q	R
343	10			q	R
344	10			q	SR
345	10			q	SR
346	10			q	R
347	10			q	SA
348	10			q	SR
349	10			q	SR
350	10			q	SR
351	10			q	SR
352	10			l	A
353	10			q	S
354	10			f	A
355	10			f5	SA
356	10			f	R
357	10			f	A
358	10			q	VR
359	10			q	SR
360	10			q	SA
361	10			q	V
362	10			q	SR
363	10			q	R
364	10			q	R
365	10			q	S
366	10			q	SR
367	10			q	S
368	10			q	SR
369	10			f	VA
370	10			q	R
371	10			f	VA

Table 12. Continued

Grain #	Magnification	Long Axis	Short Axis	Composition	Roundness
372	10			q1	VR
373	10			q	R
374	10			q	R
375	10			q	R
376	10			q	VA
377	10			q	VR
378	10			q	SA
379	10			q5	R
380	10			q	R
381	10			q	R
382	10			f	SA
383	10			q	R
384	10			q	S
385	10			q	A
386	10			q	R
387	10			q	SR
388	10			q	R
389	10			q	SR
390	10			q	R
391	10			f	VA
392	10			q	SR
393	10			q	SA
394	10			q	SA
395	10			q	VR
396	10			q	SR
397	10			q5	R
398	10			q	SR
399	10			q	VR
400	10			l	VA
401	10			q	VR
402	10			q	VA
403	10			q	SA
404	10			q	SR
405	10			q	SA
406	10			f5	SA
407	10			f	A
408	10			q	SR

Table 12. Continued

Grain #	Magnification	Long Axis	Short Axis	Composition	Roundness
409	10			q	SR
410	10			q	R
411	10			q	SR
412	10			q	R
413	10			q	R
414	10			q	R
415	10			q	VR
416	10			q	R
417	10			q	R
418	10			q	SR
419	10			q	SA
420	10			q	SR
421	10			q	SR
422	10			q	SR
423	10			q	SR
424	10			q	R
425	10			q	VA
426	10			Q5	VA
427	10			q	SA
428	10			q	SR
429	10			q	SA
430	10			q	R
431	10			q	SR
432	10			f	A
433	10			q	SR
434	10			q	SA
435	10			f	R
436	10			q	VA
437	10			q	R
438	10			q	SR
439	10			q	SR
440	10			q	SR
441	10			q	R
442	10			q	SR
443	10			q	VA
444	10			l	VA
445	10			q	SA

Table 12. Continued

Grain #	Magnification	Long Axis	Short Axis	Composition	Roundness
446	10			q	SA
447	10			q	R
448	10			q	SR
449	10			q	R
450	10			q	R
451	10			f	SA
452	10			q	SA
453	10			q	SA
454	10			f5	A
455	10			q	SR
456	10			f	SA
457	10			q	R
458	10			q	VR
459	10			f	VR
460	10			q	A
461	10			q	R
462	10			q	V
463	10			f5	A
464	10			q	SR
465	10			q	R
466	10			q	SR
467	10			q	SR
468	10			q	SA
469	10			q	SA
470	10			q	SR
471	10			q	A
472	10			q	R
473	10			q	SA
474	10			q	SA
475	10			q	R
476	10			f	A
477	10			l	R
478	10			l	A
479	10			q	R
480	10			q	R
481	10			q	SR
482	10			q	SA

Table 12. Continued

Grain #	Magnification	Long Axis	Short Axis	Composition	Roundness
483	10			q	SR
484	10			q	R
485	10			q	SA
486	10			q	A
487	10			q	S
488	10			q	SR
489	10			q	R
490	10			q	VA
491	10			q	A
492	10			q	SR
493	10			f	SA
494	10			q	SR
495	10			q	R
496	10			q	R
497	10			q	S
498	10			q	SA
499	10			q	R
500	10			q	R

Table 13. Vermillion 5806 2EE-014 Point Count Results

Grain	Magnification	Long Axis	Short Axis	Composition	Roundness
1	10	30	30		Q
2	10	15	10		Q
3	10	30	20		P
4	10	15	15		Q
5	10	40	30		Q
6	10	5	5		Q
7	10	25	20		Q
8	10	15	10		Q
9	10	35	25		Q
10	10	30	20		Q
11	10	20	15		Q
12	10	10	10		F
13	10	40	40		P
14	10	40	20		Q
15	10	25	20		Q
16	10	20	15		F
17	10	30	20		Q
18	10	20	15		Q
19	10	10	10		P
20	10	20	10		Q
21	10	10	10		Q
22	10	30	20		Q
23	10	10	10		P
24	10	20	20		Q
25	10	20	20		Q
26	10	15	10		Q
27	10	30	20		Q
28	10	40	20		Q
29	10	15	10		P
30	10	30	20		Q
31	10	30	10		P
32	10	20	20		Q
33	10	10	10		Q
34	10	10	5		Q
35	10	15	15		P
36	10	20	20		Q
37	10	15	5		Q

Table 13. Continued

Grain	Magnification	Long Axis	Short Axis	Composition	Roundness
38	10	30	30		Q
39	10	25	20		F
40	10	20	10		P
41	10	10	10		P
42	10	10	10		P
43	10	15	10		P
44	10	20	15		Q
45	10	30	15		Q
46	10	20	10		F
47	10	25	20		Q
48	10	20	15		Q
49	10	20	15		Q
50	10	10	10		Q
51	10	30	25		Q
52	10	20	10		Q
53	10	40	25		Q
54	10	30	20		P
55	10	20	10		F
56	10	40	30		Q
57	10	30	30		Q
58	10	30	20		Q
59	10	20	20		P
60	10	5	5		P
61	10	20	5		P
62	10	20	10		Q
63	10	20	20		Q
64	10	40	30		Q
65	10	20	20		Q
66	10	25	15		Q
67	10	25	20		Q
68	10	10	5		P
69	10	25	15		Q
70	10	20	20		Q
71	10	30	30		Q
72	10	30	20		P
73	10	10	10		P
74	10	20	10		Q

Table 13. Continued

Grain	Magnification	Long Axis	Short Axis	Composition	Roundness
75	10	40		40	Q
76	10	10		10	P
77	10	20		10	F
78	10	30		20	Q
79	10	25		20	Q
80	10	30		30	Q
81	10	20		20	Q
82	10	20		20	Q
83	10	25		20	Q
84	10	20		15	Q
85	10	30		30	F
86	10	15		15	P
87	10	10		5	P
88	10	15		10	Q
89	10	20		10	Q
90	10	30		20	Q
91	10	20		10	Q
92	10	40		40	Q
93	10	20		10	F
94	10	25		20	Q
95	10	25		15	Q
96	10	10		5	P
97	10	15		10	Q
98	10	15		15	Q
99	10	5		5	P
100	10	20		5	P
101	10	15		5	P
102	10	10		5	P
103	10	20		10	Q
104	10	15		10	Q
105	10	30		25	Q
106	10	10		10	P
107	10	25		20	Q
108	10	15		10	P
109	10	10		10	P
110	10	30		20	Q
111	10	20		20	Q

Table 13. Continued

Grain	Magnification	Long Axis	Short Axis	Composition	Roundness
112	10	35	20		Q
113	10	25	20		Q
114	10	20	20		Q
115	10	20	20		Q
116	10	20	20		F
117	10	40	40		Q
118	10	30	20		Q
119	10	20	20		Q
120	10	5	5		P
121	10	35	25		Q
122	10	20	20		Q
123	10	20	10		P
124	10	20	20		Q
125	10	10	5		P
126	10	20	10		P
127	10	10	10		L
128	10	30	20		Q
129	10	20	20		Q
130	10	60	50		Q
131	10	20	10		P
132	10	25	25		Q
133	10	20	20		P
134	10	10	10		Q
135	10	20	15		Q
136	10	25	20		Q
137	10	30	20		Q
138	10	40	30		Q
139	10	20	15		Q
140	10	30	20		Q
141	10	10	10		Q
142	10	20	20		Q
143	10	15	10		Q
144	10	20	20		Q
145	10	25	10		Q
146	10	20	20		Q
147	10	30	20		Q
148	10	30	30		Q

Table 13. Continued

Grain	Magnification	Long Axis	Short Axis	Composition	Roundness
149	10	40		40	Q
150	10	10		5	P
151	10	15		10	Q
152	10	30		20	Q
153	10	30		30	Q
154	10	20		20	Q
155	10	10		10	P
156	10	20		20	Q
157	10	25		15	Q
158	10	40		25	Q
159	10	30		30	Q
160	10	10		10	L
161	10	20		15	F
162	10	35		25	Q
163	10	25		20	Q
164	10	20		10	F
165	10	20		20	Q
166	10	20		20	Q
167	10	30		20	Q
168	10	35		10	Q
169	10	50		20	Q
170	10	30		20	Q
171	10	15		10	L
172	10	25		5	P
173	10	40		30	Q
174	10	20		10	Q
175	10	20		5	P
176	10	25		20	Q
177	10	25		25	F
178	10	20		10	P
179	10	40		30	Q
180	10	30		20	Q
181	10	60		40	Q
182	10	30		30	Q
183	10	20		15	Q
184	10	25		20	Q
185	10	20		15	Q
186	10	25		10	P

Table 13. Continued

Grain	Magnification	Long Axis	Short Axis	Composition	Roundness
187	10	55		40	Q
188	10	20		15	Q
189	10	55		40	Q
190	10	10		10	Q
191	10	15		5	Q
192	10	30		25	Q
193	10	20		10	P
194	10	25		10	Q
195	10	15		10	Q
196	10	20		10	Q
197	10	15		10	F
198	10	50		30	Q
199	10	25		20	Q
200	10	30		20	Q
201	10				Q
202	10				Q
203	10				Q
204	10				Q
205	10				F
206	10				Q
207	10				Q
208	10				Q
209	10				Q
210	10				P
211	10				Q
212	10				Q
213	10				Q
214	10				Q
215	10				Q
216	10				Q
217	10				Q
218	10				Q
219	10				P
220	10				P
221	10				P
222	10				Q
223	10				Q

Table 13. Continued

Grain	Magnification	Long Axis	Short Axis	Composition	Roundness
224	10				F
225	10				P
226	10				Q
227	10				Q
228	10				Q
229	10				Q
230	10				P
231	10				Q
232	10				P
233	10				Q
234	10				F
235	10				Q
236	10				Q
237	10				Q
238	10				Q
239	10				Q
240	10				Q
241	10				P
242	10				P
243	10				Q
244	10				Q
245	10				P
246	10				Q
247	10				P
248	10				Q
249	10				Q
250	10				Q
251	10				Q
252	10				F
253	10				Q
254	10				F
255	10				Q
256	10				Q
257	10				Q
258	10				Q
259	10				Q
260	10				Q

Table 13. Continued

Grain	Magnification	Long Axis	Short Axis	Composition	Roundness
261	10				F
262	10				F
263	10				Q
264	10				P
265	10				Q
266	10				Q
267	10				Q
268	10				P
269	10				Q
270	10				P
271	10				P
272	10				Q
273	10				Q
274	10				Q
275	10				Q
276	10				Q
277	10				Q
278	10				Q
279	10				P
280	10				Q
281	10				P
282	10				P
283	10				Q
284	10				Q
285	10				Q
286	10				Q
287	10				Q
288	10				F
289	10				Q
290	10				Q
291	10				Q
292	10				Q
293	10				Q
294	10				P
295	10				L
296	10				P
297	10				P

Table 13. Continued

Grain	Magnification	Long Axis	Short Axis	Composition	Roundness
298	10				Q
299	10				Q
300	10				Q
301	10				Q
302	10				P
303	10				Q
304	10				Q
305	10				Q
306	10				Q
307	10				Q
308	10				Q
309	10				Q
310	10				Q
311	10				Q
312	10				P
313	10				P
314	10				Q
315	10				Q
316	10				Q
317	10				Q
318	10				F
319	10				Q
320	10				Q
321	10				Q
322	10				Q
323	10				P
324	10				Q
325	10				Q
326	10				Q
327	10				P
328	10				F
329	10				Q
330	10				P
331	10				Q
332	10				Q
333	10				Q
334	10				Q

Table 13. Continued

Grain	Magnification	Long Axis	Short Axis	Composition	Roundness
335	10				P
336	10				Q
337	10				Q
338	10				Q
339	10				Q
340	10				Q
341	10				P
342	10				Q
343	10				Q
344	10				Q
345	10				Q
346	10				Q
347	10				Q
348	10				F
349	10				P
350	10				Q
351	10				F
352	10				Q
353	10				Q
354	10				Q
355	10				F
356	10				Q
357	10				Q
358	10				Q
359	10				F
360	10				Q
361	10				Q
362	10				Q
363	10				P
364	10				Q
365	10				Q
366	10				L
367	10				P
368	10				F
369	10				Q
370	10				Q
371	10				P

Table 13. Continued

Grain	Magnification	Long Axis	Short Axis	Composition	Roundness
372	10				Q
373	10				Q
374	10				Q
375	10				P
376	10				P
377	10				P
378	10				Q
379	10				Q
380	10				P
381	10				Q
382	10				Q
383	10				P
384	10				Q
385	10				P
386	10				F
387	10				F
388	10				P
389	10				Q
390	10				L
391	10				Q
392	10				Q
393	10				P
394	10				F
395	10				F
396	10				Q
397	10				Q
398	10				Q
399	10				P
400	10				Q
401	10				P
402	10				P
403	10				P
404	10				Q
405	10				Q
406	10				Q
407	10				Q
408	10				Q

Table 13. Continued

Grain	Magnification	Long Axis	Short Axis	Composition	Roundness
409	10				Q
410	10				P
411	10				Q
412	10				Q
413	10				Q
414	10				Q
415	10				Q
416	10				P
417	10				P
418	10				Q
419	10				P
420	10				Q
421	10				F
422	10				F
423	10				Q
424	10				Q
425	10				Q
426	10				P
427	10				P
428	10				P
429	10				P
430	10				Q
431	10				P
432	10				Q
433	10				Q
434	10				Q
435	10				Q
436	10				P
437	10				Q
438	10				P
439	10				Q
440	10				F
441	10				Q
442	10				Q
443	10				Q
444	10				Q
445	10				Q

Table 13. Continued

Grain	Magnification	Long Axis	Short Axis	Composition	Roundness
446	10				Q
447	10				F
448	10				Q
449	10				Q
450	10				Q
451	10				P
452	10				Q
453	10				F
454	10				Q
455	10				Q
456	10				Q
457	10				L
458	10				Q
459	10				F
460	10				Q
461	10				Q
462	10				Q
463	10				P
464	10				Q
465	10				Q
466	10				P
467	10				F
468	10				Q
469	10				Q
470	10				Q
471	10				Q
472	10				Q
473	10				Q
474	10				Q
475	10				P
476	10				Q
477	10				Q
478	10				Q
479	10				Q
480	10				Q
481	10				Q
482	10				Q

Table 13. Continued

Grain	Magnification	Long Axis	Short Axis	Composition	Roundness
483	10				F
484	10				Q
485	10				Q
486	10				Q
487	10				Q
488	10				Q
489	10				Q
490	10				Q
491	10				Q
492	10				P
493	10				Q
494	10				P
495	10				Q
496	10				Q
497	10				Q
498	10				F
499	10				Q
500	10				F

Table 14. Knox 8542 2EE-015 Point Count Results

Grain #	Magnification	Long Axis	Short Axis	Composition	Roundness
1	40	50	40	l	SA
2	40	65	55	q	SR
3	40	40	30	q	R
4	40	100	60	l	A
5	40	60	60	q	SR
6	40	30	25	q	R
7	40	15	5	f5	SA
8	40	20	10	q5	SR
9	40	60	35	q	SA
10	40	50	30	q	VA
11	40	80	20	f	A
12	40	25	25	l	VA
13	10	15	10	f	A
14	40	9	8	q	R
15	40	12	8	q5	SA
16	40	15	10	q	SA
17	40	130	30	q	A
18	40	65	55	q	VA
19	10	40	20	f	VA
20	10	10	15	q	R
21	10	30	20	q	SA
22	10	12	8	q	R
23	10	25	10	q	A
24	10	30	10	q	VA
25	10	110	20	f	VA
26	40	70	30	q	SA
27	40	80	50	q	VA
28	40	60	40	q	VA
29	40	30	25	q	SA
30	40	40	30	q	SA
31	40	50	30	q	R
32	40	55	40	f	SA
33	40	50	50	q	R
34	40	25	10	q	R
35	40	45	35	q	SR

Table 14. Continued

Grain #	Magnification	Long Axis	Short Axis	Composition	Roundness
36	40	20	10	q5	SR
37	40	65	25	Q5	SR
38	40	60	30	q5	R
39	40	30	10	f5	SA
40	40	55	55	f	R
41	40	10	10	q	R
42	40	60	40	q	A
43	40	45	35	q	SR
44	40	50	30	f	SA
45	40	45	20	q	R
46	40	50	40	f	SR
47	40	20	20	f5	R
48	40	20	5	q	R
49	40	30	20	q	R
50	40	75	35	q	SA
51	40	100	30	q	SR
52	40	25	15	l	A
53	40	150	35	f	VA
54	40	60	60	q	A
55	40	50	15	q	SA
56	40	60	50	q	R
57	40	50	30	q	SA
58	40	20	10	f	A
59	40	110	100	f	R
60	40	70	50	f	SA
61	40	50	50	q	SA
62	40	80	25	l	SR
63	40	20	5	f5	A
64	40	25	5	q	A
65	40	50	40	q	SR
66	40	20	15	f	R
67	40	30	25	f	A
68	40	85	25	q1	A
69	40	90	30	f	SA

Table 14. Continued

Grain #	Magnification	Long Axis	Short Axis	Composition	Roundness
70	40	25	25	f	A
71	40	30	30	q5	R
72	40	20	10	q	A
73	40	40	30	q	SR
74	40	60	20	q5	A
75	40	12	10	f5	VA
76	40	15	5	q	A
77	40	50	25	q	SR
78	40	80	20	f	A
79	40	70	25	f	A
80	40	70	30	f	A
81	40	80	20	q	SA
82	40	40	25	q	A
83	40	40	30	f	A
84	40	70	10	f	SR
85	40	30	20	f	SA
86	40	45	35	q	SR
87	40	70	40	f	VA
88	40	90	40	q	SA
89	40	50	30	q	SR
90	40	70	18	f	SR
91	40	60	40	q	R
92	40	45	35	f	SA
93	40	35	35	f5	VA
94	40	120	60	f	SR
95	40	55	45	q	SA
96	40	25	25	q	SR
97	40	70	50	q	SA
98	40	50	10	q5	A
99	40	50	35	q	R
100	40	60	30	q	SR
101	40	100	40	f	A
102	40	5	5	q5	A
103	40	50	40	q	SR
104	40	25	20	l	A

Table 14. Continued

Grain #	Magnification	Long Axis	Short Axis	Composition	Roundness
105	40	20	10	q5	SA
106	40	50	30	q1	R
107	40	40	40	q	A
108	40	30	20	f	SA
109	40	40	30	q	SA
110	40	100	70	f	SR
111	40	25	20	q	SA
112	40	20	10	f	A
113	40	5	5	q5	A
114	40	30	30	q	SR
115	40	30	25	q	R
116	40	60	30	f	A
117	40	30	20	l	A
118	40	40	40	q	SR
119	40	60	25	q	A
120	40	45	25	q	A
121	40	75	35	f	SA
122	40	20	20	q	R
123	40	50	40	q	R
124	40	55	50	q	R
125	40	60	50	q	R
126	40	60	40	q	R
127	40	70	25	f	A
128	10	50	50	f	A
129	10	10	10	q	R
130	10	15	10	q	SR
131	10	20	15	f	A
132	10	15	12	f5	SA
133	10	20	10	q	A
134	10	40	40	f	R
135	10	20	20	f	R
136	10	25	15	f	R
137	10	15	10	q	A
138	10	10	5	q	A
139	40	20	20	q	A

Table 14. Continued

Grain #	Magnification	Long Axis	Short Axis	Composition	Roundness
140	40	50	40	q	SA
141	40	40	40	q	VA
142	40	20	10	q	SR
143	40	35	20	q	A
144	40	50	30	q	SA
145	40	10	10	q5	A
146	40	50	40	q	A
147	40	40	10	q	SA
148	40	30	25	f	R
149	40	50	35	q	SA
150	40	70	40	f	SR
151	40	100	50	q1	A
152	40	110	70	q	A
153	40	60	35	q	SA
154	40	75	60	q	SA
155	40	110	30	q	A
156	40	70	50	q	A
157	40	80	40	l	SA
158	40	70	50	q	SR
159	40	80	20	q	A
160	40	70	30	f	A
161	40	50	40	q	SA
162	40	70	30	q	R
163	40	50	45	q1	R
164	40	20	15	q	SR
165	40	30	15	q	SA
166	40	80	60	l	R
167	40	60	40	q	SR
168	40	70	60	q	A
169	40	80	60	f	VA
170	40	50	30	f	SA
171	40	70	100	f	SA
172	10	20	15	q	SA
173	40	10	5	q5	R
174	40	20	5	f5	A

Table 14. Continued

Grain #	Magnification	Long Axis	Short Axis	Composition	Roundness
175	40	80	40	q	SA
176	40	50	30	q	SR
177	40	50	30	q	A
178	40	60	30	q	SA
179	40	40	20	q1	SR
180	40	40	30	q1	VR
181	40	100	60	q	VA
182	40	50	10	q	SR
183	40	60	20	q	SA
184	40	70	50	q	SA
185	40	40	30	q	R
186	40	40	40	f	R
187	40	90	70	q	R
188	40	90	50	q	R
189	40	30	20	q1	VA
190	40	15	10	f	A
191	40	60	50	q	SR
192	40	60	40	q	SA
193	40	50	30	f	SR
194	40	50	20	q	SA
195	40	50	40	q	R
196	40	50	50	f	R
197	40	100	80	f	A
198	40	50	30	q	R
199	40	80	80	f	SR
200	40	90	30	q	A
201	40			q	A
202	40			q	A
203	40			q	R
204	40			q	R
205	40			q	R
206	40			f	VA
207	40			q	SR
208	40			f	SA
209	40			q	SR

Table 14. Continued

Grain #	Magnification	Long Axis	Short Axis	Composition	Roundness
210	40			q	SA
211	40			q	SR
212	40			q	SA
213	40			q	A
214	40			q	SR
215	40			q	R
216	40			q	SR
217	40			q	R
218	40			q	SA
219	40			q	SA
220	40			q	R
221	40			q	SA
222	40			q5	A
223	40			q	SR
224	40			q	SR
225	40			f	SA
226	40			f	SR
227	40			q	SR
228	40			q	SR
229	40			q	SA
230	40			q	A
231	40			q	A
232	40			q5	A
233	40			q	A
234	40			f	VA
235	40			q	SR
236	40			q5	SA
237	40			q	SR
238	40			q5	SR
239	40			q	R
240	40			q	SR
241	40			f	SA
242	40			q	SR
243	40			f	SA
244	40			q	SR

Table 14. Continued

Grain #	Magnification	Long Axis	Short Axis	Composition	Roundness
245	40			q	SA
246	40			q	VR
247	40			f	SA
248	40			q	SA
249	40			f	SR
250	40			q	R
251	40			q	SA
252	40			f	R
253	40			q	SR
254	40			q	R
255	40			f	A
256	40			f	A
257	40			f	SA
258	40			f	R
259	40			l	R
260	40			q	A
261	40			q	SA
262	40			f5	A
263	40			q	R
264	40			f5	A
265	40			q5	A
266	40			q	R
267	40			q	SA
268	40			q5	A
269	40			q	SA
270	40			q	R
271	40			q	VR
272	40			f	SR
273	40			f	SR
274	40			f	A
275	40			f	A
276	40			q5	A
277	40			q	R
278	40			q	SA
279	40			q5	SR

Table 14. Continued

Grain #	Magnification	Long Axis	Short Axis	Composition	Roundness
280	40			q5	A
281	40			q	R
282	40			f	SR
283	40			q5	SA
284	40			f5	A
285	40			f	SA
286	40			q	R
287	40			f	SR
288	40			f	SA
289	40			q	SR
290	40			q	SR
291	40			q	R
292	40			f	A
293	40			f	A
294	40			q	SR
295	40			q	SR
296	40			f	SR
297	40			f	SR
298	40			f5	SA
299	40			f	SR
300	40			q5	A
301	40			f	SR
302	40			q	R
303	40			q	SA
304	40			q1	R
305	40			l	SA
306	40			q	SR
307	40			q	R
308	40			q	A
309	40			q	SA
310	40			q	SA
311	40			q1	R
312	40			q	SA
313	40			f	R

Table 14. Continued

Grain #	Magnification	Long Axis	Short Axis	Composition	Roundness
314	40			q	SR
315	40			q	R
316	40			q	R
317	40			q	A
318	40			f	A
319	40			f	A
320	40			f	SA
321	40			q	VR
322	40			q	VR
323	40			q	SA
324	40			q	A
325	40			q	R
326	40			q	SR
327	40			f	SR
328	40			q	SR
329	40			l	SA
330	40			q	A
331	40			q	SA
332	40			q	A
333	40			q	R
334	40			q	SR
335	40			q	SA
336	40			q	SR
337	40			q	SR
338	40			q	R
339	40			q	VR
340	40			q	SR
341	40			f	VA
342	40			q	SR
343	40			q	SR
344	40			f	SA
345	40			q	R
346	40			q	R
347	40			q	SR
348	40			q	SR

Table 14. Continued

Grain #	Magnification	Long Axis	Short Axis	Composition	Roundness
349	40			q	SA
350	40			q	SR
351	40			q	SA
352	40			q	A
353	40			q	SR
354	40			f	SR
355	40			l	A
356	40			f	SA
357	40			q	R
358	40			q	VR
359	40			q	SR
360	40			q	SA
361	40			q	VA
362	40			q5	A
363	40			q	R
364	40			q	R
365	40			q	SR
366	40			q	R
367	40			q	SA
368	40			l	VR
369	40			f	SR
370	40			f	SR
371	40			q	R
372	40			q	VA
373	40			q	R
374	40			q	VR
375	40			f	SR
376	40			q	SA
377	40			q	SA
378	40			q	A
379	40			f	SR
380	40			q	SR
381	40			f5	SA
382	40			q	R
383	40			q	SA
384	40			q	SR
385	40			q	R

Table 14. Continued

Grain #	Magnification	Long Axis	Short Axis	Composition	Roundness
386	40			q	VR
387	40			q	SA
388	40			q	R
389	40			q	R
390	40			q	SA
391	40			q	SR
392	40			f	SR
393	40			l	A
394	40			f	VA
395	40			f	SR
396	40			q	SR
397	40			q	VA
398	40			f	SR
399	40			f	SR
400	40			q5	VA
401	40			q	SA
402	40			q	VR
403	40			q	R
404	40			q	R
405	40			q	VA
406	40			q	SR
407	40			q1	VR
408	40			f	SA
409	40			q	SR
410	40			q	SA
411	40			f	R
412	40			q5	R
413	40			f	SA
414	40			q	SR
415	40			q	R
416	40			q	SA
417	40			q	A
418	40			f	R
419	40			f	R
420	40			q	VA
421	40			q	VA
422	40			l	SA

Table 14. Continued

Grain #	Magnification	Long Axis	Short Axis	Composition	Roundness
423	40			q	SR
424	40			q	SR
425	40			q	A
426	40			q	A
427	40			q	SR
428	40			q	R
429	40			q5	SR
430	40			q	R
431	40			q	R
432	40			q	SR
433	40			q	SR
434	40			f	SR
435	40			q	VR
436	40			f	SA
437	40			q	A
438	40			q	SR
439	40			f	SR
440	40			f5	R
441	40			f5	R
442	40			f	SR
443	40			q	R
444	40			q	A
445	40			q	R
446	40			q	SA
447	40			q	R
448	40			q	SR
449	40			q	SA
450	40			q	R
451	40			q	SA
452	40			q5	A
453	40			q	A
454	40			q	R
455	40			f	A
456	40			q	SA
457	40			q5	A
458	40			q	R

Table 14. Continued

Grain #	Magnification	Long Axis	Short Axis	Composition	Roundness
459	40			q	SR
460	40			q	SA
461	40			q	VA
462	40			f	R
463	40			q	VA
464	40			q	A
465	40			q	SA
466	40			q	VA
467	40			q	VR
468	40			q	SA
469	40			q	VA
470	40			q	VR
471	40			q	SA
472	40			f	VA
473	40			f	VA
474	40			q	VA
475	40			f	SR
476	40			f	SR
477	40			f	SR
478	40			f	SA
479	40			q	A
480	40			f	SR
481	40			f	SR
482	40			f	R
483	40			q5	SR
484	40			q5	SR
485	40			q	R
486	40			q	SR
487	40			q	R
488	40			q	R
489	40			q	A
490	40			q	VR
491	40			l	R
492	40			q	R
493	40			f	R
494	40			f	SR

Table 14. Continued

Grain #	Magnification	Long Axis	Short Axis	Composition	Roundness
495	40			q	VA
496	40			q	SA
497	40			q	SA
498	40			f	VA
499	40			f	SA
500	40			q	VA

Table 15. Knox 8642 2EE-016 Point Count Results

Grain #	Magnification	Long Axis	Short Axis	Composition	Roundness
1	40	80	70	q	SA
2	40	10	5	q	R
3	40	80	60	f	R
4	40	70	60	q	A
5	40	70	65	q	R
6	40	40	40	f	VR
7	10	25	20	q	R
8	10	35	25	q	VA
9	40	60	25	q	SA
10	40	40	30	q	SR
11	40	60	30	q	R
12	40	70	40	q	SR
13	40	60	20	f	R
14	40	25	10	q	SR
15	40	50	20	q	SR
16	40	25	20	q	R
17	40	70	50	q	V
18	40	60	50	q	SR
19	40	70	60	q	VA
20	40	70	5	q	R
21	40	80	65	q	S
22	40	60	40	q	SR
23	40	60	50	q	SA
24	40	80	40	q	SR
25	40	40	40	q	VR
26	40	50	30	q	S
27	40	10	50	q	SR
28	10	45	20	q	SR
29	10	30	20	f	SR
30	10	25	15	q	SR
31	10	15	15	q	R
32	40	70	50	f	SR
33	40	40	30	f	A
34	40	60	30	q	SR
35	40	40	20	q	R
36	40	80	30	q	SR
37	40	50	50	q	VR

Table 15. Continued

Grain #	Magnification	Long Axis	Short Axis	Composition	Roundness
38	40	85	50	q	SR
39	40	70	50	q	VA
40	40	70	40	f	A
41	40	100	90	q	SR
42	40	50	50	q	R
43	40	70	50	q	SR
44	40	100	50	q	SA
45	40	30	5	q	A
46	40	70	50	q	R
47	40	80	60	f	A
48	40	40	40	q	R
49	40	70	50	q	VR
50	40	60	40	q	A
51	40	75	60	q	SA
52	40	60	50	f	SR
53	40	50	50	q	A
54	40	80	80	q	R
55	40	100	80	q	SR
56	40	40	15	f	SR
57	10	20	20	f	VR
58	40	60	20	f	SR
59	40	90	20	q	SR
60	40	30	30	f	R
61	40	80	40	q	A
62	40	55	50	q	VA
63	40	4	10	f	SR
64	40	50	30	f	R
65	10	30	20	q	SR
66	10	25	25	q	R
67	10	70	20	q	SR
68	10	5	5	q	A
69	10	20	10	q	SA
70	10	80	30	q	VA
71	40	60	60	q	R
72	40	60	55	q	SR
73	40	120	90	q	A
74	40	60	30	q	SA
75	10	20	15	q	R
76	10	15	15	q	SR

Table 15. Continued

Grain #	Magnification	Long Axis	Short Axis	Composition	Roundness
77	10	30	20	q	R
78	10	35	5	q	SA
79	10	25	20	q	R
80	10	70	40	q	VA
81	10	10	5	q	A
82	10	25	25	q	SR
83	40	60	30	q	SR
84	40	90	50	q	SA
85	10	12	10	q	SR
86	10	30	20	q	SR
87	40	40	40	f	R
88	40	40	40	q	VR
89	40	60	60	q	R
90	40	80	65	q	SR
91	40	100	60	q	SR
92	10	35	25	f	SA
93	10	25	20	q	SR
94	10	40	30	q	SA
95	40	55	45	q	SR
96	40	90	60	q	VA
97	40	80	40	q	SR
98	40	70	60	q	R
99	40	70	70	q	R
100	40	25	20	f	A
101	40	70	60	q	R
102	40	60	50	q	SR
103	40	80	70	f	SR
104	40	50	50	q	VR
105	40	60	60	q	A
106	40	80	65	q	SR
107	40	100	70	q	SA
108	40	70	50	q	R
109	40	100	85	q	SR
110	40	70	50	q	SA
111	40	50	50	q	SA
112	40	70	30	q	VA
113	40	40	60	q	SA

Table 15. Continued

Grain #	Magnification	Long Axis	Short Axis	Composition	Roundness
114	40	90	50	f	SA
115	40	100	40	f	SA
116	10	15	10	q	VA
117	10	45	30	q	SR
118	10	20	15	q	SA
119	10	15	10	q	R
120	10	20	15	q	SR
121	10	25	25	f	R
122	10	5	5	f	VA
123	40	20	15	q	VA
124	40	80	15	q	SR
125	10	40	15	f	SA
126	10	35	20	q	SR
127	10	15	10	q	R
128	10	18	15	q	SA
129	10	15	12	q	SR
130	10	30	15	f	SR
131	10	10	7	q	SA
132	10	20	15	q	SA
133	10	12	8	f	SA
134	40	35	30	q	SR
135	40	60	40	q	VR
136	40	40	20	q	SR
137	40	30	10	q	R
138	40	120	80	q	SA
139	40	80	40	f	SR
140	40	70	60	f	A
141	40	65	55	q	SR
142	40	90	40	q	VA
143	40	70	50	q	A
144	40	70	60	q	SA
145	40	70	40	q	VA
146	40	100	90	q	A
147	40	75	45	q	SA
148	40	70	60	q	S
149	40	70	55	q	SR
150	40	60	45	f	SR

Table 15. Continued

Grain #	Magnification	Long Axis	Short Axis	Composition	Roundness
151	40	50	50	q	SR
152	40	80	45	q	R
153	40	65	60	q	VA
154	40	60	55	q	SR
155	40	30	45	f	VR
156	40	55	45	q	SR
157	40	80	60	q	R
158	40	100	45	q	SA
159	40	100	70	q	SA
160	40	80	40	q	A
161	40	60	50	f	R
162	40	50	40	q	R
163	40	70	40	q	A
164	10	20	15	q	R
165	10	70	50	q	SR
166	40	50	40	l	VR
167	40	60	40	q	SR
168	40	40	20	q	S
169	40	40	20	q	SR
170	40	90	30	q	SA
171	40	80	40	q	R
172	40	70	30	q	SR
173	40	60	20	q	SA
174	40	70	50	q	R
175	40	60	50	q	SR
176	40	50	30	q	R
177	10	40	25	f	SA
178	40	50	45	q	SR
179	40	40	30	q	SA
180	40	75	70	q	A
181	40	70	40	q	VR
182	40	70	50	q	R
183	40	60	50	q	SR
184	40	70	55	q	R
185	40	50	30	q	SR
186	40	70	30	f	SR
187	40	70	50	q	SR

Table 15. Continued

Grain #	Magnification	Long Axis	Short Axis	Composition	Roundness
188	10	20	10	f	SR
189	40	100	70	q	SA
190	40	80	40	q	A
191	40	60	50	q	R
192	40	40	30	q	SR
193	40	110	5	q	R
194	40	60	20	q	A
195	40	100	40	q	SR
196	40	70	30	q	SA
197	40	100	60	f	SR
198	40	60	60	f	R
199	40	70	60	q	R
200	10	30	20	q	R
201	40			q	SR
202	40			f	R
203	40			q	S
204	40			q	SR
205	40			q	SR
206	40			q	SA
207	40			f	SR
208	40			q	SA
209	40			q	SR
210	40			q	SR
211	40			q	SR
212	40			q	R
213	40			q	SA
214	40			q	A
215	40			q	SA
216	40			f	SR
217	40			q	R
218	40			q	R
219	40			q	SR
220	40			q	SR
221	40			q	A
222	40			f	R
223	40			f	SA
224	40			f	A

Table 15. Continued

Grain #	Magnification	Long Axis	Short Axis	Composition	Roundness
225	40			q	A
226	40			q	SR
227	40			q	SR
228	40			q	SA
229	40			q	R
230	40			q	SR
231	40			f	SR
232	40			q	SR
233	40			f	A
234	10			l	SR
235	10			f	SA
236	10			q	SR
237	10			q	SR
238	10			q	A
239	10			q	SR
240	10			q	SR
241	10			f	SR
242	10			q	R
243	10			q	A
244	10			f	SA
245	10			q	R
246	10			f	SA
247	10			q	A
248	10			f	SA
249	10			f	SA
250	10			q	SR
251	10			q	SR
252	10			q	VR
253	10			q	A
254	10			q	SA
255	10			q	R
256	10			q	SR
257	10			q	SA
258	10			q	R
259	10			q	S
260	10			q	SA
261	10			q	A

Table 15. Continued

Grain #	Magnification	Long Axis	Short Axis	Composition	Roundness
262	10			q	R
263	10			q	VA
264	10			q	A
265	10			q	SA
266	10			f	A
267	10			q	R
268	10			q	SA
269	10			q	R
270	10			q	SR
271	10			f	SR
272	10			q	SA
273	10			q	VR
274	10			q	VA
275	10			q	S
276	10			q	SR
277	10			q	SR
278	10			q	V
279	10			q	SR
280	10			q	R
281	10			q	R
282	10			q	SA
283	10			q	R
284	10			q	VA
285	10			f	SR
286	10			l	SR
287	10			q	SA
288	10			q	A
289	10			q	R
290	10			q	SA
291	10			f	SR
292	10			q	SR
293	10			q	VA
294	10			f	VA
295	10			f	VA
296	10			f	R
297	10			q	SR
298	10			q	R

Table 15. Continued

Grain #	Magnification	Long Axis	Short Axis	Composition	Roundness
299	10			q	R
300	10			q	SA
301	10			q	SA
302	10			q	VR
303	10			q	A
304	10			q	A
305	10			q	R
306	10			q	SA
307	10			q	SR
308	10			q	A
309	10			q	A
310	10			q	SA
311	10			f	SR
312	10			q	R
313	10			q	R
314	10			q	R
315	10			q	R
316	10			f	SA
317	10			q	A
318	10			q	R
319	10			q	SA
320	10			q	R
321	10			f	SR
322	10			f	SR
323	10			q	SR
324	10			l	SR
325	10			f	A
326	10			q	R
327	10			q	SA
328	10			f	SA
329	10			l	R
330	10			q	SA
331	10			f	SA
332	10			q	A
333	10			q	A
334	10			q	SR
335	10			q	SA

Table 15. Continued

Grain #	Magnification	Long Axis	Short Axis	Composition	Roundness
336	10			q	SR
337	10			q	R
338	10			q	SA
339	10			q	R
340	10			f	SR
341	10			q	SR
342	10			q	SR
343	10			q	A
344	10			q	SR
345	10			f	A
346	10			f	A
347	10			q	R
348	10			q	R
349	10			q	R
350	10			q	R
351	10			q	SR
352	10			q	SA
353	10			q	SA
354	10			q	SA
355	10			q	A
356	10			q	SR
357	10			q	SR
358	10			q	R
359	10			q	SA
360	10			f	SA
361	10			q	R
362	10			q	A
363	10			q	SA
364	10			q	SR
365	10			q	A
366	10			q	VR
367	10			q	A
368	10			q	SA
369	10			q	SA
370	10			q	R
371	10			q	S
372	10			q	SR

Table 15. Continued

Grain #	Magnification	Long Axis	Short Axis	Composition	Roundness
373	10			q	S
374	10			q	SR
375	10			q	S
376	10			f	R
377	10			q	SR
378	10			q	R
379	10			q	SA
380	10			q	R
381	10			f	A
382	10			f	A
383	10			q	VR
384	10			q	VR
385	10			q	SR
386	10			q	SR
387	10			q	SR
388	10			q	SA
389	10			q	SR
390	10			q	SA
391	10			q	SR
392	10			q	A
393	10			q	SR
394	10			q	SR
395	10			q	VR
396	10			q	SA
397	10			q	VA
398	10			q	VA
399	10			q	SR
400	10			q	SR
401	10			f	R
402	10			q	SA
403	10			q	SR
404	10			q	VA
405	10			f	VA
406	10			q	VA
407	10			q	SR
408	10			q	SR
409	10			f	SA

Table 15. Continued

Grain #	Magnification	Long Axis	Short Axis	Composition	Roundness
410	10			f	VR
411	10			f	VA
412	10			f	VA
413	10			q	SR
414	10			q	SA
415	10			q	VR
416	10			q	VR
417	10			q	SR
418	10			q	SA
419	10			l	SR
420	10			q	R
421	10			q	R
422	10			f	SA
423	10			f	R
424	10			q	VA
425	10			q	R
426	10			q	R
427	10			q	SA
428	10			q	A
429	10			q	A
430	10			q	SR
431	10			q	SA
432	10			q	SR
433	10			q	VA
434	10			q	A
435	10			q	SR
436	10			q	SR
437	10			q	SR
438	10			q	R
439	10			q	SA
440	10			q	R
441	10			q	A
442	10			q	SA
443	10			f	A
444	10			q	A
445	10			q	SA
446	10			l	SR

Table 15. Continued

Grain #	Magnification	Long Axis	Short Axis	Composition	Roundness
447	10			q	SR
448	10			q	R
449	10			q	SR
450	10			q	SR
451	10			q	R
452	10			f	A
453	10			q	S
454	10			f	SR
455	10			q	SR
456	10			f	SA
457	10			q	SR
458	10			q	SR
459	10			l	R
460	10			q	S
461	10			q	R
462	10			f	SR
463	10			q	S
464	10			q	SA
465	10			q	R
466	10			q	SR
467	10			q	R
468	10			q	SR
469	10			q	SR
470	10			q	SR
471	10			q	SA
472	10			q	A
473	10			q	A
474	10			q	SR
475	10			f	SR
476	10			f	SR
477	10			q	A
478	10			q	R
479	10			q	A
480	10			q	S
481	10			q	VR
482	10			q	A
483	10			q	SA

Table 15. Continued

Grain #	Magnification	Long Axis	Short Axis	Composition	Roundness
484	10			q	A
485	10			q	SR
486	10			q	R
487	10			f	SA
488	10			q	SA
489	10			q	SA
490	10			q	A
491	10			q	R
492	10			q	SR
493	10			q	SR
494	10			q	A
495	10			q	SR
496	10			f	R
497	10			l	R
498	10			l	VA
499	10			f	R
500	10			q	SA

REFERENCES

Bachu, S., 2003, Screening and ranking of sedimentary basins for sequestration of CO2 in geological media in response to climate change: Environmental Geology, v. 44, p. 277–289, doi: 10.1007/s00254-003-0762-9.

Bachu, S., and Adams, J.J., 1999, Geological Sequestration of Anthropogenic Carbon Dioxide in the Western Canada Sedimentary Basin: Suitability Analysis:, p. 1–23.

Balashov, V.N., Guthrie, G.D., Hakala, J.A., Lopano, C.L., Rimstidt, J.D., and Brantley, S.L., 2013, Predictive modeling of CO2 sequestration in deep saline sandstone reservoirs: Impacts of geochemical kinetics: Applied Geochemistry, v. 30, p. 41–56, doi: 10.1016/j.apgeochem.2012.08.016.

Barnes, D.A., Bacon, D.H., and Kelley, S.R., 2009, Geological sequestration of carbon dioxide in the Cambrian Mount Simon Sandstone: Regional storage capacity, site characterization, and large-scale injection feasibility, Michigan Basin: Environmental Geosciences, v. 16, p. 163–183, doi: 10.1306/eg.05080909009.

Benson, S., and Cole, D., 2008, CO2 Sequestration in Deep Sedimentary Formations: Elements, v. 4, p. 325–331, doi: 10.2113/gselements.4.5.325.

Berger, P.M., Roy, W.R., and Mehnert, E., 2009, Energy Procedia: Energy Procedia, v. 1, p. 3437–3444, doi: 10.1016/j.egypro.2009.02.134.

Bethke, C., 2008, Geochemical and Biogeochemical Reaction Modeling: Cambridge University Press.

Boden, T.A., G. Marland, and R.J. Andres. 2012. Global, Regional, and National Fossil-Fuel CO_2 Emissions. Carbon Dioxide Information Analysis Center, Oak Ridge National Laboratory, U.S. Department of Energy, Oak Ridge, Tenn., U.S.A. doi 10.3334/CDIAC/00001_V2012

Bowen, B.B., Ochoa, R.I., Wilkens, N.D., Brophy, J., Lovell, T.R., Fischietto, N., Medina, C.R., and Rupp, J.A., 2011, Depositional and diagenetic variability within the Cambrian Mount Simon Sandstone: Implications for carbon dioxide sequestration: Environmental Geosciences, v. 18, p. 69–89, doi: 10.1306/eg.07271010012.

Braile, L.W., Keller, G.R., Hinze, W.J., and Lidak, E.G., 1982, Ancient Rift Complex and its Relation to Contemporary Seismicity in the New Madrid Seismic Zone Tectonics, v. 1, p. 1–13.

Chen, Z.S., Riciputi, L.R., Mora, C.I., and Fishman, N.S., 2001, Regional fluid migration in the Illinois Basin: Evidence from in situ oxygen isotope analysis of authigenic K-feldspar and quartz from the Mount Simon Sandstone: Geology, v. 29, p. 1067–1070, doi:10.1130/0091-7613(2001)029<1067:RFMITI> 2.0.CO;2.

Dennis R Kolata, W.J.N., 1991, Tectonic History of the Illinois Basin: Chapter 18: Part I. Illinois Basin: Evolution, *in* AAPG Memoir, p. 263–285.

Dethlefsen, F., Haase, C., Ebert, M., and Dahmke, A., 2011, Uncertainties of geochemical modeling during CO2 sequestration applying batch equilibrium calculations: Environmental Earth Sciences, v. 65, p. 1105–1117, doi: 10.1007/s12665-011-1360-x.

Drever, J.L., 1997, The Carbonate System and pH Control in the Geochemistry of Natural Waters: Surface and Groundwater Environments, Prentice Hall, p. 436.

Dyar, M.D., and Gunter, M.E., 2007, Mineralogy and Optical Mineralogy: Mineralogical Society of America.

Eliasson, B., Reimer, P., and Wokaun, A., 1988, Greenhouse Gas Control Technologies: Precedings of 4th Intl. Greenhouse Gas Control.

Finley, R.J., Greenberg, S.E., Frailey, S.M., Krapac, I.G., Leetaru, H.E., and Marsteller, S., 2011, The path to a successful one-million tonne demonstration of geological sequestration: Characterization, Cooperation, and Collaboration: Energy Procedia, v. 4, p. 4770–4776, doi: 10.1016/j.egypro.2011.02.441.

Fishman, N.S., 1997, Basin-wide fluid movement in a Cambrian paleoaquifer: Evidence from the Mount Simon Sandstone, Illinois and Indiana: Society for Sedimentary Geology (SEPM), p. 1–15.

Frailey, S. M., J. Damico, and H. E. Leetaru (2011), Reservoir characterization of the Mt. Simon Sandstone, Illinois Basin, USA, Energy Procedia, 4, 5487–5494, doi:10.1016/j.egypro.2011.02.534.

Goldstein, J., Newbury, D.E., and Joy, C.E., 2003, Scanning Electron Microscopy and X-ray Microanalysis : Springer.

Hagadorn, J., Dott, R., and Damrow, D., 2002, Stranded on a Late Cambrian shoreline: Medusae from central Wisconsin: Geology, v. 30, p. 147–150.

Heald, M. T. and R. E. Larese, 1973, The significance of the solution of feldspar in porosity development: Journal of Sedimentary Petrology, v. 43, p. 458-460.

Heidlauf, D.T., Hsui, A.T., and Klein, G., 1986, Tectonic Subsidence Analysis of the Illinois Basin: The Journal of Geology, v. 94, p. 1–17.

Hoholick, J.D., Metarko, T., and Potter, P.T., 1984, Regional Variations of Porosity and Cement; St. Peter and Mount Simon Sandstone: AAPG Bulletin, v. 68, p. 1–12.

Kaszuba, J.P., Janecky, D.R., and Snow, M.G., 2005, Experimental evaluation of mixed fluid reactions between supercritical carbon dioxide and NaCl brine: Relevance to the integrity of a geologic carbon repository: Chemical Geology, v. 217, p. 277–293, doi: 10.1016/j.chemgeo.2004.12.014.

Kaszuba, J.P., Janecky, D.R., and Snow, M.G., 2003, Experimental Evaluation of Mixed Fluid Reactions between Supercritical Carbon Dioxide and NaCl Brine:Relevance to the Integrity of a Geologic Carbon Repository: Chemical Geology,, p. 1–16.

Kharaka, J.L., 2004, A Compilation of Rate Parameters of Water-Mineral Interaction Kinetics for Application to Geochemical Modeling: US Geological Survey Report 2004-1068,, p. 1–70.

Knauss, K.G., Johnson, J.W., and Steefel, C.I., 2005, Evaluation of the impact of CO2, co-contaminant gas, aqueous fluid and reservoir rock interactions on the geologic sequestration of CO2: Chemical Geology, v. 217, p. 339–350, doi: 10.1016/j.chemgeo.2004.12.017.

Lasaga, A.C., 1981, Transition State Theory: Reviews in Mineralogy and Geochemistry, v. 8, p. 135–168.

Leetaru, H.E., and Mcbride, J.H., 2009, Reservoir uncertainty, Precambrian topography, and carbon sequestration in the Mt. Simon Sandstone, Illinois Basin: Environmental Geosciences, v. 16, p. 235–243, doi: 10.1306/eg.04210909006.

Liu, F., Lu, P., Zhu, C., and Xiao, Y., 2011, Coupled reactive flow and transport modeling of CO2 sequestration in the Mt. Simon sandstone formation, Midwest U.S.A.: International Journal of Greenhouse Gas Control, v. 5, p. 294–307, doi: 10.1016/j.ijggc.2010.08.008.

Liu, H., Hou, M.Z., Gou, Y., and Were, P., 2013, Simulation of CO2-Water-Rock Interaction Processes-Mineral Scaling Problems in Saline Formations, *in* Springer Series in Geomechanics and Geoengineering, Springer Series in Geomechanics and Geoengineering, Clean Energy Systems in the Subsurface, Berlin, Heidelberg, p. 233–248.

Lovell, T.R., and Bowen, B.B., 2013, Fluctuations in Sedimentary Provenance of the Upper Cambrian Mount Simon Sandstone, Illinois Basin, United States: The Journal of Geology, v. 121, p. 129–154, doi: 10.1086/669230.

Lu, P., Fu, Q., Seyfried, W.E., Hereford, A., and Zhu, C., 2010, Navajo Sandstone–brine–CO2 interaction: implications for geological carbon sequestration: Environmental Earth Sciences, v. 62, p. 101–118, doi: 10.1007/s12665-010-0501-y.

Macke, D. L., 1995, Illinois Basin Province (064), *in* Gautier, D. L., Dolton, G.L., Takahashi, K.I., and Varnes, K.L., ed., 1995 National assessment of United States oil and gas resources

Makowitz, A., Lander, R.H., and Milliken, K.L., 2006, Diagenetic modeling to assess the relative timing of quartz cementation and brittle grain processes during compaction: AAPG Bulletin, v. 90, p. 873–885, doi: 10.1306/12190505044.

Mcbride, J.H., 1989, Quartz Cement in Sandstones: A Review: Earth Science Reviews, v. 26, p. 69–112.

Michael E Duffin, M.L.G.D.K.R.L.H., 1989, Potassic Diagenesis Of Cambrian Sandstones and Precambrian Granitic Basement in UPH-3 Deep Hole, Upper Mississippi Valley, USA: Journal of Sedimentary Petrology, v. 59, p. 848–961

Milton T Heald, R.E.L., 1973, The Significance of the Solution of Feldspar in Porosity Development: Journal of Sedimentary Petrology, v. 43, p. 458–460.

Morad, S., Marfil, R., and La Pena, De, J.A., 1989, Diagenetic K-feldspar pseudomorphs in the Triassic Buntsandstein sandstones of the Iberian Range, Spain: Sedimentology, v. 36.

Muller, N., Qi, R., Mackie, E., Pruess, K., and Blunt, M.J., 2009, CO2 injection impairment due to halite precipitation: Energy Procedia, v. 1, p. 3507–3514, doi: 10.1016/j.egypro.2009.02.143.

Newell, D.L., Kaszuba, J.P., Viswanathan, H.S., Pawar, R.J., and Carpenter, T., 2008, Significance of carbonate buffers in natural waters reacting with supercritical CO 2: Implications for monitoring, measuring and verification (MMV) of geologic carbon sequestration: Geophysical Research Letters, v. 35, p. L23403, doi: 10.1029/2008GL035615.

Nondorf, L., Gutierrez, M., and Plymate, T.G., 2011, Modeling carbon sequestration geochemical reactions for a proposed site in Springfield, Missouri: Environmental Geosciences, v. 18, p. 91–99, doi: 10.1306/eg.09141010014.

Odom, I.E., 1975, Feldspar-Grain Size Relations in Cambrian Arenites, Upper Mississippi Valley: Journal of Sedimentary Petrology, v. 45, p. 1–15.

Parry, W.T., Forster, C.B., Evans, J.P., Bowen, B.B., and Chan, M.A., 2007, Geochemistry of CO2 sequestration in the Jurassic Navajo Sandstone, Colorado Plateau, Utah: Environmental Geosciences, v. 14, p. 91–109, doi: 10.1306/eg.07120606004.

Peters, C.A., 2009, Chemical Geology: Chemical Geology, v. 265, p. 198–208, doi: 10.1016/j.chemgeo.2008.11.014.

Pittman, E.D., Larese, R.E., and Heald, M.T., 1992, Clay Coats: Occurrence and Relevance to Preservation of Porosity in Sandstones: Society for Sedimentary Geology (SEPM),, p. 1–15.

Pollington, A., Kozdon, R., and Valley, J., 2011, Evolution of quartz cementation during burial of the Cambrian Mount Simon Sandstone, Illinois Basin: In situ microanalysis of: Geology, v. 39, p. 1–4, doi: 10.1130/G32195

Rosenbauer, R.J., Koksalan, T., and Palandri, J.L., 2005, Experimental investigation of CO2–brine–rock interactions at elevated temperature and pressure: Implications for CO2 sequestration in deep-saline aquifers: Fuel Processing Technology, v. 86, p. 1581–1597, doi: 10.1016/j.fuproc.2005.01.011.

Stoessel, R.K., and Pittman, E.D., 1990, Secondary Porosity Revisited: The Chemistry of Feldspar Dissolution by Carboxylic Acids and Anions: American Association of Petroleum Geologist Bulletin, v. 74, p. 1–23.

Surdam, R., Boese, S., and Crossey, L., 1984, The Chemistry of Secondary Porosity: Clastic Diagenesis. American Association of Petroleum Geologist, p. 127–149.

Swann, J., 1968, A Summary of Geologic History of the Illinois Basin: Geology and Petroleum Production of the Illinois Basin,, p. 3–21.

Templeton, J.S., 1951, The Mount Simon Sandstone in Northern Illinois: Illinois Geologic Survey,, p. 151–159.

Walderhaug, O., 1996, Kinetic Modeling of Quartz Cementation and Porosity Loss in Deeply Buried Sandstone Reservoirs: American Association of Petroleum Geologist, v. 80, p. 731–745.

Wigand, M., Carey, J.W., Schütt, H., Spangenberg, E., and Erzinger, J., 2008, Geochemical effects of CO2 sequestration in sandstones under simulated in situ conditions of deep saline aquifers: Applied Geochemistry, v. 23, p. 2735–2745, doi: 10.1016/j.apgeochem.2008.06.006.

Yu, Z., Liu, L., Yang, S., Li, S., and Yang, Y., 2012, An experimental study of CO2–brine–rock interaction at in situ pressure–temperature reservoir conditions: Chemical Geology, v. 326-327, p. 88–101, doi: 10.1016/j.chemgeo.2012.07.030.